CHEMICALLY GRAFTED ALUMINA SURFACE AND APPLICATIONS

LIU LINGYAN

A THESIS SUBMITTED

FOR THE DEGREE OF MASTER OF SCIENCE

DEPARTMENT OF CHEMISTRY

NATIONAL UNIVERISTY OF SINGAPORE

JULY 2006

ACKNOWLEDGEMENT

At first, I would like to express my greatest gratitude to my supervisors, Asst. Prof. Toh Chee Seng., for his invaluable guidance, suggestion and discussion throughout all my graduate study. It is him who inspired me in research, and introduced me into the fantastic nano-science world. His enthusiasm and preciseness in research inspirit me in this work. From him, I have learned not only invaluable knowledge, but also the attitude for research and scientific thinking.

I would like to thank Prof. Andrew Wee Thye Shen for introducing me to various facilities in NUSNNI and Prof. Goh Suat Hong for providing the usage of gonio-meter for contact angle measurement. I also would like to thank Dr. Yuan Ze Liang, Dr. Sindu Swaminathan, Mr. Subbiah Jagadesan, Mr. Chin Kok Chung, Ms Chong Ghee Lee, for their help in instrument operation training and sample analysis. I am also grateful to all my colleagues: Dr.Shuchi Agarwal, Ms. Deng Su-Zi, Ms. He Lin, Ms. Cheow Pui Sze, and Ms. Kok Guiwan for their kind help and support. In particular, thanks to Deng Su-Zi for her collaboration with QCM studies. In addition, thanks to all lab technologists of Department of Chemistry, National University of Singapore.

The financial support of this work is provided by the National University of Singapore in the form of a research scholarship, which is gratefully acknowledged here.

At the end, I would like to thank my fiance, Xu Wei, for his continuous love and support during my graduate study in Singapore.

TABLE OF CONTENTS

SUMMARY

Surface treatment with three fluorinated carboxylic acids was carried out on nano-porous commercial alumina surface and home-made glass supported alumina surface. The three fluorinated carboxylic acid were trifluoroacetic acid (CF_3COOH), perfluoropentanoic acid ($CF_3(CF_2)_3COOH$), and pentafluorobenzoic acid (C_6F_5COOH). X-ray Photoelectron Spectroscopy AXIS Instrument was used to characterize the surface modification. The result presented successful grafting on commercial alumina and etched glass-supported alumina surface. The variation of surface property after chemical treatment was studied by contact angle measurement and AFM Force- Distance plot, indicating more hydrophobic surface exhibited.

Adsorption of Immunoglobulin (IgG) on these nano-porous alumina surfaces were studied by Atomic Force Microscopy and Quartz Crystal Microbalance. Different performance of Immunoglobulin adsorption on un-grafted anodic alumina membrane and fluorinated group grafted alumina surface has been discovered under tapping mode AFM, which has also been used to study the adsorption of chemically grafted alumina surface in different concentrated IgG solution. Different concentration effects on IgG adsorption behavior have also been studied on thermal alumina under Quartz Crystal Microbalance. It can be concluded from both experiments that nucleation formed when adsorbent concentration beyond monolayer requirement. Prospective works are suggested including study on IgG time-frame adsorption using AFM and dual polarization interferometer (DPI).

NOMENCLATURE

AFM	atomic force microscopy
ESDA	Electron Spectroscopy for Chemical Analysis
IgG	Immunoglobulin
QCM	Quartz Crystal Microbalance
XPS	X-ray photoelectron spectroscopy

LIST OF FIGURES

A~D Ⅱ are cross section studies on any cross line of the corresponding surface.

Figure 4.3 Mass densities of IgG layers assembled on aluminium coated quartz crystals as a function of time in 0. 4 μg ml^{-1}, 0.8 μg ml^{-1}, 1.6 μg ml^{-1}, 2.4 μg ml^{-1}, and 3.2 μg ml^{-1}.

Figure 4.4 Replot of the data in Figure 3-1 in terms of rate of mass density change on aluminium oxide surface of aluminium-quartz as a function of surface coverage.

LIST OF TABLES

Chapter 1

Introduction

1. Introduction

Basic principles and instrumentations of the surface techniques mainly used in this project are introduced here, including X-Ray Photoelectron Spectroscopy, Atomic Force Microscopy, and Quartz Crystal Microbalance.

1.1 X-Ray Photoelectron Spectroscopy (XPS)

X-Ray Photoelectron Spectroscopy is also named as Electron Spectroscopy for Chemical Analysis (ESCA) by Swedish scientists Siegbahn and coworkers [1] when they firstly developed electron spectrometer for low energy electrons at high resolution by using X-ray as electron source in 1954[2]. Although the name of ESCA is less commonly used than XPS, it suggests the potential of the technique in chemical analysis area.

As the name shown, the technique is to obtain information of surface elemental compositions, as well as the chemical state of the elements. By analyzing the photoelectrons emitted from the solid material, and only the electrons from atoms near top 2-5nm surface are able to escape. Nordling et al. elaborated in their classic paper in 1958 that the XPS is able to detect the difference between copper and its oxide.[3] Siegbahn's group also described the chemical shift effect exists in many cases. The XPS/ESCA quickly has become one of the most popular surface analytical techniques since 1970s. During the measurements, a sample area of 1 cm^2 is commonly required. The detection limit of a sample monolayer varies according to elements weight ranging from 1% for light elements to 0.1% for heavy elements.

The following sections will make a discussion on the working principles of XPS/ESCA and its instrumentation.

1.1.1 Basic Principles for XPS / ESCA

The basic event for XPS/ ESCA measurement is photo-ionization, and the fundamental process is the adsorption of energy or photons *h*. These photoelectrons are produced by X-rays, thus gives the technique another name: X-Ray Photoelectron Spectroscopy. Here, we use Al Kα (1486.71 eV) x-ray. Usually, Mg Kα (1253.6 eV) is also used as X-ray source.

To be simplified, the incident X-ray can be considered as monochromatic, and emerging electrons can be treated as mono-energetic. When the scatter event takes place, the kinetic energy of an electron and the energy level of the electron source is the criteria to identify the atom. In vacuum chamber, the photon *hv* from X-ray irritates a free atom A from the sample surface, two possible cases are possible:

1> the photon energy *hv* is less than the binding energy E_b of atom A:

$$A + hv \rightarrow A^* \qquad \text{Eq. (1-1)}$$

The atom A is excited and ionized into A*. Later, A* can either emit fluorescence or produce an Auger electron, which is used in Auger Electron Spectroscopy (AES).

2> the photon energy *hv* is larger than E_b:

$$A + hv \rightarrow e^- + A^{+*} \qquad \text{Eq. (1-2)}$$

The photon *hv* interacts with atom A in the surface, causing atom A excited into A^{+*} and electrons to be emitted. Fig 1.1 illustrates this photo ionization process schematically. The electron escaping from the atom with a kinetic energy E_{KE} is given by:

$$E_{KE} = hv - E_b \qquad \text{Eq. (1-3)}$$

Where E_b is the binding energy of atom A in vacuum.

Other factors such as recoil, binding, relaxation effects, as well as the spectrometer potential differences have to be taken into consideration to modify the equation (Eq.1-3). For a free atom in XPS, it is necessary to take an additional recoil kinetic energy of the atom into account for a free atom, which in terms of E_{recoil}. However, according to the equation given by Siegbahn et al. on recoil energy value, E_{recoil} is negligible when using incident X-rays which is not too energetic.

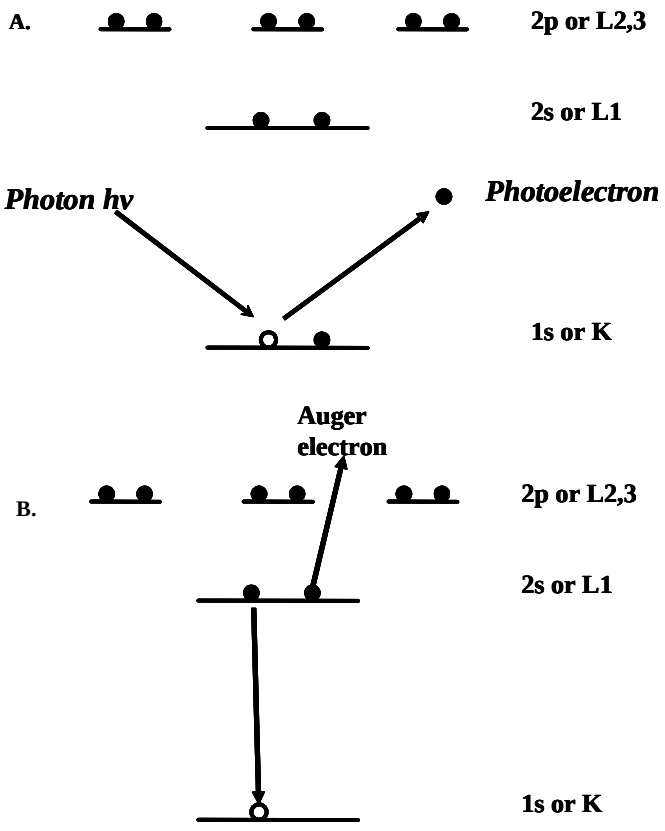

Figure1.1 Electron emission in XPS and Auger Electron Spectroscopy: A.X-ray photoelectron emission process; B. a KLL Auger process

The binding energy E_b for an atom in vacuum is defined as the electron orbital energy with regard to the Fermi level, or the energy change of the ion after removing an electron without changing wave functions of other electrons, which is also called Koopman's energy [4]. Therefore, the binding energy can be regarded as the energy change between initial and final state after the photoelectron has emitted from the atom. The kinetic energy of the emitted electrons varies corresponding to the final state of the ion from different atom type. Furthermore, the variety is also increased by cross-section of different final state. Figure 1.2 illustrates the ionization cross sections for an atom, from which the corresponding binding energies can be calculated out. As the Fermi level is defined as zero binding energy, the levels beneath it indicate different binding energy accordingly. From figure 1.2, it is observed that p, d and f levels splits when ionization, thus giving the vacancies in sub-levels such as $p_{1/2}$, $p_{3/2}$, $d_{3/2}$, $d_{5/2}$, $f_{5/2}$, and $f_{7/2}$. The spin-orbit splitting ratio for p, d, and f level is 1:2, 2:3, and 3:4 respectively.

Typically, the kinetic energy of photoelectrons E_{KE} is not more than 1200eV, so with elastically scattering off other atoms or electrons, they can only get rid of a

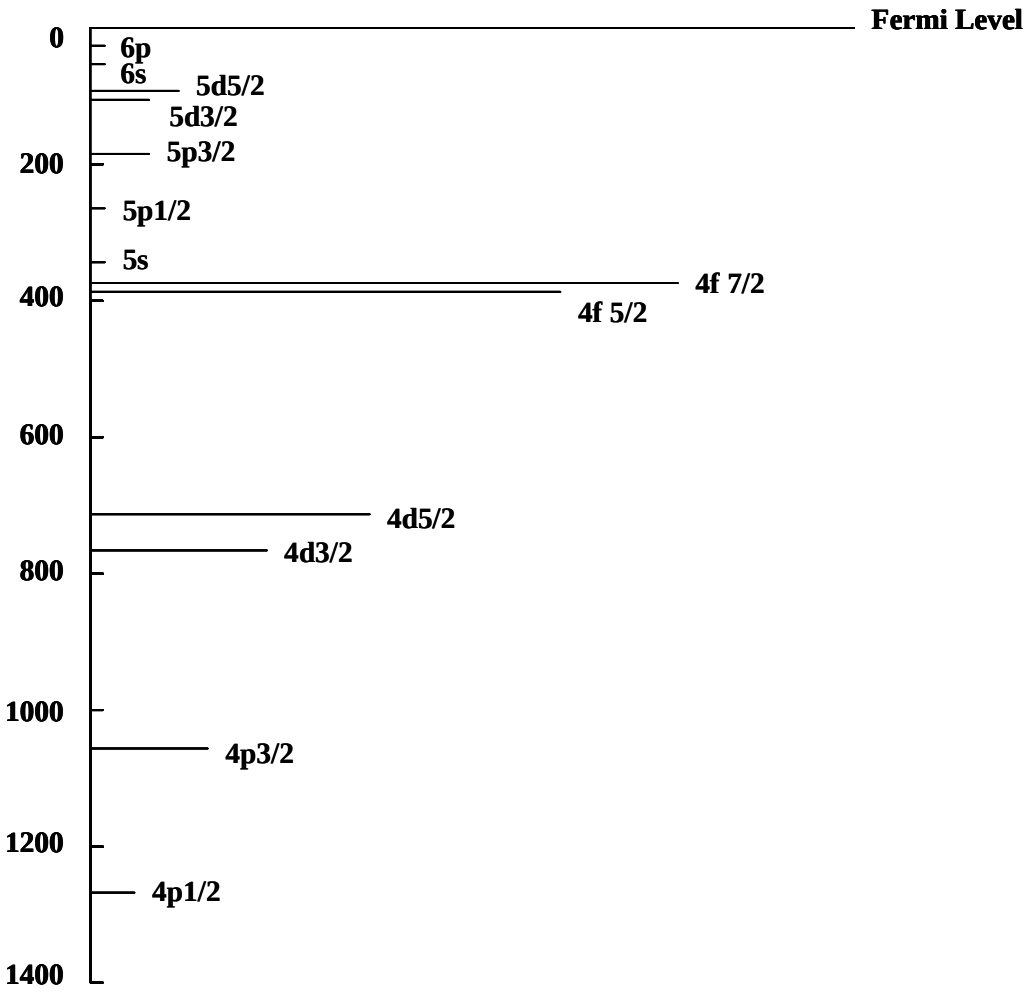

Figure 1.2 The relative binding energies and ionization cross-sections for an atom

shallow surface with depth ≤ 30 A. If the remaining electrons exist and relax in the free atom, E_a is described as the additional energy for the emerging electron, thus giving the equation:

$$E_{KE} = \quad h\nu - E_b + E_a \qquad \text{Eq. (1-4)}$$

If the atom is on/in a solid surface, because of the interaction between the atom and other electrons/atoms, an additional relaxation energy E_r is introduced, so that,

$$E_{KE} = \quad h\nu - E_b + E_a + E_r \qquad \text{Eq. (1-5)}$$

Since the shift E_a+E_r is as small as 1% of E_b, the atom can be identified with the knowledge of its electronic energy level. When an electron comes from an atom in solid surface, the environment will cause a small shift of the electron energy, which is called "chemical shift". Normally, the difference in chemical potential and polarize-ability raises the chemical environment variety. Therefore, this "chemical shift" can be used to study the chemical environment/state of the atom from which the electron emitted. The "chemical shift" can also be affected by the final relaxing energy condition of the electron in addition to its initial energy state. So far, the chemical shifts of atoms with different chemical bonding have been systematically studied by scientists [5], thus the unknown chemical environment can be inferred by comparing the investigated shift with the standard list.

Because of the different spectrometer effects, instead of compare with absolute binding energies, a spectrometer work function Φ_s has been introduced into the equation:

$$E_{KE} = h\nu - E_b + E_a + E_r + \Phi_s \qquad \text{Eq. (1-6)}$$

1.1.2 Quantitative measurements by XPS/ESCA

Since every element has its unique set of binding energies, the XPS/ESCA can be used for quantitative analysis based on peak intensity. Excluding the matrix effects, the relation between atom number in the testing volume sample and the corresponding peak intensity is:

$$\text{Peak intensity} = I n_i P \varepsilon \left(d\sigma/d\Omega\right) d\Omega \qquad \text{Eq.(1-7)}$$

I is the X-ray flux; n_i is the atom number of a certain type i in the volume sample; P is the probability of atom escape from the surface without loss; ε is the detector efficiency; $d\sigma/d\Omega$ is the differential cross section of electron of atom i; and $d\Omega$ is the acceptance solid angle of the electron analyzer. [6-7]

As the Equation 1-7 shows, when comparing the concentrations of two atoms in a certain sample, the differential cross sections ($d\sigma/d\Omega$) of both atoms are required, or at least the with knowledge of the ratio. These cross sections are decided by two factors: one is the atomic number in measurement; the other is the electronic level for electron ejection. The commonly used X-ray sources, Al Kα (1486.71 eV) and Mg Kα (1253.6 eV), limit the available electronic level within the provided energy. The X-rays provide enough energy for atomic number up to 20 to allow electrons being ejected from 1s level. Higher electronic levels are required for higher atomic numbers. Within the available energy range, the cross section for a given section varies by the magnitude orders according to different atomic number. To be within a single magnitude order, this cross section variation can be reduced if different energy levels are chose for different atoms. Normally, for a sample with knowledge of compositions, calibration of peak heights is used to estimate relative concentration with the accuracy of 10~50%.

As review by Seah [8], and Powell and Seah [9], the peak intensity I for an element from a solid surface can be taken as the peak height or peak-to-peak height in energy spectrum or derivative energy spectrum respectively. If the intensity of the element A is given as I_A;

the provided elemental sensitivity factor is given as I_A^{∞}. The molar fraction X_A of element A is:

$$X_A = I_A / I_A^{\infty} \qquad \text{Eq.(1-8)}$$

If only the peak intensity ratios are accessible, the equation is derivate into:

$$X_A = I_A / I_A^{\infty} \Sigma (I_i / I_i^{\infty}) \qquad \text{Eq. (1-9)}$$

If element A forms a monolayer φ_A on the substrate B, Powell and Seah [9] give out:

$$\varphi_A = Q_{AB}^{X} (I_A / I_A^{\infty}) / (I_B / IB^{\infty}) \qquad \text{Eq.(1-10)}$$

Whereas Q_{AB} is a monolayer matrix factor for monolayer coverage of less than 0.2 atomic fractions.

1.1.3 Instrumentation of XPS/ESCA

XPS/ESCA instrument consists of three basic components: an X-ray source, a sample holder, and an electron energy analyzer.

In XPS, x-rays are created by electron bombardment of Al or Mg targets. A simple X-ray tube can be used as the X-ray source in relatively low resolution measurement. Normally for a high resolution XPS, both of the two sources are used for switching between each other thus permit two distinguished spectra: shifted XPS peaks, and fixed Auger peaks. In a higher resolution XPS instrument, the X-ray beam is focused to providing a narrow line (not more than 1mm) by mounting the X-ray source onto a Rowland circle.

Both sample holder and the electron energy analyzer are placed in high-vacuum chamber. The sample holder can rotate in three dimensions. Several samples can be mounted on the holder and switched from one to others. The sample insertion system help the sample holder retracted and isolated from vacuum chamber when samples being mounted. Then the samples are inserted through the insertion chamber followed by rapidly pumping down. The procedure can help maintain the primary ultra-vacuum system by excusing venting the main vacuum chamber. The temperature can also be controlled with the range of -50 to 600 degree C for commercial instruments.

Typically, one of the three types of electron energy analyzers is used: the hemispherical sector analyzer (HSA), the cylindrical mirror analyzer (CMA), or the 127^{o} sectors. As compared and suggested by Woodruff and Delcharearly in 1986[10], nowadays HSA is widely used in XPS as it can provide high resolution spectra for long working distance; as CMA is normally used for Auger spectra for its relatively low resolving power but high collection efficiency; whereas 127^{o} sector analyzers are used in High Resolution Electron Energy Loss Spectroscopy (HREELS).

1.2 Atomic Force Microscopy (AFM)

During the last two decades, the scanning probe techniques in deputation of Atomic Force Microscopy (AFM) and Scanning Tunneling Microscopy (STM) have undergone an extensive development as promising techniques for surface imaging and visualization. The most attractive advantage for these imaging techniques is their capability for real-

place measurement at the atomic level. This atomic resolution of AFM and STM provides the visualization of the finest surface details, satisfying the increasing need of miniaturization to nano-scale in current world. Another obvious advantage which makes AFM and STM outstanding is their compatibility for use in various operation environments. In comparison, ultra high vacuum or other constraining condition is a pre-requirement which limits most other surface techniques. Especially, when a solid-liquid interface or a biological surface is under measurement, certain modification is necessary for strict operation environments required in these other surface techniques. Whereas, in AFM and STM, the surface can be measured under ambient conditions and other environments including water or other types of fluid without sophisticated modification.

In addition, another feature which distinguishes AFM from STM is the technique does not depend on sample conductivity when generating images. It works well on both conductive and non-conductive surfaces. STM and SEM techniques, which rely on electron movements on sample surface, require conductive surfaces. Furthermore, AFM is also applicable for electrochemical environment because of its inert tip. Not only surface with atomic resolution can be investigated by AFM, but also the force between tip and a defined place on the surface can be measured at nano-Newton scale. Other derivative techniques such as magnetic force microscopy expand AFM capabilities among surface characterization techniques.

As all the advantages listed above, nowadays AFM is being widely used not only for researches of different fields including materials, biology, chemistry, and physics, but

also for various industries in electronics, biological, chemical, aerospace and so on. The surfaces being measured include film coatings, glasses, ceramics, metals, polymers, membranes, and semiconductors. A broad range of phenomena are studied by AFM such as adsorption, adhesion, etching, corrosion, plating, crystal growth, and so on.

1.2.1 Basic Principles and instrumentation for AFM

The AFM operates by sensing the force between a tip which is mounted at the end of cantilever spring, and a sample surface held by a piezo-electric scanner. The changes of cantilever or spring deflection are related to the tip-sample force changes. During the measurement, the sharp probe moves over the sample surface. The tip movement is controlled by piezo scanner which is made from piezo-electric ceramics and with a high resolution of sub-angstrom in x, y, and z direction, where z-axis is perpendicular to the measuring surface.

Different methods are applied to detect this cantilever or spring deflection. The first AFM invented in 1986 by Binnig, Quate and Gerber [11] used a scanning tunneling microscope at the end of the AFM cantilever to detect its movement. However, it was found that the force brought by STM is larger than being investigated under AFM. Later, the optical lever technique has been developed by Meyer and Amer [12], which is being commonly utilized by most of commercial AFM currently. Figure 1.3 illustrates how this optical lever detection works. The light from the laser is focused on the end of the cantilever, and reflected onto the split photo-diode. When the cantilever flexes, light reflects toward the

top or bottom photodiode sector based on deflect direction. The photocurrent imbalance thus induces a signal proportional to the bending of the cantilever.

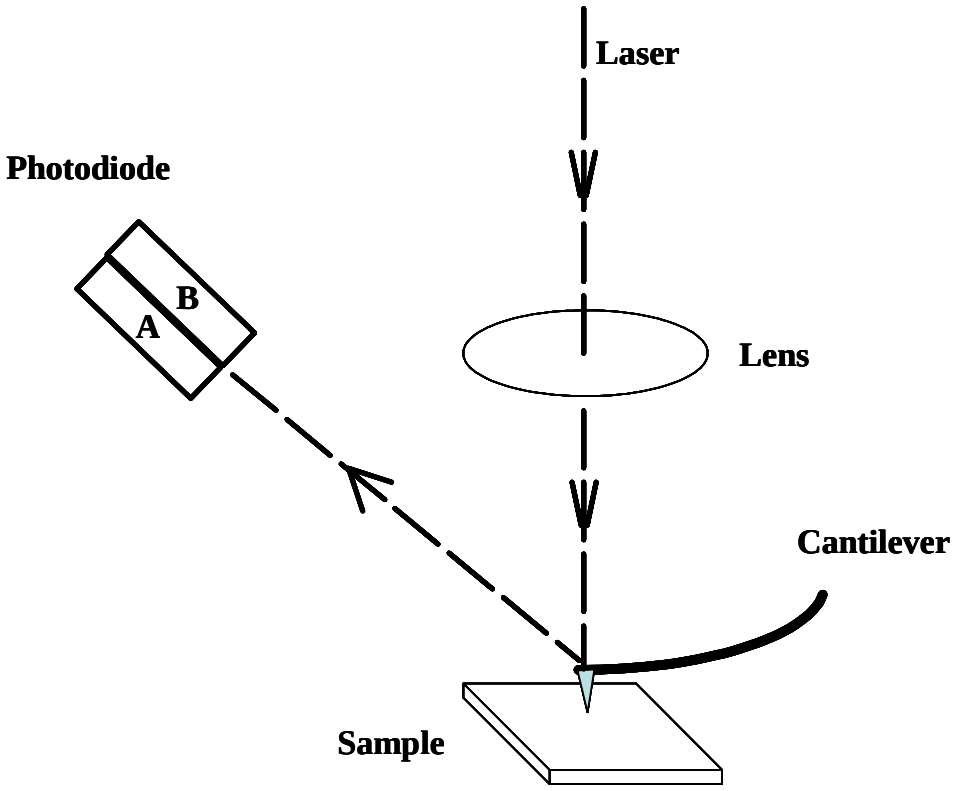

Figure 1.3 An AFM schematic. The sample moves under the sharp tip held by the cantilever. Focused by the lens, the laser arrives at the end of cantilever and reflects onto the split photo-diode. The detection of the light in different direction from the cantilever caused by tip deflection thus gives the topology of sample surface.

The cantilever obeys Hooke's Law for fine displacement:

$$F = -kx \qquad \text{Eq. (1-11)}$$

Where F is the force between the tip and surface, k is the spring constant, and x is the displacement. The interaction force between the tip and sample surface can be calculated out with the knowledge of displacement x.

Therefore, three essential elements comprising of a typical AFM are:

1) Piezo-electric scanner.

The scanner is normally in form of a tube, with the main device made from a soft piezo-electric ceramics. Piezoelectricity is a kind of electromechanical transducer which creates a mechanical motion from electrical energy. When the material is placed in an electric field, it undergoes a change in geometry. This mechanical motion takes place because of the property of non-centrosymmetricity. When exposed to an electrical potential, the crystalline structure of material changes giving a dimensional change. Thus the direction and amount of motion changes are decided by the type of piezoelectric material, as well as its shape and field strength. Figure 1.4 shows an example of the motion change when a piezoelectric material is placed in an electrical field.

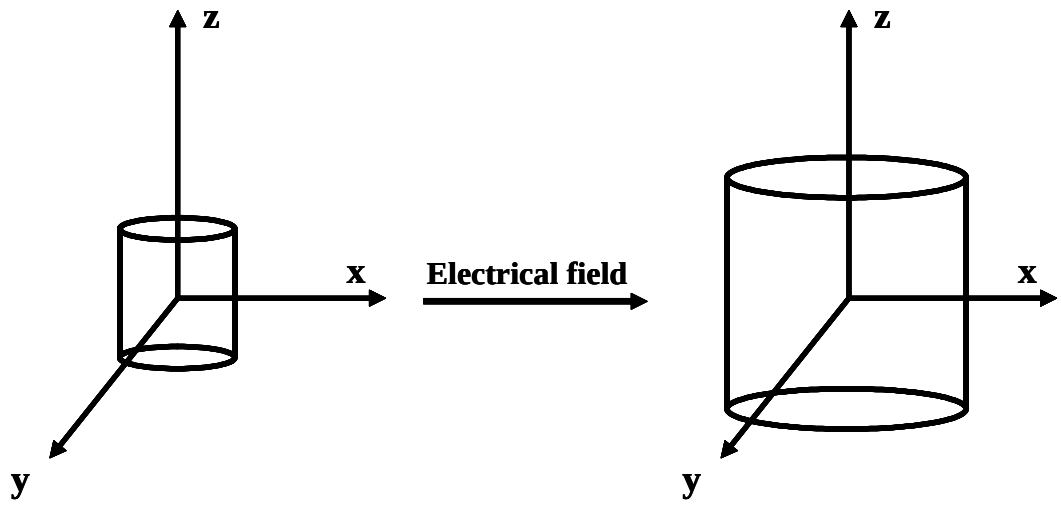

Figure 1.4 a piezoelectric material changes the motion in x,y,z direction when an electrical field applied on it.

A typical piezoelectric material will expand or contracted by about 1 nm per volt, with a range of DC voltage from -500 to +500 volts. To get a larger motion change in practice, hundreds of piezoelectric material layers are made into a

piezoelectric transducer. Taking a transducer consisting of one thousand layers of piezoelectricity for example, a motion of 1000 nm can be readily obtained per volt. Thus 0.1 mm of motion is possible with 100 volts for this transducer. However, less layers of piezoelectric material can be used to produce a high resolution, say, 10 layers are used from the above kind of material, which means every volt induces 10nm motion change. This is equal to a displacement resolution of 0.01 nm per mV, and for a computer controlled system, the resolution is 0.04 nm for this transducer.

Therefore, the piezoelectric scanner provides an extremely precise positioning with a high resolution of sub-angstrom in x, y, and z direction for AFM system.

2) Micro-fabricated cantilever

In AFM system, the probe is given by a tip mounted on cantilever. The cantilever will bend in response to the force between the tip and the measuring surface. The even and sensitive response is required which is provided by excellent uniform material. Generally, AFM tip and cantilever is are micro-fabricated from Si and Si_3N_4.

3) Diode laser and its optical path

The AFM detection system comprises of a prism, lens, mirror, cantilever and a photodiode detector. The laser is focused onto the backside of the tip of the cantilever by the lens. The mirror helps to locate the light reflected from the

cantilever to the position-sensitive photodiode detector. The cantilever angular deflection causing doubled laser beam thus been detected by giving the different position of the laser spot on the detector. As a result, the angular deflection of the cantilever can be distinguished. It can be seen that, the pre-experiment adjusting on laser focusing, light positioning on cantilever as well as on detector is crucial to the final reliability of the image. Since the distance from cantilever to the detector is as thousands of times long as the length of the cantilever, the motion of the tip is greatly magnified by this optical path. Some advanced commercial system use four detector areas for the centre point to monitor the cantilever with both torsion and vertical movements, thus obtain a number of imaging modes after deconvolving the data.

1.2.2 Feedback operation

In the view of Feedback Operation, AFM can be divided into two principal modes:
One is with feedback control; the other is without feedback control.

When the feedback control is turned on, the electronic feedback loop will respond to cantilever deflection changes which are detected by the position-sensitive photodiode detector. Upon the deflection being sensed, it will be compared in a DC amplifier of feedback loop with the desired value. If the difference is found from the desired value, a voltage will be applied to the piezoelectric positioning system, alter the tip-sample distance by moving the sample (or the tip) down or up to compensate the deflection change. In this way, the force between sample and tip will be restored to a pre-

determined value. This feedback mode of operation is also known as constant force imaging since the force of interaction between tip and sample is maintained constantly. The feedback mode is most commonly used as it provides a fairly faithful topography of the substrate surface.

When the feedback control is switched off, the AFM is then operated in a so-called error signal mode. It is especially used when investigating very flat samples by providing a high resolution. Normally, a small proportion of feedback loop control is used simultaneously to protect tip from being damaged by rough surface in accident, or avoid other problems like thermal drift. This kind of error signal mode can also be displayed when feedback mode is being used to remove variation in topography.

1.2.3 Tip- sample interaction

AFM, as the name shows, Atomic Force Microscopy, affords the resolution in order of atomic level on many surfaces. This high resolution is given out by the magical AFM imaging mechanism.

The ultimate high resolution of AFM imaging is defined by the magnitude and nature of interaction force between tip and investigated surface when the size of probing tip has been given by microscopy. Therefore, imaging modes of AFM are sorted by this tip-sample interaction.

Contact mode is the most common imaging method for AFM. During the operation, the tip and sample remains close contact with each other. The force pushes the cantilever against the surface which is set by piezoelectric positioning system with a range from nanos to micros Newton. The essential feature of operation of this contact mode has been detailed discussed in Feedback mode on above. The hard surfaces are quite suitable for this contact mode. And the majority of contact mode operates in ambient or liquids environment, while some cases operate in ultra-high vacuum.

Some problems exist in contact mode operation caused by the tracking force of the tip applied on sample surface. Although the problem can be improved by reducing the tracking force of the tip, some practical control limits on magnitude of the minimized forces can not be avoid by users when operation carried out in ambient condition. In ambient environment, the investigated surfaces are covered by a layer of 10 to 30 nm thick as a result of adsorbed gas and water vapor. When the tip gets in contact with this layer, a meniscus will form between tip and surface resulting in the cantilever being pulled towards the surface by surface tension. Typically, this meniscus is about 100 nN force based on the tip geometry. But if in liquid media, this kind of attracting force can be neutralized. Other factors affecting the resolution such as capillary forces and Van der Waals' forces can be reduced by operating in liquid system. In addition, some studies involving process like biological ones requiring solid-liquid interface can be achieved in liquid operation system. However, the liquid measurement also brings some artifacts in images caused by sample hydration and sensitive biological samples.

On the other side, when contact mode is applied on charged surface like semiconductors, a electrostatic charge is easily to be trapped between the tip and surface. Although this electrostatic charge contributes a little amount of attractive force, it induces a substantial frictional force when the tip scanning along. This frictional force dragging over the surface results in a more serious surface damage than a normal one. This destructive force also causes dulling the tip and distorting the investigating image.

Other surfaces like ones with adsorbed layers, biomaterials, even sometimes are placed in aqueous solutions, are not suitable for contact mode. Because when the tip scans over the surface, it creates damages or displaces the adsorbed molecules. In these cases, rather than contact mode imaging, imaging with non-contact mode and tapping mode are introduced.

Non-contact mode is introduced a new imaging way for sensitive samples which are easily been altered by tip contact. During the scanning, the tip suspends 50 – 150 Angstrom above the sample surface. The detective force attributes the tip to provide surface topographic image is the Van der Waals forces between the tip and sample surface. These Van der Waals forces are much weaker than those used in contact mode AFM. Thus, in order to detect such small forces, AC detection method has been used. In this way, the tip is required to be oscillating during the scanning and AC detector measures the change in amplitude, phase or frequency of the oscillating cantilever according to the force gradients between the tip and surface. In those high resolution

equipments, it is able to measure the force gradients only a nanometer from the investigating surface.

However, since the thin layer of fluid contaminant exists on the surface in ambient conditions, a capillary bridge is easily formed between the tip and the surface resulting in the non-contact mode failed into contact mode. Even in vacuum and liquid system, this capillary effect is extremely worse. As a result, a request of tapping mode is brought forward.

Tapping mode is another most common mode in AFM. It acts as one of the most potential techniques offering high resolution images for the surfaces which are easily deformed or easily removed from the substrates and difficult for imaging by other techniques. The rule for tapping mode is to integrate the advantages of both contact mode and non-contact mode. The tip performs alternately contact and lift away from the sample surface. The high resolution images are given out when the tip touch the surface, and then move away from it in order to avoid the tip dragging over the surface. In this way, tapping mode also overcomes a series of problems of both contact mode and non-contact mode such as electrostatic force, friction, adhesion, and so on.

The tapping mode scanning operation is performed in ambient condition by oscillating the cantilever with the frequency at or near its resonant frequency. During the scanning process, the cantilever oscillates at high amplitude of at least 20nm when the tip is drawn away from the surface. After that, the tip is moved down to the surface until lightly

touches it. This frequency of the tip alternatively lifting up and down ranges from 50,000 to 500,000 cycles per second. When oscillating cantilever touch the surface, the oscillating frequency decreases due to the energy lose as the contacting happens. And this oscillating frequency reduction can be used to identify surface characteristics.

NanoScope software is used to provide a digital feedback loop for maintaining the cantilever oscillation amplitude during the operation. Before the scanning, the software assists operators to select the optimal oscillation frequency and lowest operation level of scanning force. During the scanning, the tip scans over a protruding place resulting in the less oscillating space for cantilever, as well as a decrease of oscillation amplitude. In reverse, if the tip comes across a concavity, the space for cantilever oscillation increases giving the same trend for the amplitude. These changes of oscillation amplitude are measured by the detector followed by the digital feedback loop adjusting the tip-sample distance to maintain the amplitude and scanning force.

The advantage of tapping mode becomes outstanding when the tip contacts the surface with high frequency of 50~500 kHz greatly reduce the tip-sample adhesion force thus help prevent tip being trapped by surface which will result surface damage. Furthermore, as the force is applied at lowest level and of vertical direction, the surface will not be pulled away by any transverse force.

When operating in fluid system, the tapping mode operates with the same advantages as in ambient system. However, as the tip placing in fluid, the fluid is likely to affect cantilever oscillating frequency. To solve the problem, the entire fluid cell is oscillated thus make the cantilever oscillate together. The same working principle applies as the amplitude changes when the tip scanning over the surface with different feature. However, the appropriate frequency for this fluid cell driving oscillation falls in the range of 5,000 to 40,000 cycles per second. As the frequency is lower compared to the operation in the air (50,000 to 500,000 cycles per second), softer cantilevers with lower spring constant of 0.1 N/m are used compared to the one for air condition ranging from 1-100 N/m.

1.3 Quartz Crystal Microbalance

Quartz Crystal Microbalance (QCM) has become an attractive analytical technique because of its simple design and wide applications. [13] As an extremely sensible technique which can detect nano-gram level of mass change on the quartz surface, QCM has been used in observing many important physical and chemical processes by measuring these associated mass changes. [14]

1.3.1 Basics of QCM

It has been acknowledged that in mechanical oscillating system, the resonant frequency is correlated with the mass of oscillating body. In the other word, with all of other characteristics keeping constant, the change of the oscillating frequency can be used to

calculate mass change of the oscillating body. Since the other parts of the oscillating system always keep stable along the measurement, the QCM become a sensitive tool to quantitatively monitor interface-process.

The oscillating body used in QCM is comprised of a thin piece of pieozoelectric material. Usually quartz is particularly used here not only because it is economical, stable and chemically inert (the most stable form of SiO_2), also it can provide various types of resonators. As a resonant material widely used in electronic devices, the properties of quartz such as oscillation mode, resonant frequency of different mode, as well as the temperature impact have been well defined. In QCM, quartz crystals of alpha type are used, since it has most excellent mechanical and pieozoelectric properties of the all. The oscillation mode depends on the crystal cutting angles with respect to the crystal optical axis. The most common used quartz is of AT-cut crystal produced by slicing across a quartz body with an angle of $35^o10'$ shown in Fig.1.5 to the optical axis. This angle gives the cutting vertical to the resonator surface. The AT cut method gives a crystal with frequency drift nearly zero when temperature ranges from 0 to 50 °C. Other precise cutting ways produce special use quartz for QCM including BT-cut crystals, SC-cut crystals, IT-cut crystals, and FC-cut crystals.

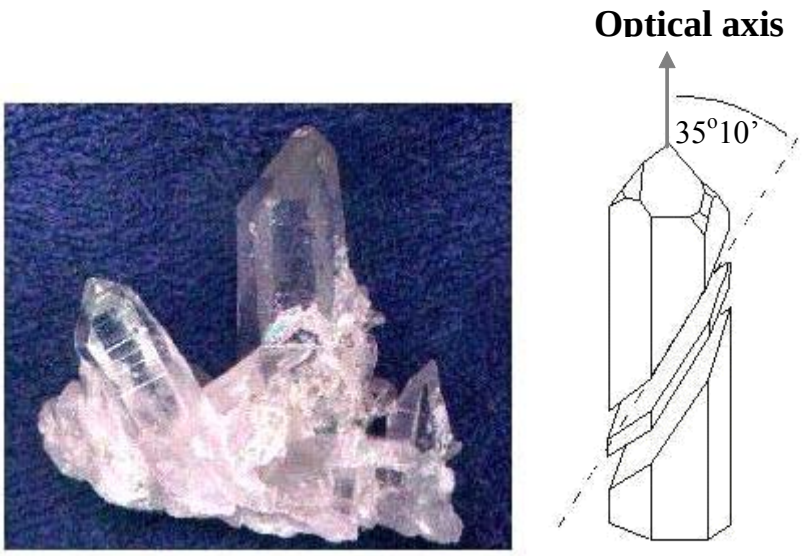

Figure 1.5 The quartz crystal and AT cut

A thin disk of quartz is positioned between a pair of electrodes, and the whole system appears as a sandwich structure. The positioned electrode is made of a thin plate of metal. Gold is used in majority since it is chemically inert, easy to be deposited and can be easily connected with "thio-" group for many self-assembly system, though a very thin layer of about 0.1 to 0.2 μm of gold surface is suspected oxidized in environment.[15] Generally, a layer with thickness of 1000 Angstroms Gold is evaporated on a support of 100 Angstroms Cr or Ti over the quartz. Other electrode materials have been employed include silver and aluminum which easily become oxidized in liquid [16], as well as Cu, Ni, Pt. Before operation or sampling, the gold surface is treated with Piranha solution for removing organic contaminations.

During the operation, the crystal in placed into an oscillating circuit, and by applying an alternating voltage over the electrodes on the two sides of the quartz, the quartz crystal begins to oscillate at its resonance frequency. This oscillation results in a transverse

acoustic wave spreading over the crystal and reflecting back to the crystal surface again. Properties of oscillating body including the mass, thickness, density, shearing method of the quartz, as well as the oscillating media – in the air or liquid, the viscosity of the liquid, decide the resonance frequency. Typically, QCM operates with frequency range of 5 to 10 MHZ.

1.3.2 Mass-Frequency relationship

By analyzing the measured frequency change Δf resulting from the adsorbed or deposited mass change Δm on quartz, Sauerbrey[17] firstly suggested the equation for mass calculation based on the oscillating frequency:

$$\Delta f = -[2 \times f_0^2 \times \Delta m]/[A \times (\rho_q \ \mu_q)^{1/2}] \qquad \text{(Eq.1-12)}$$

Where f_0 is the resonant frequency of the fundamental mode of the crystal; A is the piezo-electrically active area; ρ_q is the density of the quartz, with the value of 2.649g/cm^3 for typical quartz crystal; μ_q is the shearing mode of the crystal, with the value of 2.947×10^{11} g/cm$\times$s^2 for AT-cut quartz.

However, Sauerbrey's equation only holds with the assumption 1) the deposition is rigid; 2) the deposited or adsorb layer is uniform and stable. These assumptions limit the QCM advisable in gas phase or vacuum system. Later, at the beginning of 1980's, liquid phase QCM has been studied by scientists with the pioneers of Kanazawa and his co-workers, showing that the oscillation also can stably operate when immerging in liquid. Therefore, Kanazawa et al[18] give out the modified equation taking consideration of liquid's density and viscosity as shown in equation

$$\Delta f = - f_u \, 3/2[(\rho_L \, \eta_L)/(\Pi \times (\rho_q \quad \mu_q)]^{1/2} \qquad \text{(Eq.1-13)}$$

Where f_u is the resonant frequency of the quartz before loading; ρ_L is the liquid density, and η_L is the liquid viscosity. Their research has found that even with the viscosity property changes in liquid media, the QCM can still operate sensitively for mass changes probing. And this is especially suitable for those condensed substance such as polymer and bio-molecules.

Chapter 2

Experimental

2.1 Materials

Whatman Anodisc 25 alumina membranes of 60 μm thickness with 0.1 μm nominal pore size were purchased from Fisher Scientific. 1,2-dichloroethane(99+%), and Trifluoroacetic acid (98%) were purchased from Sigma-Aldrich; 2,3,4,5,6-pentafluorobenzoic acid (>97%) was purchased from Fluka, and perfluoropentanoic acid (98%) was obtained from Lancaster. And all of above chemicals were used as received.

Mouse monoclonal antibody (IgG2b-kappa, clone GST 3-4C) rose against the 26 kDa GST proteins from S. japonica, supplied by ZYMED laboratories Inc. as a 200 ml aliquot at a concentration of 0.5 mg ml^{-1} in PBS, pH 7.4, containing 0.1% sodium azide (NaN3), and was used as received. Monoclonal anti-glucose oxidase (anti-GOX) in forms of ascites fluid was purchased from Sigma Aldrich and supplied with the concentration of 8.2 mg ml^{-1}.

2.2 Chemically grafted nano-porous alumina surface

2.2.1 Sputtering of Al films

Aluminum films were produced on microscopy glass slides by RF sputtering (Discovery®-18 Sputtering System) using a 99.999% Al target in an argon atmosphere. The deposition conditions for Al films using RF-sputtering are as indicated below:

RF Gun Supply was under 200W;

- Argon (Ar) flow rate used in the chamber was 60 sccm (standard cubic centimeter);
- Chamber pressure was 10^{-7} Torr during sputtering process;

- The pre-sputtering time was kept the same for every deposition: 180 seconds to remove the impurity on target surface;
- Sputtering time of 5400sec was applied on the substrates during all the experiments;

Here, microscopy glass was used as substrate to support sputtered aluminum film. Before loading into the sputtering chamber, the microscopy glass was washed in dichloroethane, followed by acetone, ethanol, and nanopure water, and dried in oven at 120 ^{o}C.

The parameters of sputtering affect sputtered surface in grain size, uniformity, sputtering speed, and thickness. These affecting parameters mainly include power of RF gun, flow-rate of activation gas, spin speed of the holder, and sputtering time.

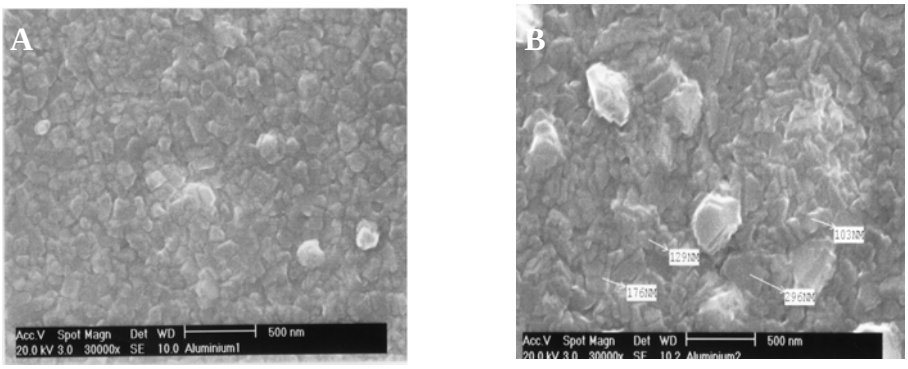

Figure 2.1. SEM results of sputtered Al on glass under sputtering conditions: A) 200W RF Gun Supply; B) 300W RF Gun Supply; with all of other parameters remain the same.

The SEM pictures shown in Fig. 2.1 give the example that, both the sizes and uniformity of aluminum grains can be affected by the RF Gun Supply. With all other parameters remain the same as given in 2.2.1, Fig. 2.1A used 200W RF Gun Supply and Fig.2.1B used 300W. The aluminum grain sizes of sputtered Al under 200W RF Gun Supply range

from 70 nm to 150 nm, while under 300W RF Gun Supply, most of the grain sizes are more than 120 nm, even some of them extend 300nm. Furthermore, aluminum grains in Fig. 2.1A are more uniform than those in Fig. 2.1B. Therefore, the parameters of Fig 2.1A are used in following sputtering conditions.

The thickness of sputtered aluminum was measured under profile meter. After 5400 sec sputtering, a layer of 436.1$\pm$ 7.4 nm aluminum was deposited on microscopy glass.

2.2.2 Electrochemical anodization and surface etching of glass-supported alumina

The electrochemical anodization of these aluminum films were prepared according to procedure described in reference [27]. The sputtered aluminum film was anodized at a voltage of 40 V, in 0.10 M oxalic acid for 3 min. The anodized film was then rinsed with de-ionized water thoroughly and immersed in a solution containing 0.20 M chromic acid and 0.30 M phosphoric acid for 5 min. The film was rinsed with de-ionized water again, and anodized in 0.10 M oxalic acid for another 3min. Finally, the sample was rinsed with de-ionized water thoroughly.

To obtain different sizes of pores on alumina surface, the etching process of glass-supported alumina was carried out in 3 % phosphoric acid for different time periods ranging from 10 to 60 min. Finally, the samples were dried in oven at 120 oC for 2 h.

Morphology and microstructure of alumina-coated surfaces were observed using field emission scanning electron microscopy (FEI, XL30-FEG SEM) with an energy dispersive X-ray analyzer (EDX).

Scanning Electron Microscopy pictures in Fig 2.3 clearly show the different pore sizes achieved by different etching time in 3wt% phosphoric acid. The pore sizes range from 10 nm to 100 nm and give very regular pore structures (Fig 2.3 C, D, E). These pores are formed on the aluminum particles during the electrochemical anodization. At the beginning of anodization, the alumina comes out as nonporous (shown in Fig 2.2 step1,2), further Al_2O_3 forms through Al cations moving outward from the bottom and the anion and water molecules coming inward (shown in Fig 2.2 step3). With these continuous Al cations, anions and water molecules coming from bulk to the substrate interface, the successive Al_2O_3 grows from the underline aluminum substrate which acts as Al source to provide this oxide growth. In the other way, because of nonconductive Al_2O_3 formed, following anodization rate decreases, which is given by anodization current dropping from more than 150 mA to about 10s mA in the first ten seconds, and later the current stays at 2 mA.

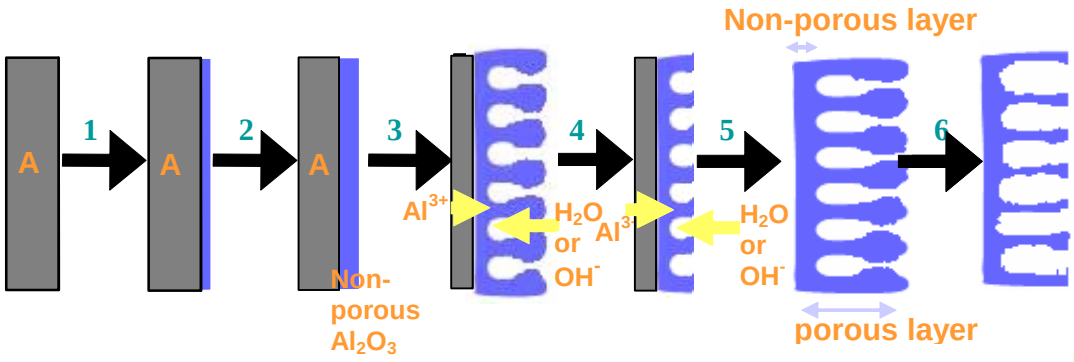

Figure 2.2. **Electrochemical Anodization process**

The actual mechanism of forming the highly regular structure of the alumina is stilled uncertain, but is believed that fluxion of the anions and water molecule towards the alumina/liquid interface helps shape the pores within the porous layer as illustrated in Fig 2.2 above. After the first step of anodization, the samples are immerged in the solution containing both chromic and phosphoric acid. The solution thins down alumina walls formed in the first step of anodization by etching (Fig 2.2 step 4). Hence the following pores structures are shaped to form in the second anodization step (Fig 2.2 step5). After second anodization accomplished, these porous alumina are further etched in 3% phosphoric acid.

An increased pore sizes are observed with extension of the surface etching time in 3% phosphoric acid, given by a series of SEM pictures in Figure 2.3. In Fig 2.3A, on the glass-supported alumina surface without etching in phosphoric acid, about 10 ~ 20nm pores can be investigated. Between the pores there are 100 ~ 200nm wide “alumina wall”. On the surface, pores do not appeared on some particles as large as 500nm. It is because of that the alumina growing from aluminum cover the channels between alumina walls,

thus the pores can not be observed from the surface planar. When etching process takes place, a layer of alumina surface in all dimensions exposed to the etching solution is shaved off. The longer the etching time, the more of the alumina layer are removed. As a result, the alumina wall become thinner, and the pores become larger (from Fig 2.3 B to Fig 2.3 D). In addition, a decrease of the surface roughness has been found due to the larger possibility of the outlet surface exposed to bulk etching solution. However, when the etching time extends to 60 mins (Fig 2.3 E), even some of the alumina walls begin to be totally removed away, which result in the combination of the pores.

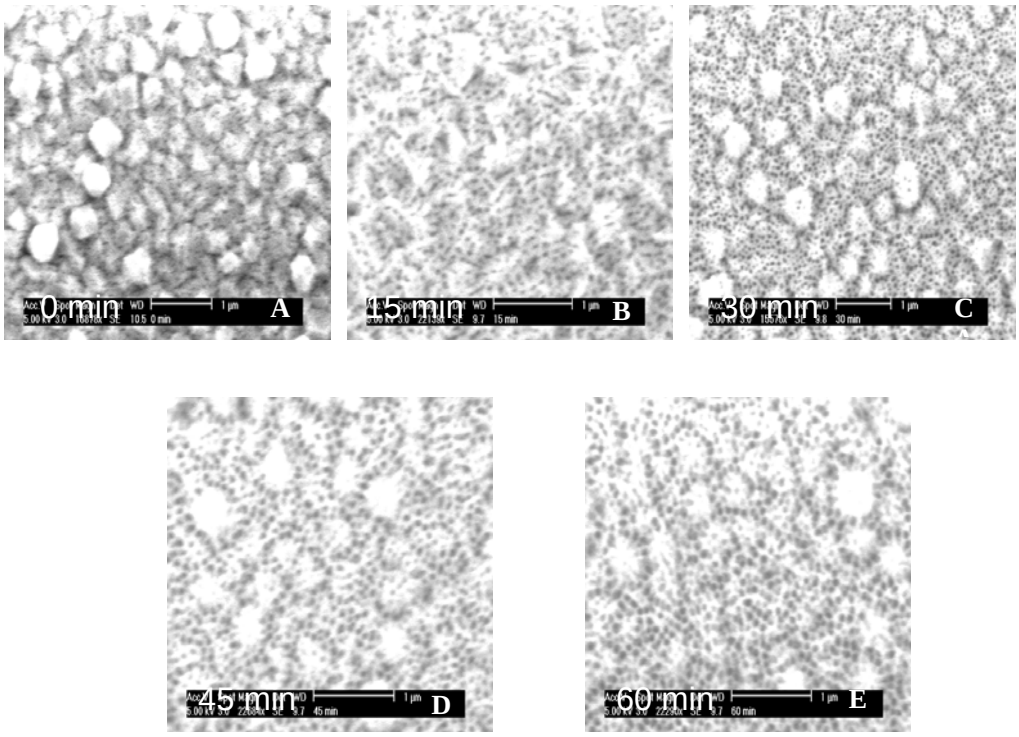

Figure 2.3 SEM pictures of glass-supported alumina film with different pore sizes

In addition, the sputtering produces a surface comprise of aluminum particles rather than those uniform aluminum films with a thickness of 100s um normally used to create AAO or those annealed aluminum surface which are seemed as non-crystal. And the cubic

particles sizes of about 300~500nm in Fig 2.3 A are similar in shape with those original sputtered aluminum particles. A possibility exists that the alumina particles (shown in Fig 2.3) are derived from sputtered aluminum particles (shown in Fig 2.1A). The size increase of these cubic alumina particles (300~500nm) from original aluminum particles (70~150nm) can be due to: 1) the crystal unit size increase after Al growing to Al_2O_3; 2) the introduction of alumina channels help increase particle size. From Fig 2.3 B to Fig 2.3 E, it also can be observed that pores are formed within the scale of the aluminum particles. It is probably that the individual aluminum particles produced by sputtering form as the surface unit when alumina grows. During the growing process, successive aluminum supply for further alumina growth only comes from the individual alumina particles rather than the whole aluminum films. Different from those annealed aluminum or aluminum films with a uniform surface on which the whole aluminum surface acts as successive aluminum supply source for alumina growth, the naturally formed nonconductive alumina on surface between the individual sputtered aluminum particles forms as a gap for one aluminum particle to supply the other when alumina grows. Therefore, the original aluminum particles size is one of the factors (anodizaiton voltage, electrolyte, and so on) which determine or limit alumina pore sizes. This is also the reason when etching time beyond 60 mins, the surface become destroyed.

2.2.3 Preparation of chemical treated commercial alumina membrane and glass-supported alumina

treated alumina surfaces were prepared by refluxing the samples in 1, 2-dichloroethane solutions containing 0.03 M trifluoroacetic acid. The refluxing was carried out at 60 ^{o}C for 2 h. After removal of samples from the solutions, they were rinsed with de-ionized water and dried in oven at 45 ^{o}C before further analysis. The same procedure was used for chemical treatment of alumina surface with perfluoropentanoic acid and 2, 3, 4, 5, 6-pentafluorobenzoic acid. The chemically treated surfaces were characterized using Kratos X-ray Photoelectron Spectroscopy AXIS Instrument.

2.2.4 Preparation of chemically grafted etched glass-supported alumina films

As described in section 3.3, the glass-supported alumina film was etched before the chemical modification procedure, in order to improve the chemical modification process. Etching was carried out as described above in section 2.2.2 with the etching time of 30 mins. The same chemical treatment process of alumina same as section 2.2.3 was carried out on the etched glass-supported alumina films. The chemically treated surfaces were characterized under Kratos X-ray Photoelectron Spectroscopy AXIS Instrument.

2.3 Contact angle measurement on chemically grafted etched glass-supported alumina films

Contact angle measurements were carried out on etched glass-supported alumina surface with different pore sizes before and after surface modification by $CF_3(CF_2)_3COOH$. The specimen has been placed in vacuum oven overnight to thoroughly remove water residue

in alumina before measurements. The measurements were taken at five different locations along the alumina surface.

2.4 Atomic Force Microscopy Force-Distance study on chemically grafted alumina surface

AFM force-distance plot measurements were carried out to study alumina surface property before and after the chemical modification procedure. As in contact angle measurements, the surface has to be placed overnight in vacuum oven at room temperature to ensure the specimens were thoroughly dried before AFM force-distance plot measurements. The AFM force-distance plot studies were carried out using Digital Instrument from Veeco® Metrology Group Digital under ambient conditions.

2.5 Atomic Force Microscopy study on chemically grafted alumina surface adsorbed with Immunoglobulin.

1.5μg ml-1 IgG (Mouse monoclonal anti-GST) solution was made in pH 7 PBS buffer, containing 0.1M NaCl. IgG solution was added on both chemically modified and unmodified commercial alumina membranes from Whatman® membrane with 200nm pores, acting as templates for adsorption of IgG. The adsorption time takes 20mins. A control using chemically unmodified alumina and buffer solution without IgG, was carried out under the same experimental conditions. All samples were rinsed thoroughly with de-ionized water after the adsorption procedure, and dried under nitrogen gas before further measurement under AFM.

Chemically grafted commercial alumina surfaces with perfluoropentanoic acid with pore size of 200nm were soaked in anti-Glucose Oxidase (anti-GOX) IgG solution with different concentration for IgG adsorption. Available concentrations include 0.4 μg ml^{-1}, 0.8 μg ml^{-1}, 1.6 μg ml^{-1}, 2.4 μg ml^{-1}, and 3.2 μg ml^{-1}. The adsorption time takes 30mins. After that, the surface was air dried before studied under AFM. Atomic Force Microscopy (AFM) studies were carried out using tapping mode under ambient conditions, from Digital Instrument from Veeco Metrology Group.

2.6 QCM study of IgG adsorption on aluminum oxide.

The 8MHz quartz crystals are bought from CH Instruments respectively. Mouse monoclonal antibody (IgG2b-kappa, clone GST 3-4C) raised against the 26 kDa GST proteins from S. japonica, supplied by ZYMED laboratories Inc. as a 200 ml aliquot at a concentration of 0.5 mg/ml in PBS, pH 7.4, containing 0.1% sodium azide (NaN3), and was used as received.

The gold surface of quartz crystal was cleaned by piranha solution (3:1 concentrated sulphuric acid to hydrogen peroxide) for half hour at 70°C to remove any impurities on the surface. The quartz was then washed with D.I. water and ethanol and dried with nitrogen gas. About 390 nm Al (according to the thickness measured in section 2.2.2) was sputtered on quartz crystal by period of 3600 sec sputtering under RF sputtering (Discovery®-18 Sputtering System) using a 99.999% Al target in an argon atmosphere.

The quartz crystal is held in a vertical orientation between O-rings in a Teflon cell holder and connected to an oscillator. The frequency is recorded by Autolab GPES 4.7 software. The QCM cell was fitted with the Al-sputtered quartz crystal and stabilized in 5ml of D.I. water. There was a negative drift and it takes typically 5h for the baseline to stabilize. After the baseline had relatively stabilized, an aliquot of IgG (in the range of 4uL to 32uL) was added to the water with stirring to ensure even distribution of the IgG molecules within the solution). The frequency shift was then monitored with time, until a plateau was reached.

Chapter 3

Surface treatment of alumina

3.1 Introduction

Commercial membrane filters are available in many different specifications, including pore size, pore density, flexibility and hydrophilicity. It is clear that these properties are determined by the membrane materials, besides the methods of fabrication. Among these membrane filters, nano-porous alumina membranes are widely employed for a variety of applications. These applications include solvent filtration for high-performance liquid chromatography, liposome extrusion, micro- and nano-meter filtration. Increasingly, nano-porous alumina membranes have been applied in non-filtration related applications such as templates for synthesis of nano-wires[27,28] and nano-rods[29], support for cell cultures[30] and microscopy studies, and recently, as high surface area support for lipid bilayer formation. All these latter applications rely on the same properties which make alumina an attractive material for filtration applications, that is, its high pore density of about 1x1010 pores cm^{-2}, narrow pore size distribution, chemical and thermal stability, as well as its rigid support structure.

Substrate supported nano-porous alumina prepared from electrochemical anodization has its advantages of well controlled pores with variable diameters and high pore densities which have found wide use as templates for growth of nanostructure materials and catalysis. However, there is little research carried out on chemical grafting of nano-porous alumina membranes and substrate-supported alumina prepared from electrochemical anodization of aluminum. Chemical grafting of alumina surfaces would further enhance its performance in filtration and non-filtration applications, in which variation of surface property is desirable.

Alumina made from anodization of aluminum sheets have been grafted with poly(ethylene) glycol by activation of the hydroxyl terminal groups using chlorosilane and later covalent coupling with trace –OH groups on the alumina[21,22]. Other groups have generally approached chemical grafting of alumina membranes by direct functionalizing with organo-chlorosilanes with the surface –OH [23] groups on the alumina [24]. These two approaches are generally adopted for grafting of silicon-based surfaces with organic compounds. Recently it has been shown that using high pressure vials, physical adsorption of organo-carboxylic acids was achieved on alumina powders and aluminum sheets covered with surface oxides (α-alumina) derived from air oxidation [25]. We modify this approach and apply it to commercial alumina (γ-alumina) membranes as well as alumina films made in-house using electrochemical anodization. The reaction is a simple one-pot process which yields a stable product with evidence which presently suggests chemical covalent bond formed between the carboxylate groups of organo-carboxylic acids and the surface –OH groups of alumina.

Herein, we describe a process [21] to modify the alumina surfaces, both commercial alumina membrane and sputtered alumina films, as the two surfaces were thought to be the same type of alumina both made of anodized aluminum. And these grafted surfaces show different effect on adsorption behavior of an immunoglobulin molecule.

3.2 XPS study of chemically treated commercial alumina membrane

The alumina membrane surfaces after different chemical treatment using the procedure described in section 2.4 were studied using XPS on Al 2p, C 1s, and F 1s respectively. A

common convention is to put saturated, un-functional C 1s at 284.5 eV which could be assigned to hydrocarbon contamination in XPS chamber. Here, all the curves has been fitted by assigned to C 1s = 284.5 eV.

XPS study of F 1s peaks on chemically treated commercial alumina surfaces are given in Fig. 3.1. It is apparent that on un-treated bare commercial alumina surface, there is no F 1s peak observed. After the surface was treated with three different fluorinated carboxylic acids, different intensities of F 1s peaks appear at about 688 eV, confirming the presence of a layer of fluorinated group on the chemically treated commercial alumina surface. Detailed peak parameters have been summarized in Table 3.1. The positions of F 1s allocate at 687.971 eV, 688.403 eV and 687.772 eV of CF_3COOH, $CF_3(CF_2)_3COOH$ and C_6F_5COOH respectively. It is reasonable for the different F 1s peak position that on C_6F_5COOH, because of the conjugative effect on benzene ring, there is negative shift of ~0.2 eV compared with F 1s peak position of CF_3- on $CF_3(CF_2)_3COOH$. Moreover, the FWHM (A full width at half maximum) of F 1s on C_6F_5COOH is about 0.3 eV less than the other two, which also due to the benzene ring effect. In addition, F 1s peak on CF_3COOH is shifted by -0.5 eV relative to F 1s on $CF_3(CF_2)_3COOH$. It is because that on CF_3COOH, the electron-withdrawing effect of C=O group imposed on CF_3-, whereas on $CF_3(CF_2)_3COOH$, this electron-withdrawing effect is shared with $CF_3(CF_2)_3$-. However, as the electron-withdrawing effect of C=O group execute indirectly on F- (by affecting adjacent C), the shift is not large and within 0.5 eV.

Figure 3.1 XPS study of F 1s on commercial alumina membrane

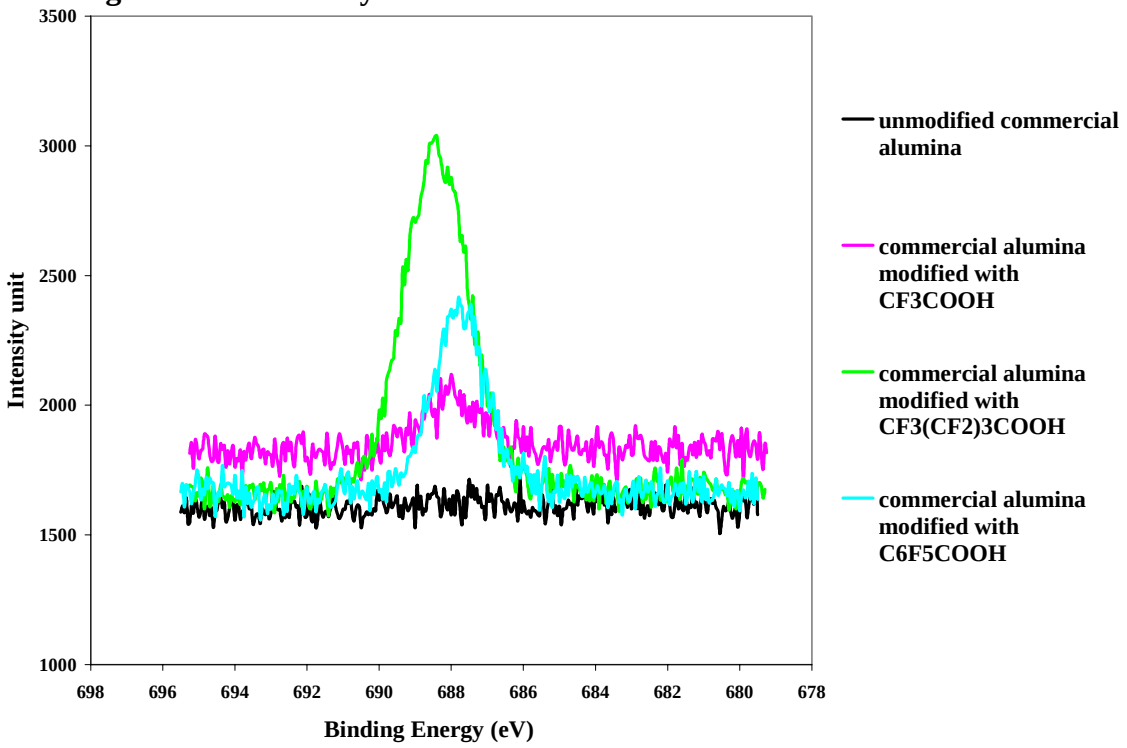

Table 3.1: parameters of F 1s peak on commercial alumina surface treated by different fluorinated carboxylic acid.

	F 1s of CF_3COOH	F 1s of $CF_3(CF_2)_3COOH$	F 1s of C_6F_5COOH
BE(eV)	687.971	688.403	687.772
FWHM(eV)	2.05	2.09	1.75

Table 3.2: Atomic concentration of F and Al by XPS on commercial membrane

	Commercial alumina membrane treated with CF_3COOH	Commercial alumina membrane treated with $CF_3(CF_2)_3COOH$	Commercial alumina membrane treated with C_6F_5COOH
F atomic concentration (%)	0.93	4.40	3.02
Al atomic concentration (%)	16.98	12.99	16.38
F/Al atomic concentration ratio	0.055	0.339	0.184

Table 3.2 shows the atomic concentrations of fluorine F and aluminum Al on the surfaces of commercial alumina membrane samples, after treatment with three different types of

fluorinated organic acids. It is clear from Table 3.2 that the atomic concentration ratio of F to Al on the surface of alumina membrane sample treated with $CF_3(CF_2)_3COOH$ is nearly twice that of the surface treated with C_6F_5COOH. This is not surprising since there are 9 F atoms on $CF_3(CF_2)_3COOH$ molecule compared to only 5 F atoms on $CF_3(CF_2)_3COOH$. However, the surface atomic concentration ratio of F to Al for alumina membrane sample treated with CF_3COOH is considerably much lower than the samples treated with $CF_3(CF_2)_3COOH$ and C_6F_5COOH. This is inconsistent with the relative numbers of F atoms in the organic acids. Clearly, this suggests a lower surface coverage by CF_3COOH compared to $CF_3(CF_2)_3COOH$ and C_6F_5COOH.

Raw XPS spectra of Al 2p (Fig. 3.2) indicate ~0.35 eV shifts in the peaks after chemical treatment of the commercial alumina membrane samples with the organic acids. We fitted the Al 2p peaks using the original peak position of the un-treated alumina at 74.26 eV and obtain shifts of the second peak after surface treatment with the three different types of fluorinated carboxylic acids (Fig 3.3 A~D). In Fig. 3.3 A~D, peak 1 are the original Al 2p peak with the same position as in un-treated alumina, and peak 2 are the split Al 2p peaks caused by chemical treatment. These shifts of Al 2p ranging from between ~0.6-0.9 eV clearly indicate chemical shifts [31], indicative of a covalent grafting process which probably occurs on oxygen atoms adjacent to aluminum atoms.

Figure 3.2 XPS study of Al 2p on commercial alumina membrane

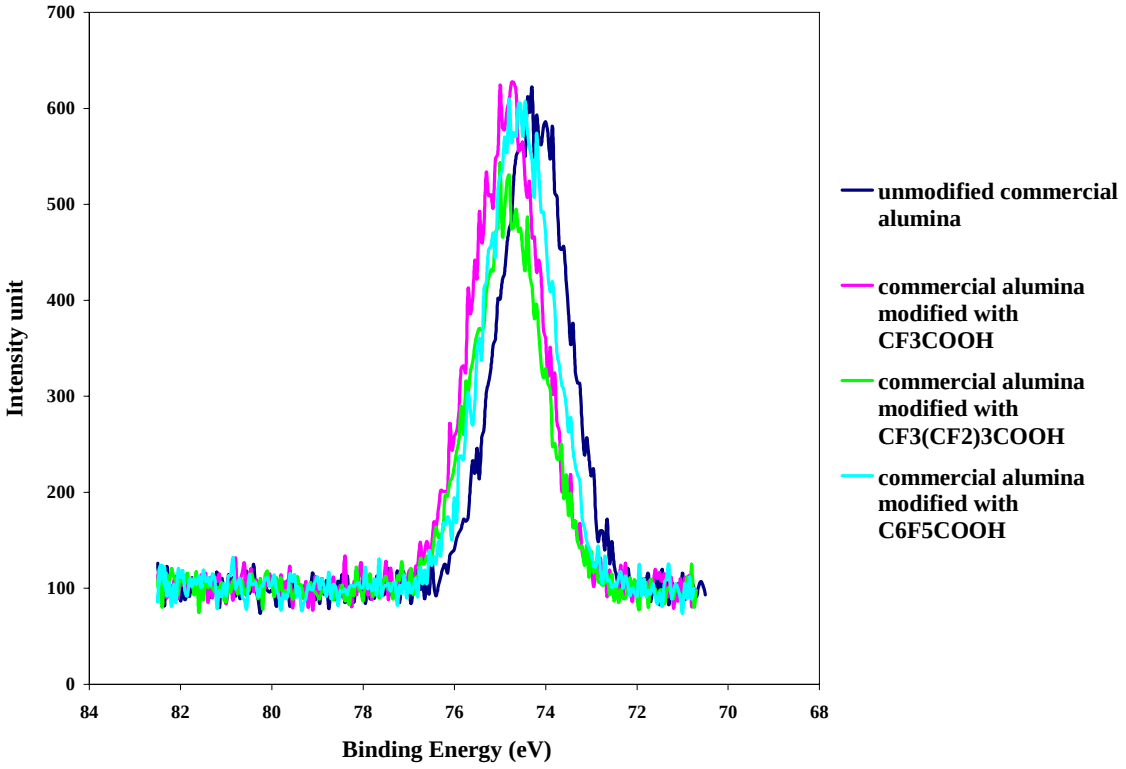

Table 3.3: Al 2P peak shift of treated surfaces

	Commercial alumina treated with CF_3COOH	Commercial alumina treated with $CF_3(CF_2)_3COOH$	Commercial alumina treated with C_6F_5COOH
Original Al 2p position (eV)	74.26		
Al split peak (eV)	75.14	74.85	75.04
Peak shift (eV)	0.88	0.59	0.78

Figure 3.3 A XPS study of Al 2p on un-treated commercial alumina membrane

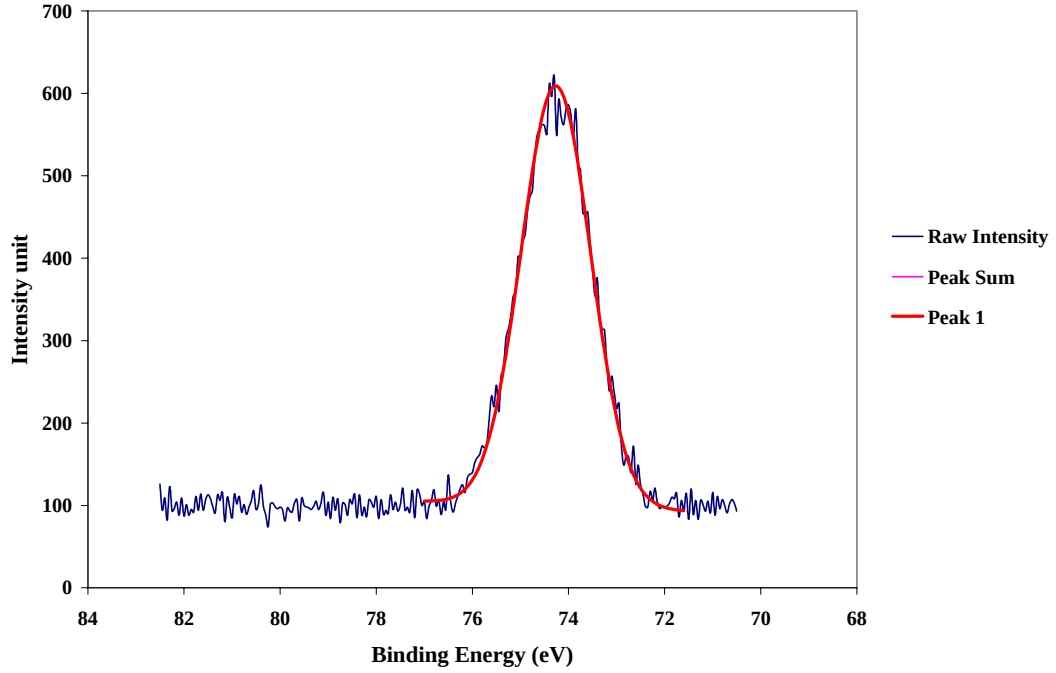

Figure 3.3 B XPS study of Al 2p on CF_3COOH-treated commercial alumina membrane

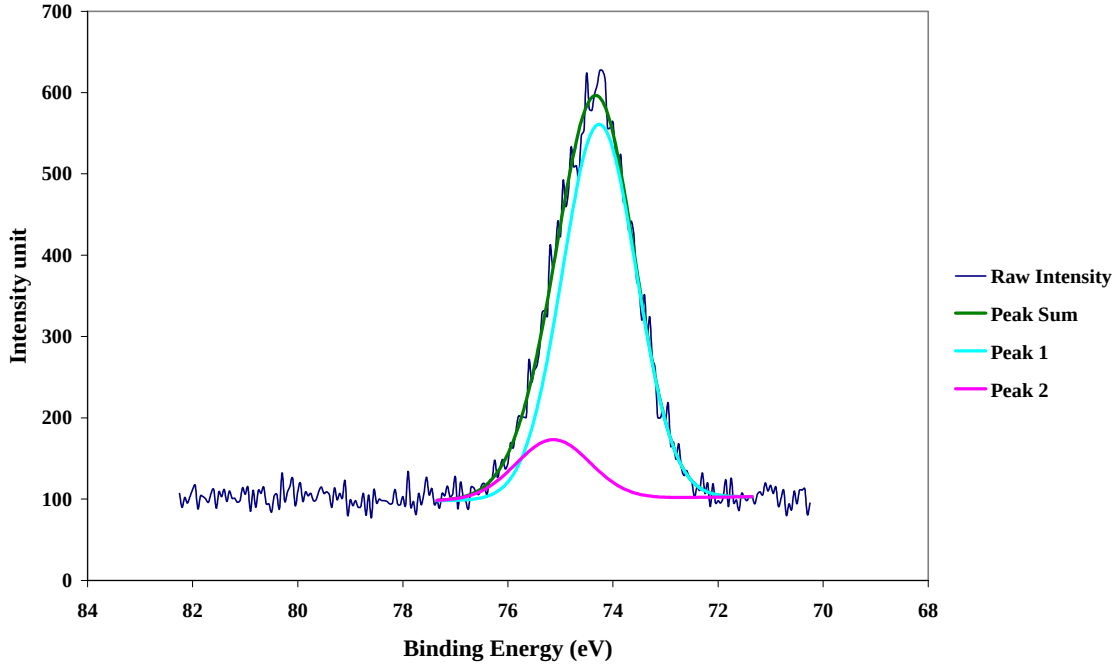

Figure 3.3 C XPS study of Al 2p on $CF_3(CF_2)_3COOH$-treated commercial alumina membrane

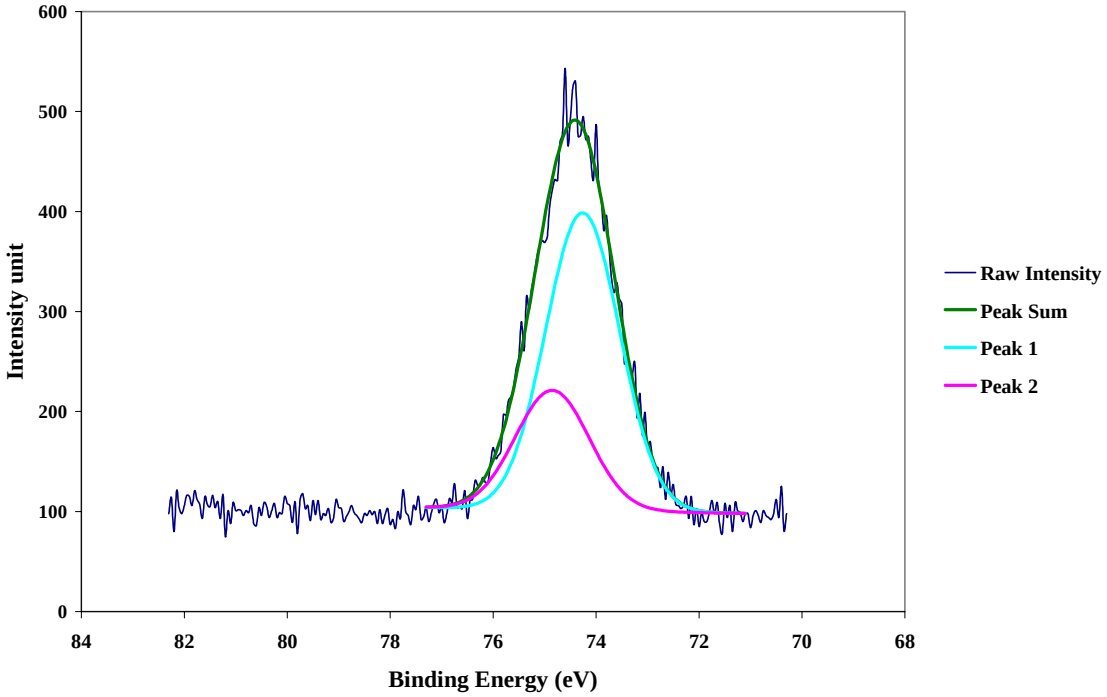

Figure 3.3 D XPS study of Al 2p on C_6F_5COOH-treated commercial alumina membrane

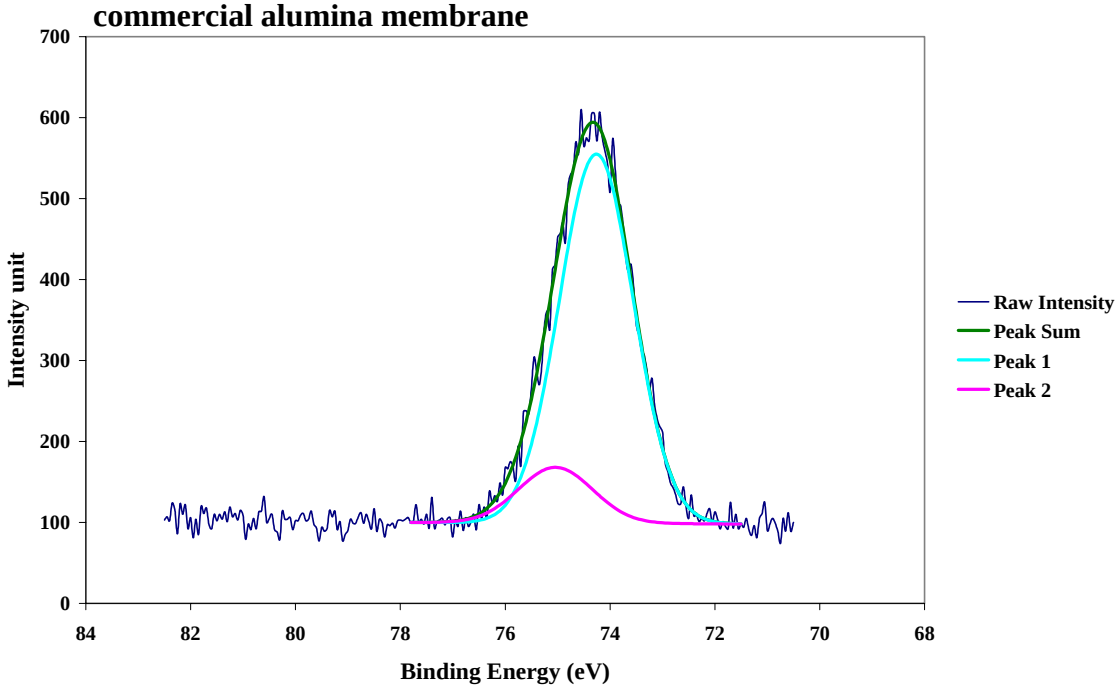

Spectra in Fig. 3.4 A~D are XPS study of C 1s on chemically treated alumina surfaces compared to the un-treated ones. An obvious peak at low BE which can be observed in all these four spectra is assigned to hydrocarbon contamination and is set to 284.5 eV. It is apparent that in Fig.3.4 C, the peak at highest BE of 293.52 eV indicates the C 1s peak of CF_3- group, and second highest BE of 290.94 suggests C 1s peak of CF_2- group. Moreover, in Fig.3.4 D, the peak at 289.32 eV is C 1s of CF on benzene ring. Whereas, on bare alumina surface (Fig 3.4A), these peaks appear at high BE corresponding to CF_3 is absent. Similarly, in Fig.3.4B, CF_3COOH-treated commercial alumina surface does not show such peaks with high BE of more than 290 eV. This is probably due to the limited amount of CF_3- group indicated in Fig.3.1 is covered by or combine with carboxylic group presented at 288.87 eV.

In Conclusion, XPS studies on F 1s, C 1s, and Al 2p indicate that commercial alumina surfaces are grafted with three kinds of fluorinated carboxylic acid.

Figure 3.4 A XPS study of C 1s on untreated commercial alumina membrane

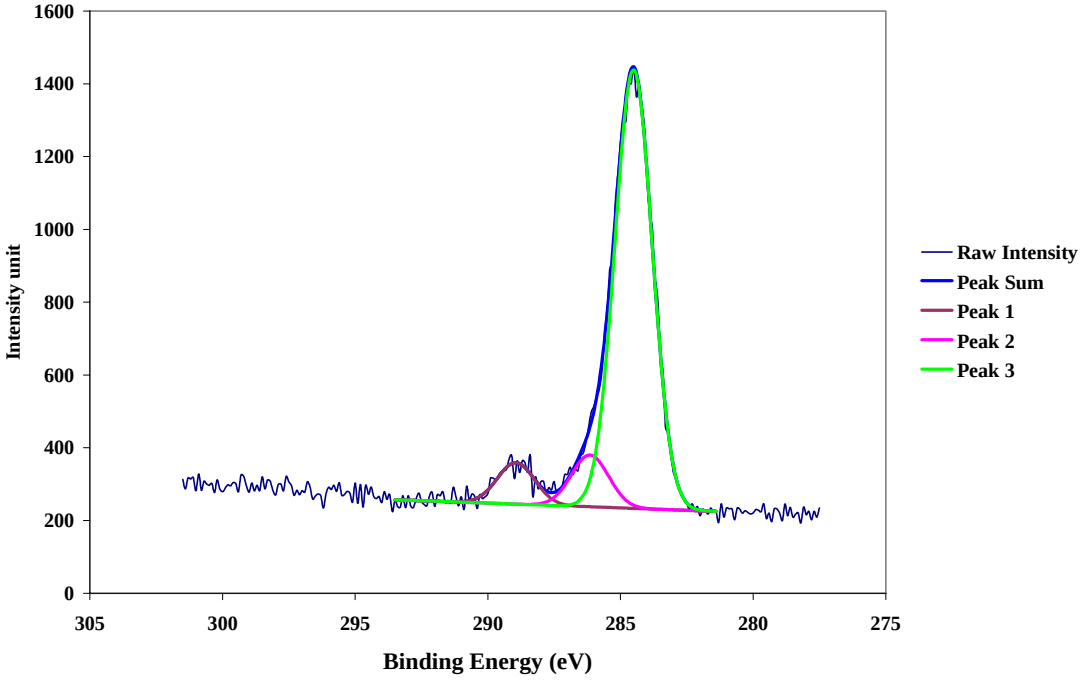

Figure 3.4 B XPS study of C 1s on CF3COOH-treated commercial alumina membrane

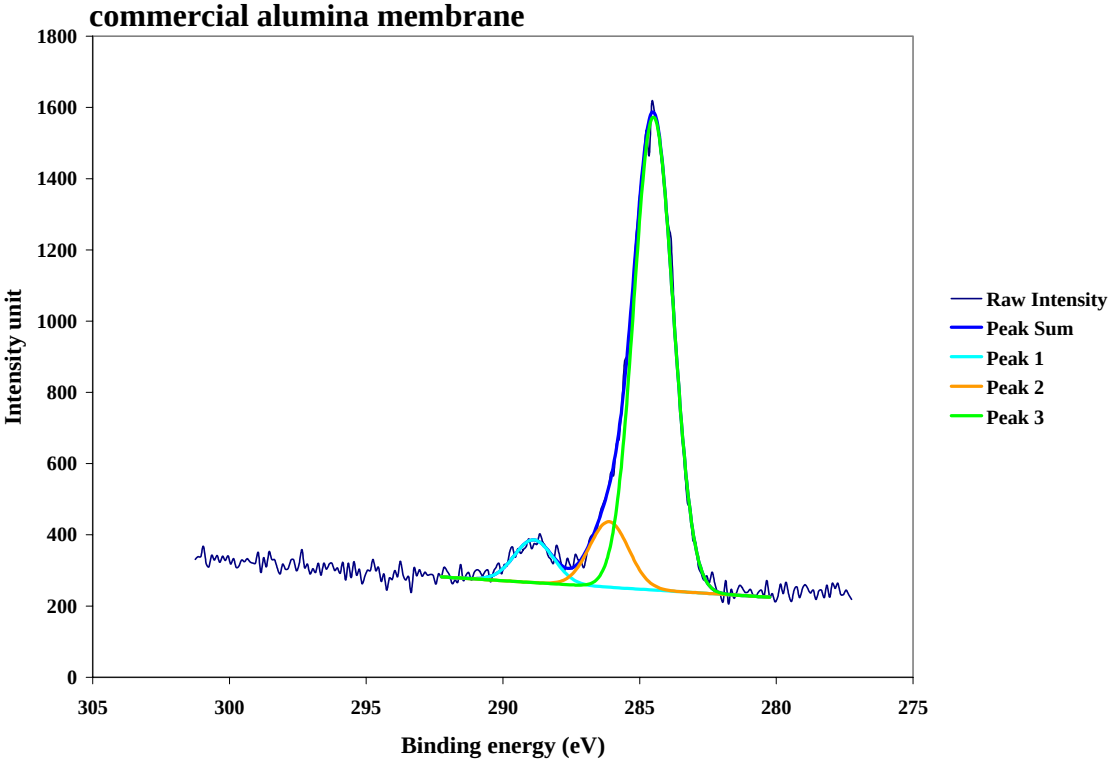

Figure 3.4 C XPS study of C 1s on $CF_3(CF_2)_3COOH$-treated commercial alumina membrane

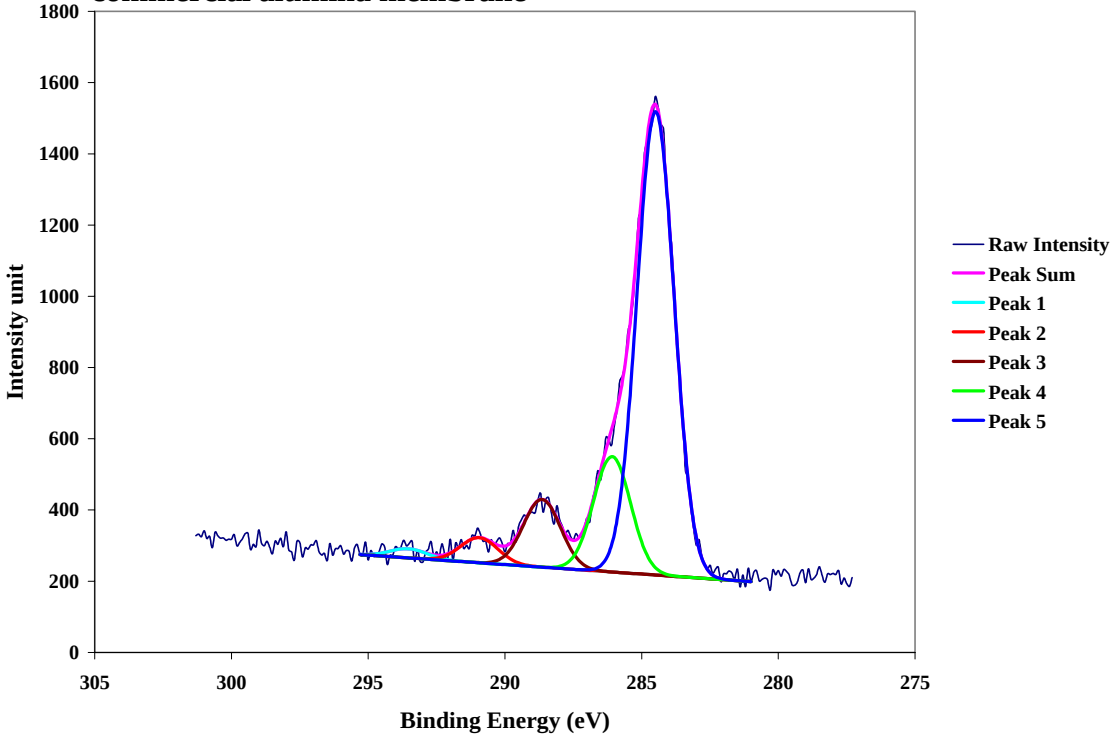

Figure 3.4 D XPS study of C 1s on C_6F_5COOH-treated commercial alumina membrane

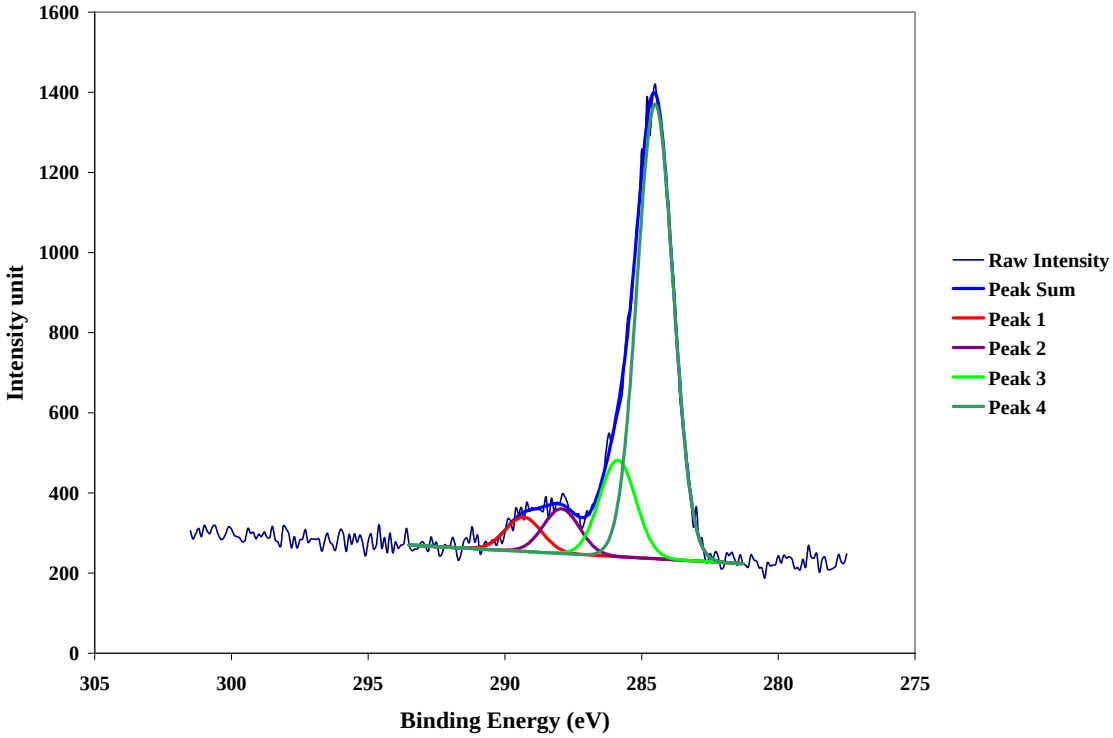

3.3 XPS study of chemically treated Glass-supported alumina film

The glass-supported alumina films after different chemical treatment were studied by XPS on Al 2p, C 1s, and F 1s respectively. A common convention has been exerted to saturated, un-functional C 1s at 284.5 eV which could be assigned to hydrocarbon contamination in XPS chamber. Here, all the curves has been fitted by assigned to C 1s = 284.5 eV.

Figure 3.5 XPS study of F 1s on glass-supported alumina film.

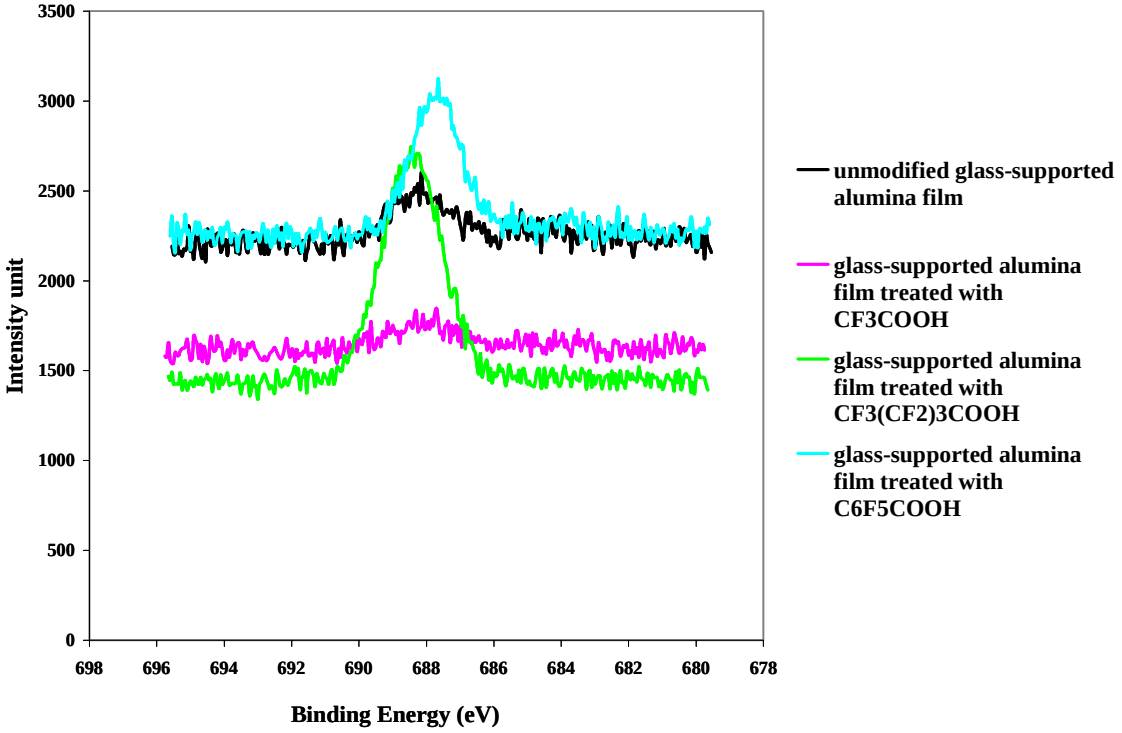

Figure 3.6 XPS study of Al 2p on glass-supported alumina film.

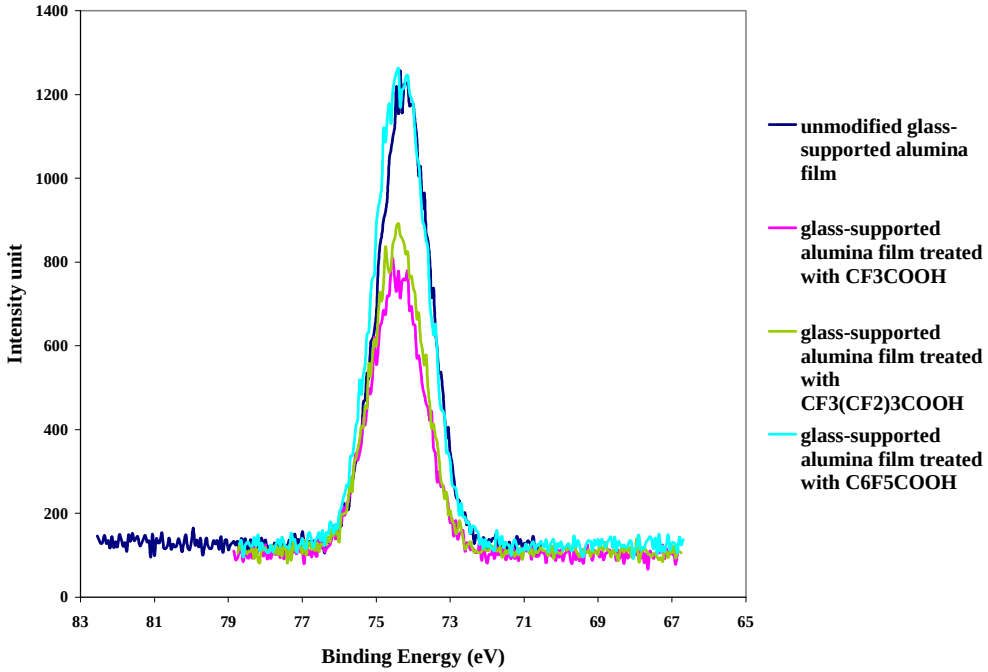

Figure 3.7 A XPS study of Al 2p on un-treated glass-supported alumina film

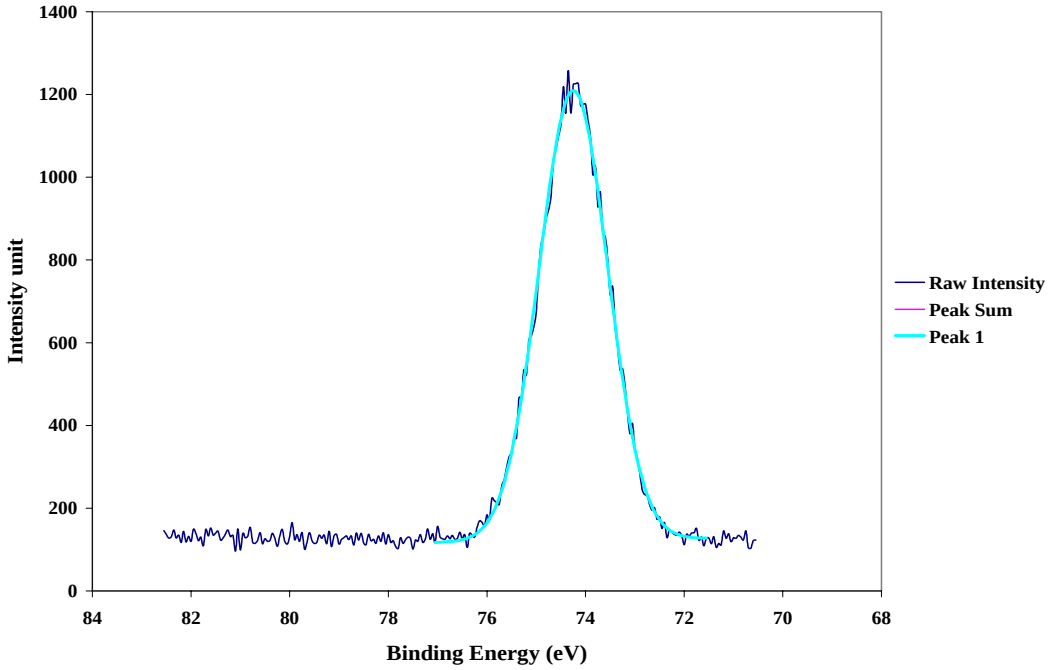

Figure 3.7 B XPS study of Al 2p on CF_3COOH-treated glass-supported alumina film

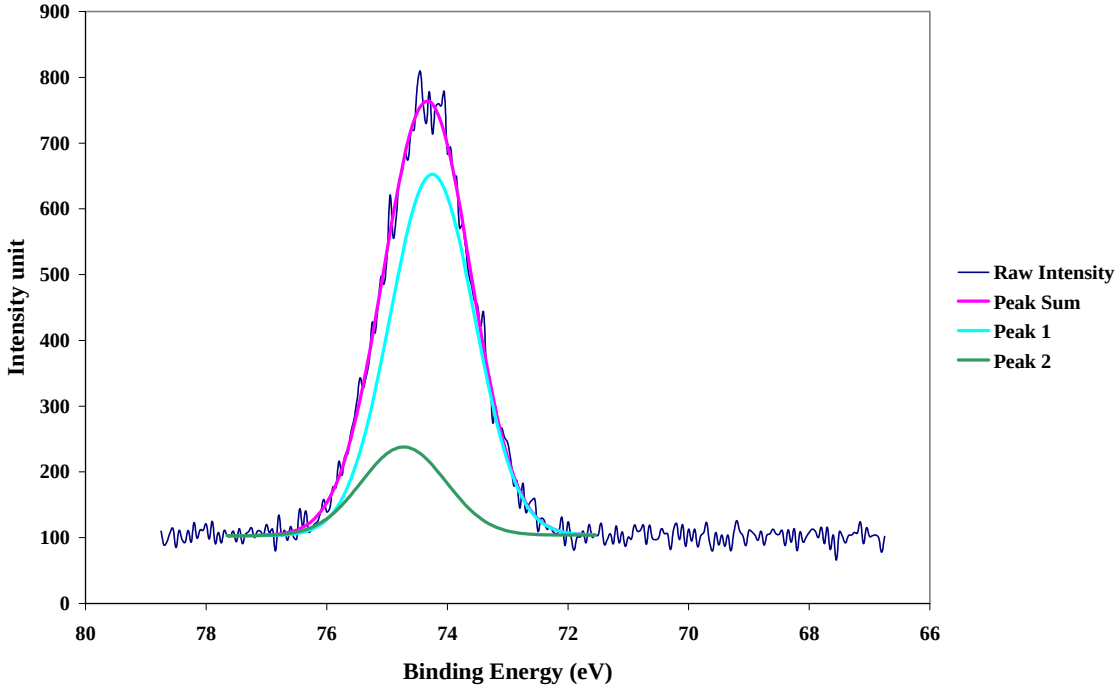

Figure 3.7 C XPS study of Al 2p on $CF_3(CF_2)_3COOH$-treated glass-supported alumina film

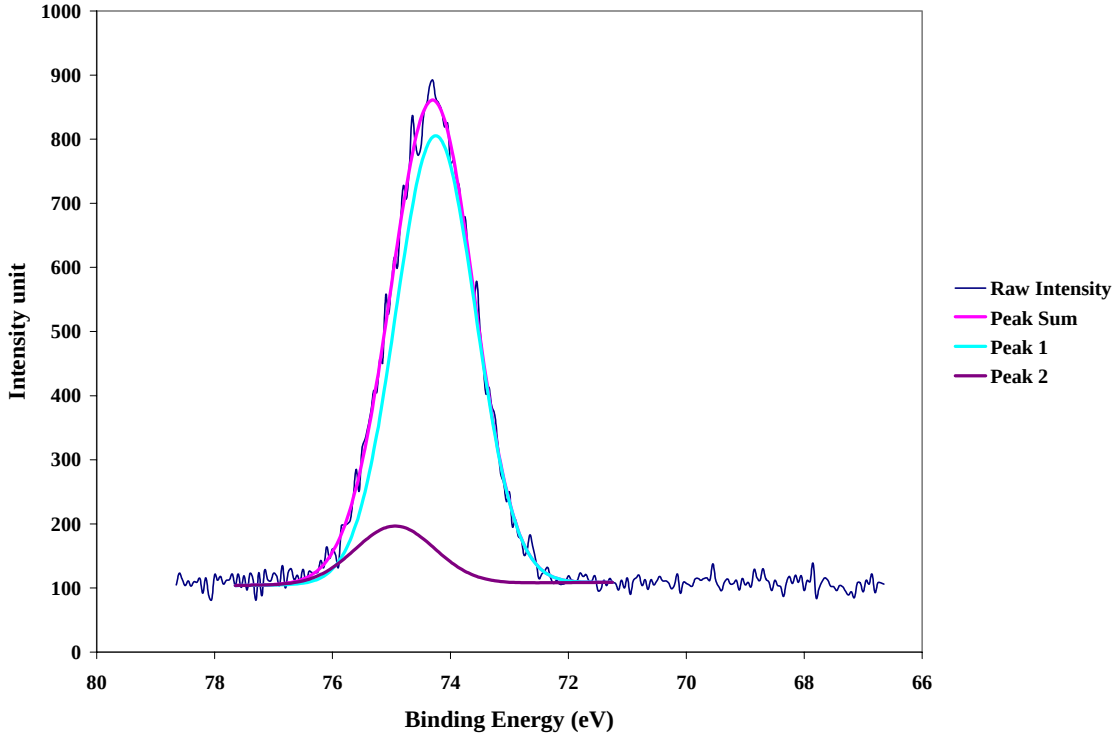

Figure 3.7 D XPS study of Al 2p on C_6F_5COOH-treated glass-supported alumina film

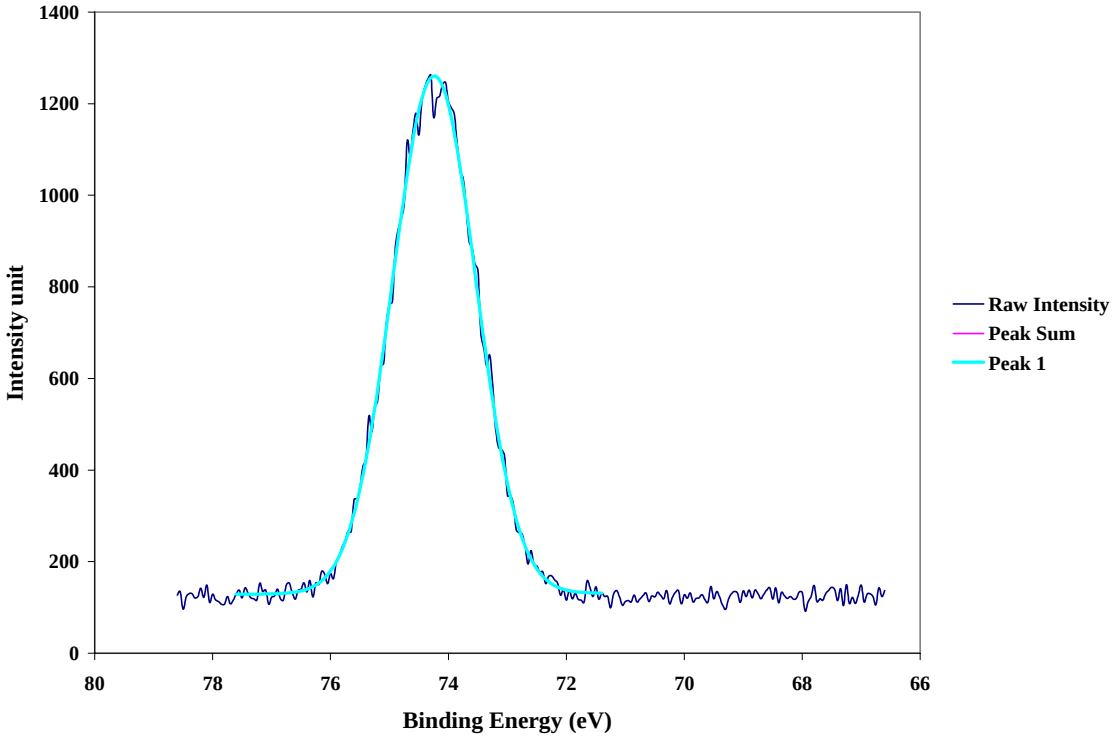

Figure 3.8 A XPS study of C 1s on un-treated glass-supported alumina film

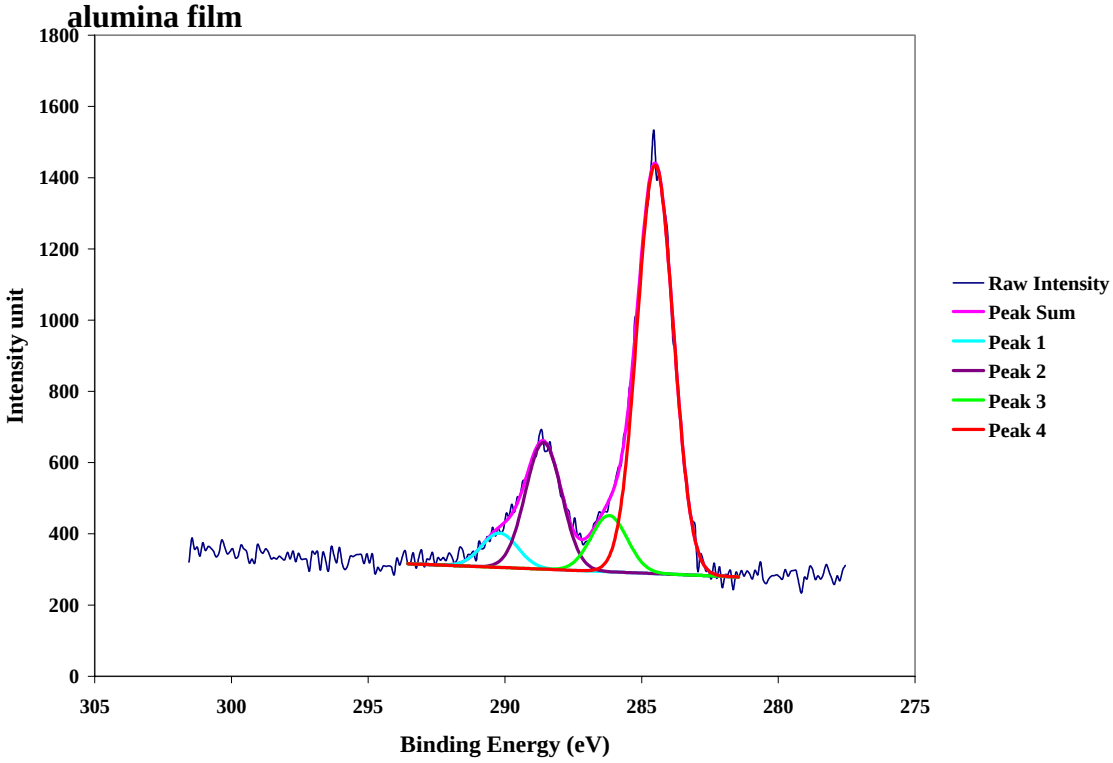

Figure 3.8 B XPS study of C 1s on CF_3COOH-treated glass-supported alumina film

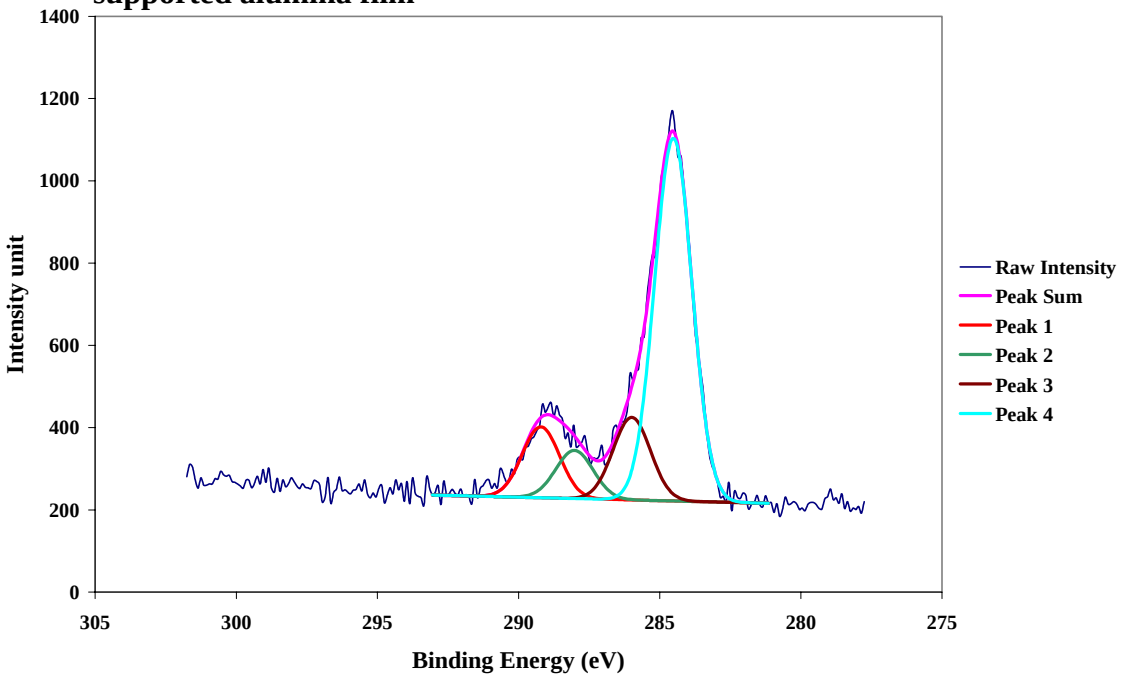

Figure 3.8 C XPS study of C 1s on $CF_3(CF_2)_3COOH$-treated glass-supported alumina film

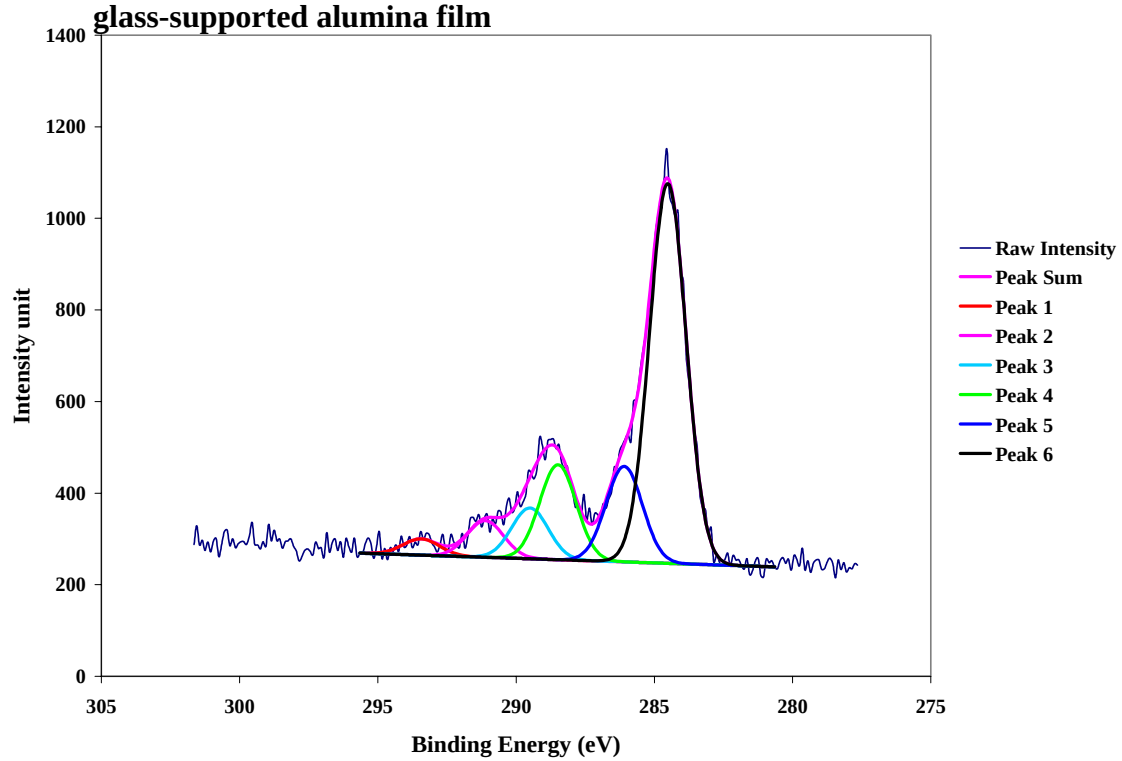

Figure 3.8 D XPS study of C 1s on C_6F_5COOH-treated glass-supported alumina film

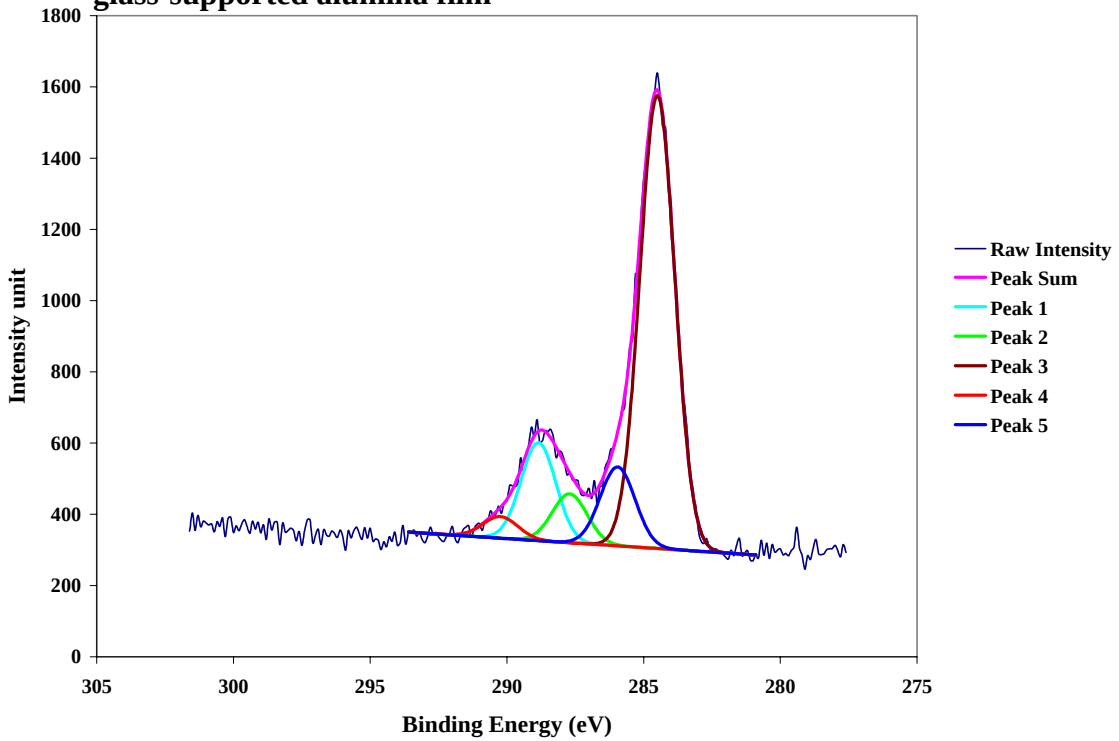

Table 3.4: Atomic concentration of F and Al by XPS on glass-supported alumina film

	glass-supported alumina film treated with CF_3COOH	glass-supported alumina film treated with $CF_3(CF_2)_3COOH$	glass-supported alumina film treated with C_6F_5COOH
F atomic concentration (%)	0.82	4.38	1.56
Al atomic concentration (%)	19.58	19.95	21.80
F/Al atomic concentration ratio	0.042	0.220	0.072

Table 3.5 Al 2p peak shift of treated glass-supported alumina surface

	glass-supported alumina film treated with CF_3COOH	glass-supported alumina film treated with $CF_3(CF_2)_3COOH$	glass-supported alumina film treated with C_6F_5COOH
Original Al 2p position (eV)	74.25		
Al split peak (eV)	74.73	74.94	-
Peak shift (eV)	0.48	0.69	-

When the same chemical treatment method was applied to glass-supported alumina film samples, it is noted that in comparison with results obtained for commercial alumina membranes treated with different fluorinated carboxylic acid (Tab.3.2), glass-supported alumina surfaces yield lower values of the F/Al concentration ratio (Tab. 3.4). Meanwhile, it yields a slightly different result as shown in Table 3.2. The results in Table 3.4 indicate that the surface atomic concentration ratio of F to Al on the surface treated with CF_3COOH is about one-fifth compared with that of the one treated with $CF_3(CF_2)_3COOH$, which is similar with commercial membrane samples. However, the atomic concentration ratio of F to Al on the surface treated with C_6F_5COOH is considerably lower than half of atomic concentration ratio of F to Al on the surface treated with $CF_3(CF_2)_3COOH$, suggesting a lower surface coverage of C_6F_5COOH on glass-supported alumina film compared with commercial membrane. It can be concluded that $CF_3(CF_2)_3COOH$ is the best organic modifier on both commercial membrane and glass-supported alumina film, giving the highest surface coverage.

Spectra in Fig. 3.8 A~D are XPS study of C 1s on on chemically treated glass-supported alumina compared to the un-treated ones. An obvious peak at low BE which can be observed in all these four spectra is assigned to hydrocarbon contamination and is set to 284.5 eV. Similarly with Fig. 3.4, in Fig.3.8 C, the peak at highest BE of 293.43 eV indicates the C 1s peak of CF_3- group, and second highest BE of 291.112 suggests C 1s peak of CF_2- group; in Fig. 3.8 D, the peak at 290.24 eV is C 1s of CF on benzene ring. Whereas, on un-treated glass-supported alumina surface (Fig 3.8 A), these peaks appear at high BE corresponding to CF_3 is absent.

A particular kind of C 1s peak around ~288 eV can be found on each glass-supported alumina surface in Fig. 3.8. To be in detail, the peak appears as peak 2 (288.58 eV) in Fig. 3.8A; peak 2 (288.02 eV) in Fig. 3.8 B; peak 4 (288.49 eV) in Fig. 3.8C; and peak 2 (288.85 eV) in Fig. 3.8D which are likely to be an additional carboxylic group other than the existing fluorinated carboxylic group. However, this kind of C 1s peak does not appear on commercial alumina membrane surface, as well as those treated with different fluorinated carboxylic acid. Since its appearance on un-treated glass-supported alumina surface, it is probably that this particular peak is coming from the substrate, and possibly formed when anodization carried out in oxalic acid.

Furthermore, shifts in the raw XPS spectra of Al 2p on these glass-supported alumina film (Fig. 3.6) are not observed as obvious as appears on commercial alumina surface which shown in Fig. 3.2. With the same method as used on commercial alumina surface, these Al 2p peaks are fitted using the original peak position of the un-treated glass-supported alumina surface. The obtained second Al 2p peak of CF_3COOH-treated glass-supported alumina surface (Tab.3.3) gives a much smaller shift compared with the one of commercial alumina surface which gives the number of 0.88 eV (Tab. 2.3). Moreover, there is not any second Al 2p peak can be figured out from C_6F_5COOH-treated glass-supported alumina surface. However, it is interesting to be found that on $CF_3(CF_2)_3COOH$-treated glass-supported alumina surface, this second Al 2p peak gives a even larger shift of 0.69 eV than that on commercial alumina with 0.59 eV. It is illustrated again that $CF_3(CF_2)_3COOH$ appears as a better modifier than the other two fluorinated carboxylic acid.

For the observation of both the decrease of Al 2p peak shift and lower F/Al concentration ratio given on these glass-supported alumina surface, we think this is due to exposure of the alumina surface to oxalic acid during the anodization process, which remain entrapped on the surface and interfere with the chemical reaction between carboxylic acids and surface Al-OH groups. Oxalic acid is known to form stable chelating bonds with metal ions and likewise, we think the remnant oxalic acid may have formed a stable surface layer on the alumina surface, thus hinder subsequent surface chemical reactions or physical-adsorption by fluoro-carboxylic acids. This postulate is supported by observation of unusually high proportion of COOH groups (represented by peak at 288.58 eV) present on the chemically un-treated glass-supported alumina film samples (Fig 3.8A), compared to the commercial alumina membrane samples (Fig 3.4A) as we discussed above. According to this postulate, we tried to use phosphoric acid to etch the glass-supported alumina in order to remove the contaminated outer surface, thus allowed the fresh alumina exposed to the chemicals. After etching of the glass-supported alumina film samples using phosphoric acid, the proportion of COOH groups decrease (Fig 3.12A) which will be discussed in the following section. We carried out chemical treatments of these etched samples with the same organic acids and using the same procedure as for the commercial alumina membrane samples.

In conclusion, the surface coverage of fluorinated carboxylic acid on glass-supported alumina surface is not as good as on commercial alumina. It is highly suspected that the surface remnant from oxalic acid when anodization prohibit the further surface reaction with fluorinated carboxylic acid.

3.4 XPS study of chemically treated Etched glass-supported Alumina films

The etched glass-supported alumina films after different chemical treatment were studied by XPS on Al 2p, C 1s, and F 1s respectively.

Figure 3.9 XPS study of F 1s on etched glass-supported alumina

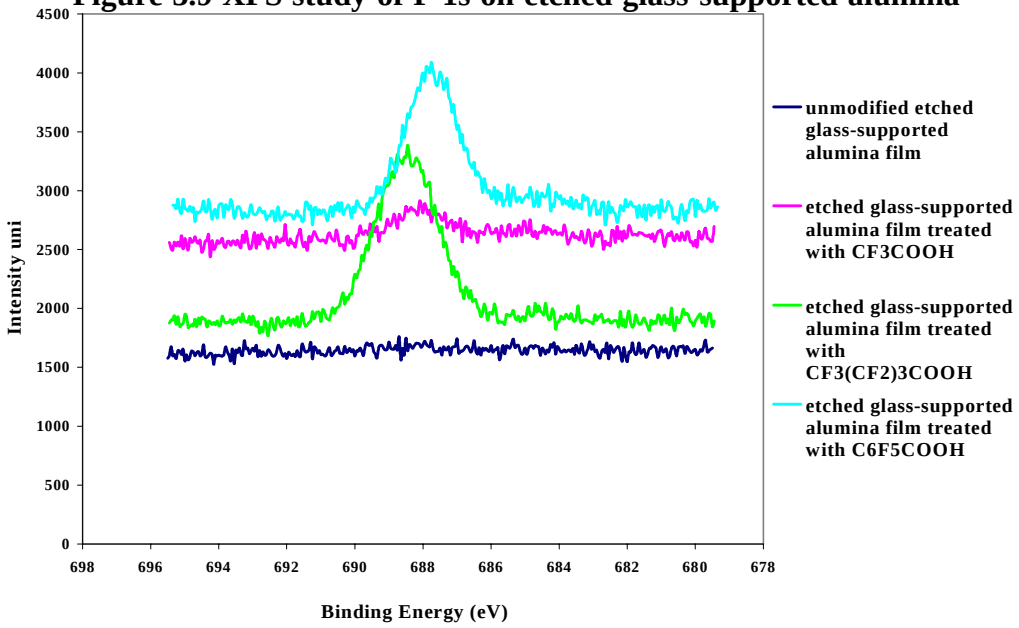

Figure 3.10 XPS study of Al 2p on etched glass-supported alumina film

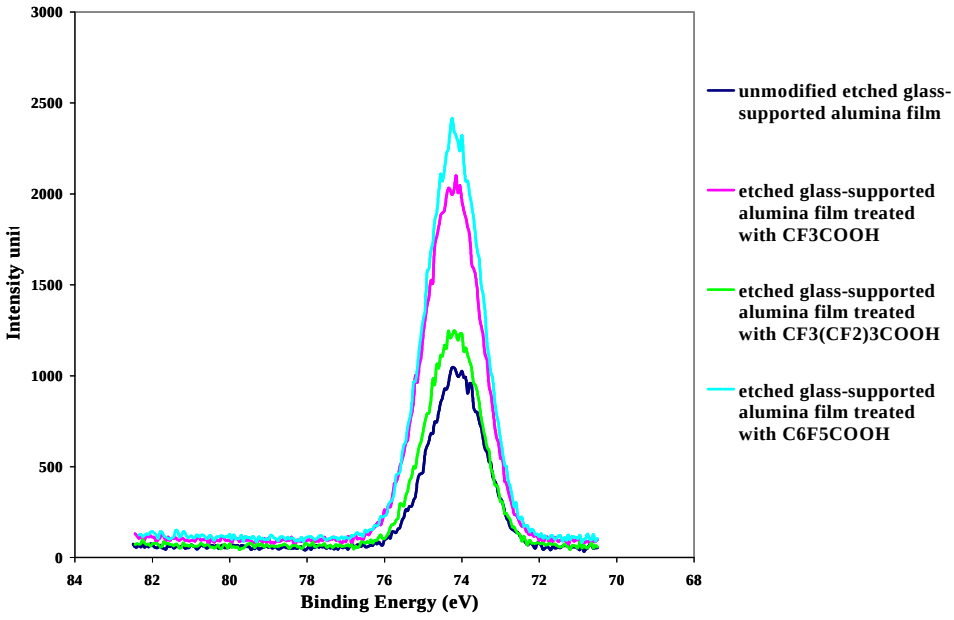

Figure 3.11 A. XPS study of Al 2p on un-grafted etched glass-supported alumina film.

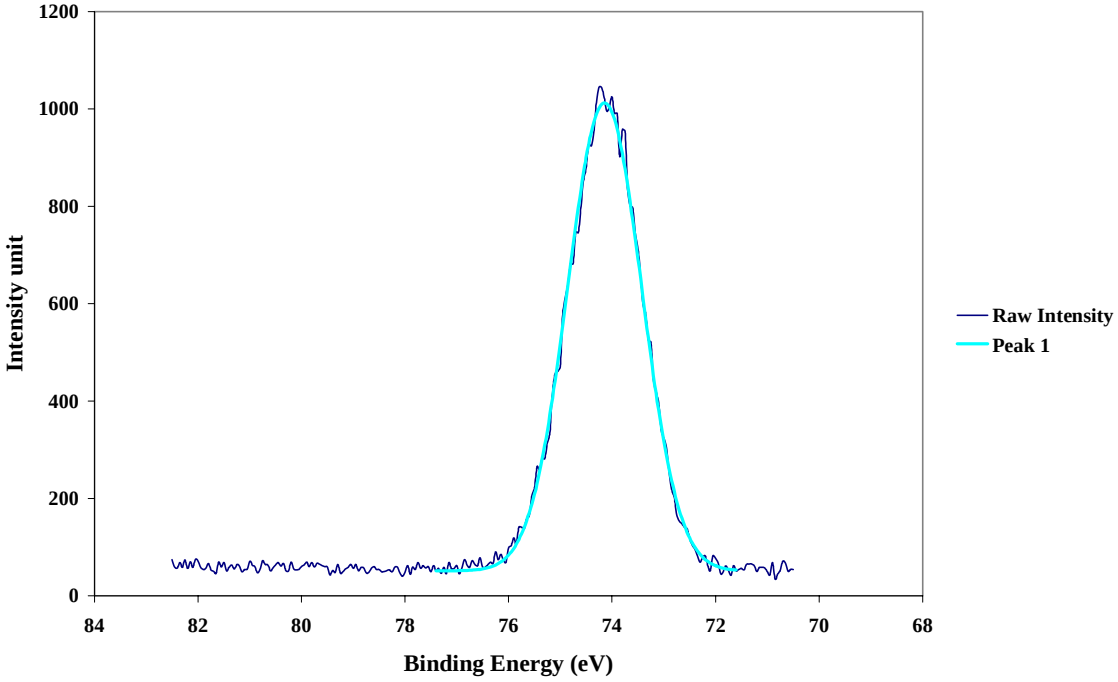

Figure 3.11 B. XPS study of Al 2p on CF_3COOH-treated etched glass-supported alumina film

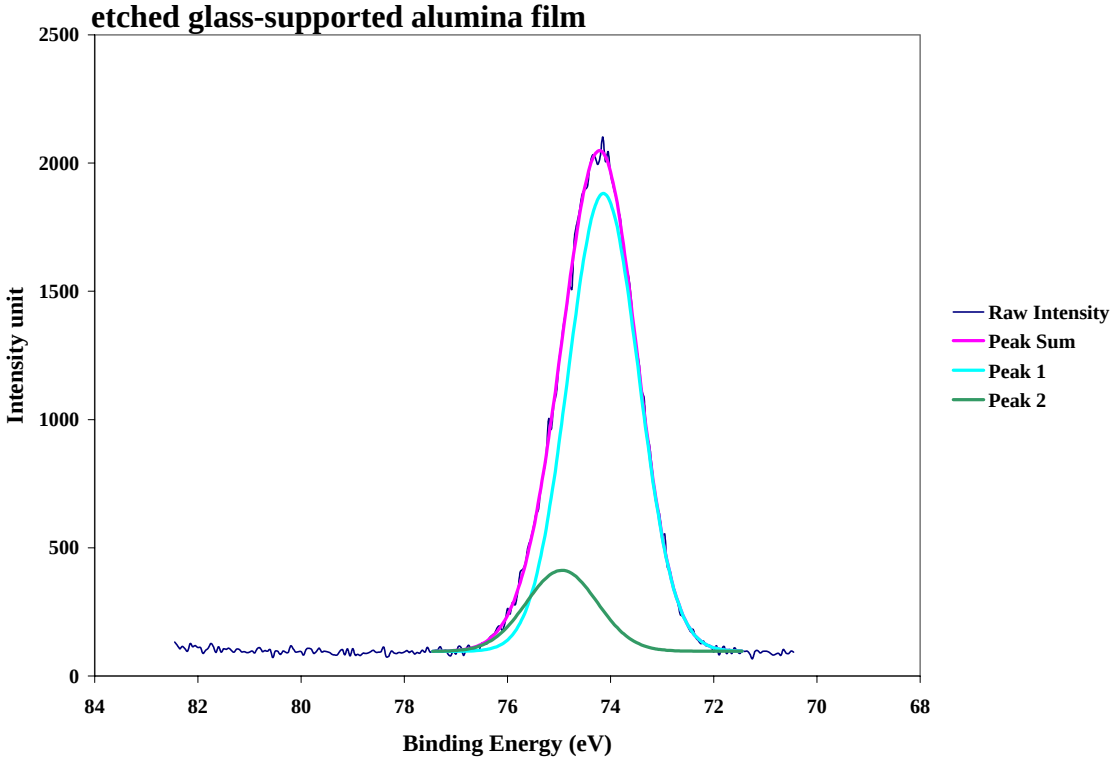

Figure 3.11 C. XPS study of Al 2p on $CF_3(CF_2)_3COOH$-treated etched glass-supported alumina film

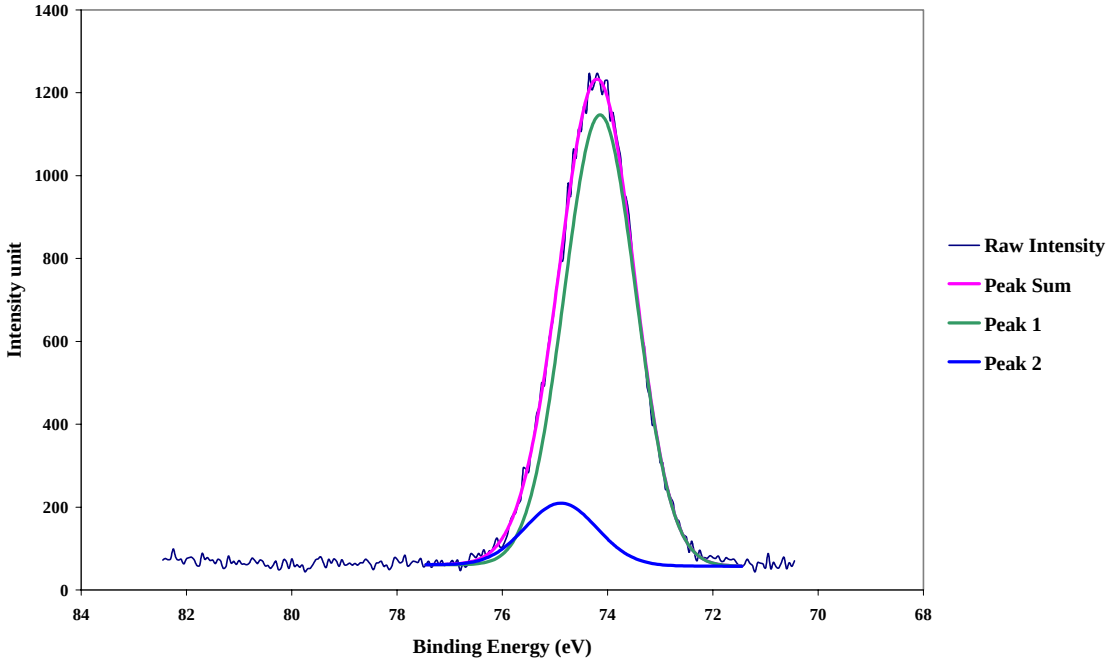

Figure 3.11 D XPS study of Al 2p on C_6F_5COOH-treated etched glass-supported alumina film

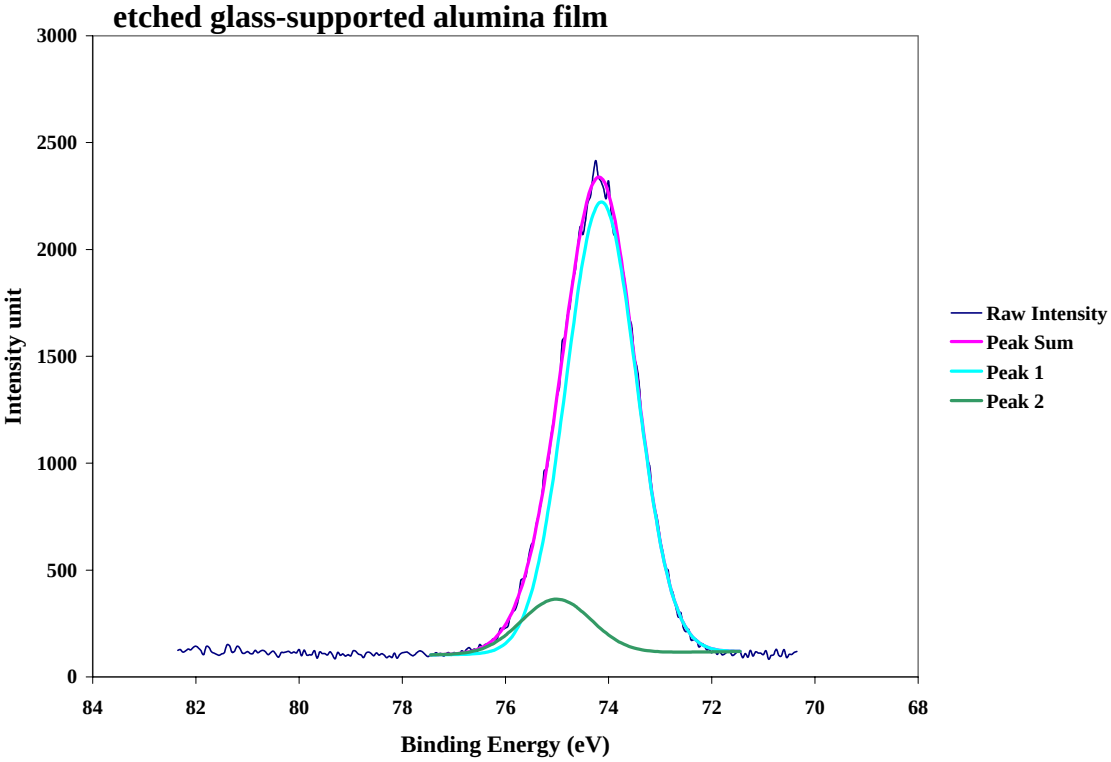

Figure 3.12 A. XPS study of C 1s on un-treated etched glass-supported alumina film

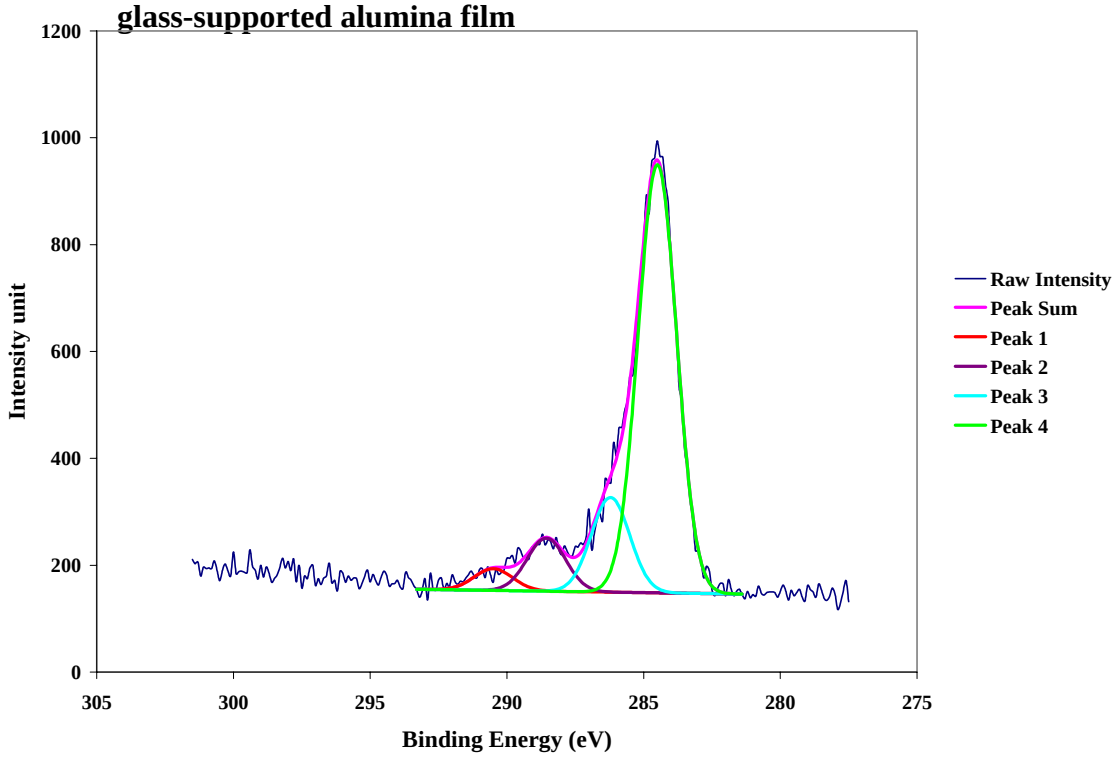

Figure 3.12 B. XPS study of C 1s on CF_3COOH-treated etched glass-supported alumina film

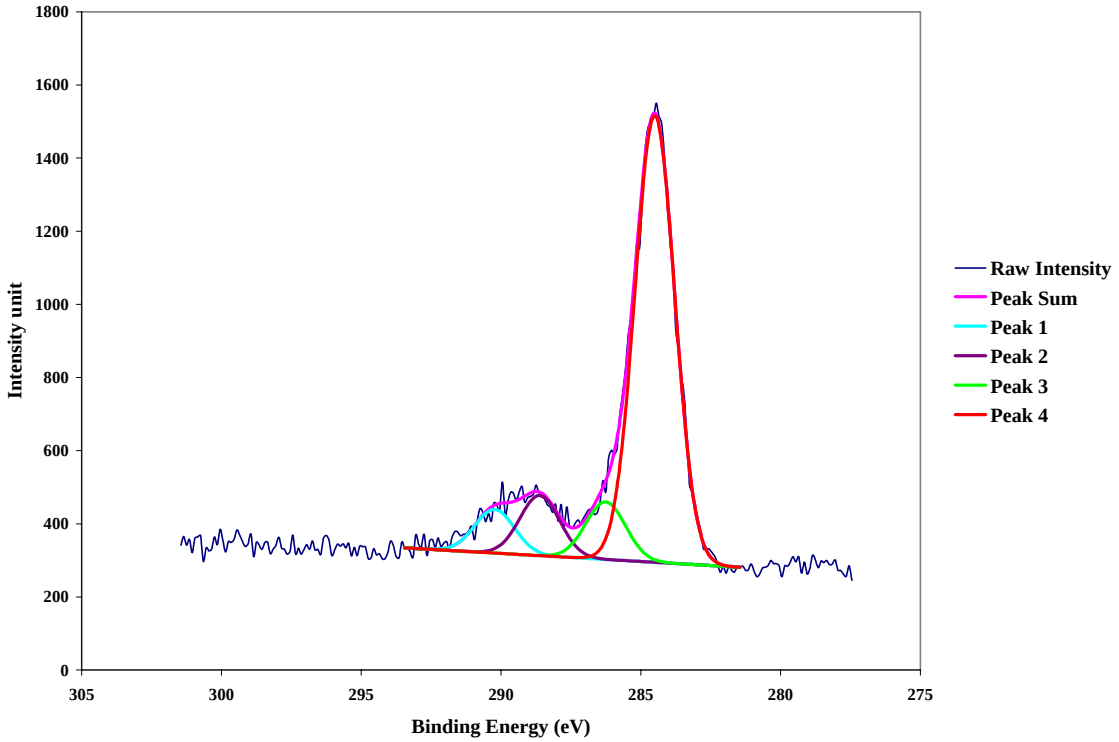

Figure 3.12 C. XPS study of C 1s on $CF_3(CF_2)_3COOH$-treated etched glass-supported alumina film

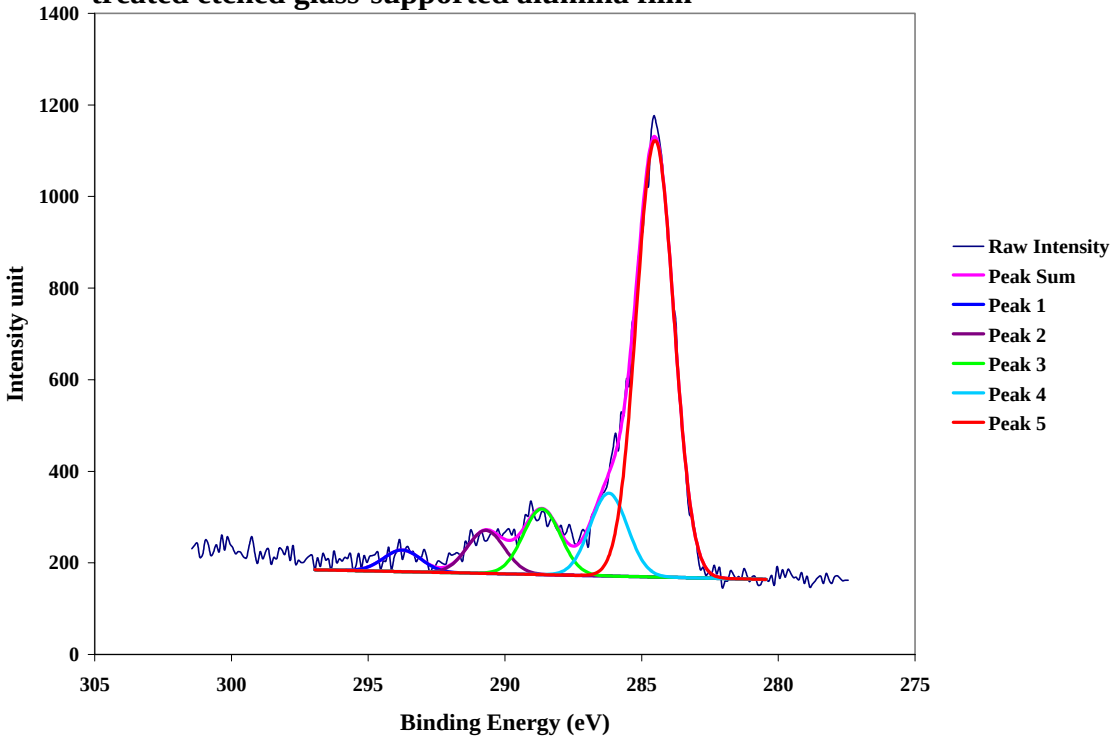

Figure 3.12 D. XPS study of C 1s on C_6F_5COOH-treated etched glass-supported alumina film

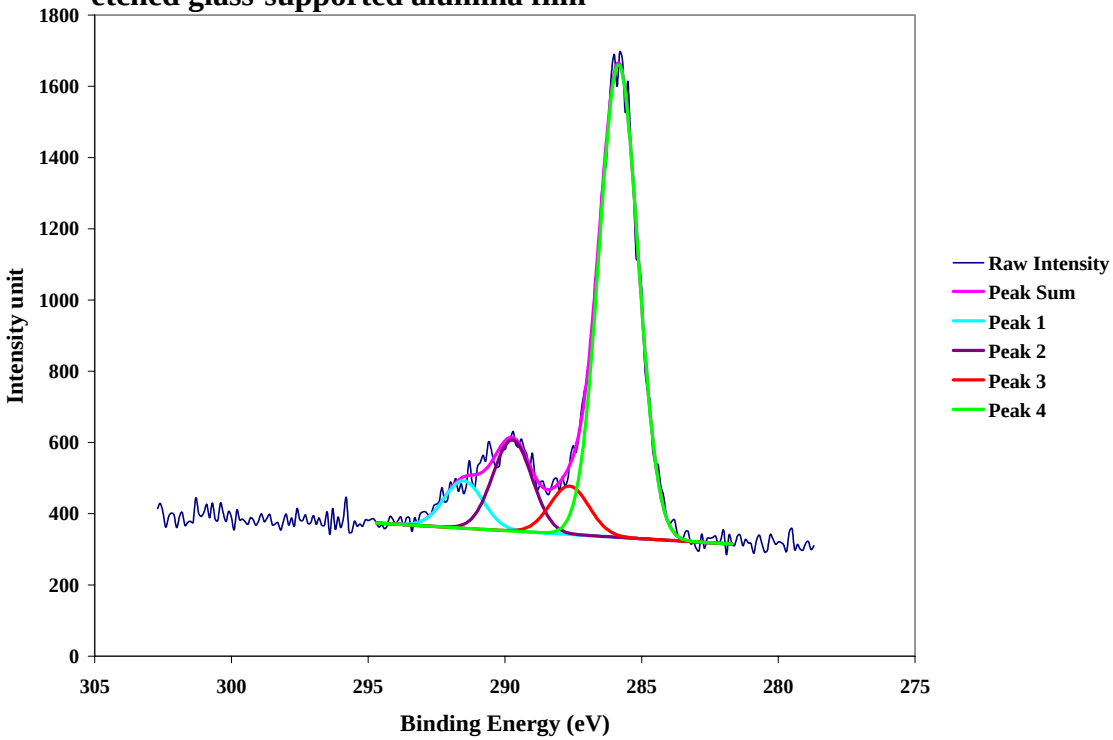

Table 3.6: Atomic concentration of F and Al by XPS on etched glass-supported alumina film

	Etched glass-supported alumina film treated with CF_3COOH	Etched glass-supported alumina film treated with $CF_3(CF_2)_3COOH$	Etched glass-supported alumina film treated with C_6F_5COOH
F atomic concentration (%)	0.65	3.83	1.85
Al atomic concentration (%)	24.83	27.73	24.70
F/Al atomic concentration ratio	0.026	0.138	0.075

Table 3.7: Al 2P peak shift of treated etched glass-supported alumina surfaces

	Etched glass-supported alumina film treated with CF_3COOH	Etched glass-supported alumina film treated with $CF_3(CF_2)_3COOH$	Etched glass-supported alumina film treated with C_6F_5COOH
Original Al 2p position (ev)	74.14		
Al split peak (ev)	75.15	74.88	75.01
Peak shift (ev)	1.01	0.74	0.87

Table 3.6 gives the quantitative XPS results on the F/Al ratios of these etched glass-supported alumina samples. These F/Al ratios are still lower compared to the commercial alumina membrane chemically treated with the corresponding acids (refer to Table 3.2 for comparison). However, when comparing the F/Al ratios between the different acids, it is clear the etched glass-supported alumina samples undergo surface treatments in much the same way as the commercial alumina membrane samples. For examples, the results indicate that etched glass-supported surface atomic concentration ratio of F to Al on the surface treated with $CF_3(CF_2)_3COOH$ is about 1.84 times of atomic concentration ratio of F to Al on the surface treated with C_6F_5COOH, which is the same as commercial membrane samples. The ratio is reasonable as the atomic number of F in $CF_3(CF_2)_3COOH$ is 1.8 times of the one in C_6F_5COOH. Meanwhile, the atomic

concentration ratio of F to Al on the surface treated with CF_3COOH is about one-fifth compared with that of the one treated with $CF_3(CF_2)_3COOH$, which is similar to that observed in the commercial membrane samples. Thus it can be concluded that both $CF_3(CF_2)_3COOH$ and C_6F_5COOH give higher surface coverage compared to CF_3COOH on commercial membrane and etched glass-supported alumina films.

Spectra in Fig. 3.12 A~D are XPS study of C 1s on chemically treated glass-supported alumina compared to the un-treated ones. The obvious peak at low BE is assigned to hydrocarbon contamination and set to 284.5 eV for all the samples. Similarly with Fig. 3.4, in Fig.3.12C, the peak at highest BE of 293.75 eV indicates the C 1s peak of CF_3- group, and second highest BE of 290.70 eV suggests C 1s peak of CF_2- group; in Fig. 3.12D, the peak at 290.16 eV is C 1s of CF on benzene ring. Whereas, on un-treated glass-supported alumina surface (Fig 3.12A), these peaks appear at high BE corresponding to CF_3 is absent.

In addition, though the suspected carboxylic C 1s peak near 288 eV still exist on the etched glass-supported alumina surface (shown in Fig. 3.12A), when compared to un-treated commercial alumina surface (Fig. 3.4A), the intensity has been decreased to about 100 eV from about 400 eV on the un-treated glass-supported alumina surface (Fig. 3.8A). It is probably due to the surface etching by phosphoric acid which at the same time removes the carboxylic group from the surface.

In Fig. 3.11 A~D, interestingly, chemical treatment of glass-supported alumina film samples treated with phosphoric acid etch shows similar peak shifts in the Al 2p peak positions as chemically treated commercial alumina membranes. These second peaks are figured out based on best fits method as mentioned in Section 3.2&3.3 above. These second peaks shift from ~0.7 eV to ~1.0 eV (Tab. 3.7) indicating the chemical shifts which suggests the similar chemical grafting happened on commercial membrane alumina surface. Moreover, this clearly confirms our initial postulate that remnant species left on the anodized alumina films after anodization in oxalic acid inhibit the chemical grafting process. After decrease the carboxylic remnant species on anodized alumina surface, chemical grafting can take place finally.

Chemical grafting is thus best carried out on alumina surfaces which are freshly etched and the same chemical grafting can be achieved for both commercial alumina membranes and alumina films prepared from sputtered aluminum followed by electrochemical anodization.

3.5 Contact Angle measurement on chemical grafted etched glass-supported alumina

Table 3.8 shows contact angle results for glass-supported alumina film samples with different pores sizes, after thorough drying in oven at 120 ^{o}C. The results indicate increases in contact angles on alumina surface according to alumina pore size increase, suggesting an increase of hydrophobicity of the surface. However, the same trend is not observed for the chemically treated glass-supported alumina film samples.

Table 3.8: Contact angles measured on glass-supported alumina film samples with different pores sizes. Samples were placed in oven at 120^{o}C overnight and cooled to room temperature before measurements.

Etching time (min)	Bare alumina	treated with $CF_3(CF_2)_3COOH$
Bare alumina	83.1	105.0
20	96.3	103.5
30	98.1	98.6
40	111.1	111.7
50	111.4	104.2

Increasing pore sizes do not increase further the hydrophobic properties of these chemically treated films. The effects of increasing hydrophobicity by changing pore sizes and by chemical grafting are clearly not additive. This is not surprising since larger pore sizes means more contact with 'air pockets' within the pore channels. These 'air pockets' exert little attractive forces on water droplets and hence, an alumina sample with large pore sizes are similar to one in which the pore channels are filled with hydrophobic materials. Increasing pore sizes for the chemically treated alumina sample would have little effects on its hydrophobicity property if both the surface and the 'air-pockets' have similar low attractive forces for water. In addition, we found that at short etching time of 10 min, chemical treatment with $CF_3(CF_2)_3COOH$ does not yield the same surface hydrophobicity at all parts of the alumina sample. This is likely due to incomplete removal of the surface oxalic acids which hinder surface chemical reactions or physical-adsorption by fluoro-carboxylic acids as we have observed in the XPS studies above. Hence, contact angle measurements are carried out on glass-supported alumina samples etched at times longer than 10 mins.

This contact angle study indicates that chemical grafting of alumina films and membranes brings about changes in the surface hydrophobic property of alumina, whilst at same time, shows little variations despite changes in pore sizes. The consistent contact angles measured for these alumina samples possessing different pore sizes suggest strongly the possibility of using these chemically treated samples in applications requiring consistent surface hydrophobicity or in applications in which this property is critical to the application performance. Clearly, these results indicate the potential of varying other surface properties of alumina by choosing appropriate functional groups for the organic acids employed during the chemical treatment procedure.

3.6 AFM Force-Distance Plot study on chemically grafted commercial alumina surface

A silicon nitride probe used in AFM force-distance plot study is known as highly hydrophobic. As the tip diameter is normally 10~12 nm, the measurement is taken on single alumina grain rather than a surface comprise of a number of alumina grain and pores.

Fig. 3.13 Box plot of the force between AFM tip and chemically grafted alumina surfaces:

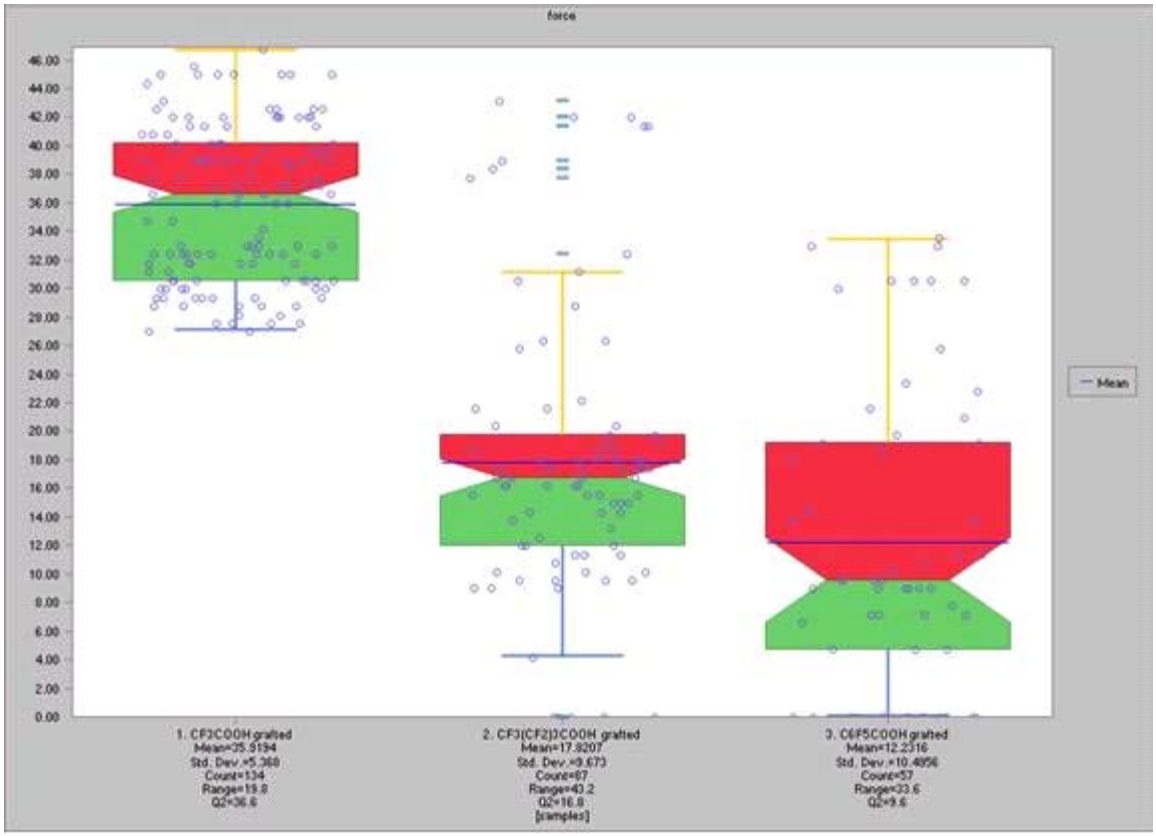

Table 3.9 Force distribution frequency of alumina surface as percentage of total number of measurements, grafted using three fluorinated carboxylic acids: CF_3COOH, $CF_3(CF_2)_3COOH$ and C_6F_5COOH respectively.

Range of the force	CF_3COOH	$CF_3(CF_2)_3COOH$	C_6F_5COOH
0	0%	5.75%	22.81%
>0~5nN	0%	1.15%	5.26%
>5~10 nN	0%	8.05%	28.07%
>10~15 nN	0%	21.84%	12.28%
>15~20 nN	0%	40.23%	8.77%
>20~25 nN	0%	5.75%	7.02%
>25~30 nN	19.40%	4.60%	3.51%
>30~35 nN	26.87%	3.45%	12.28%
>35~40 nN	26.12%	3.45%	0%
>40~45 nN	26.12%	5.75%	0%
>45 nN	1.49%	0%	0%

Figure 3.14 the force distribution percentage of alumina surface modified by three fluorinated carboxylic acid: CF_3COOH, $CF_3(CF_2)_3COOH$ and C_6F_5COOH respectively.

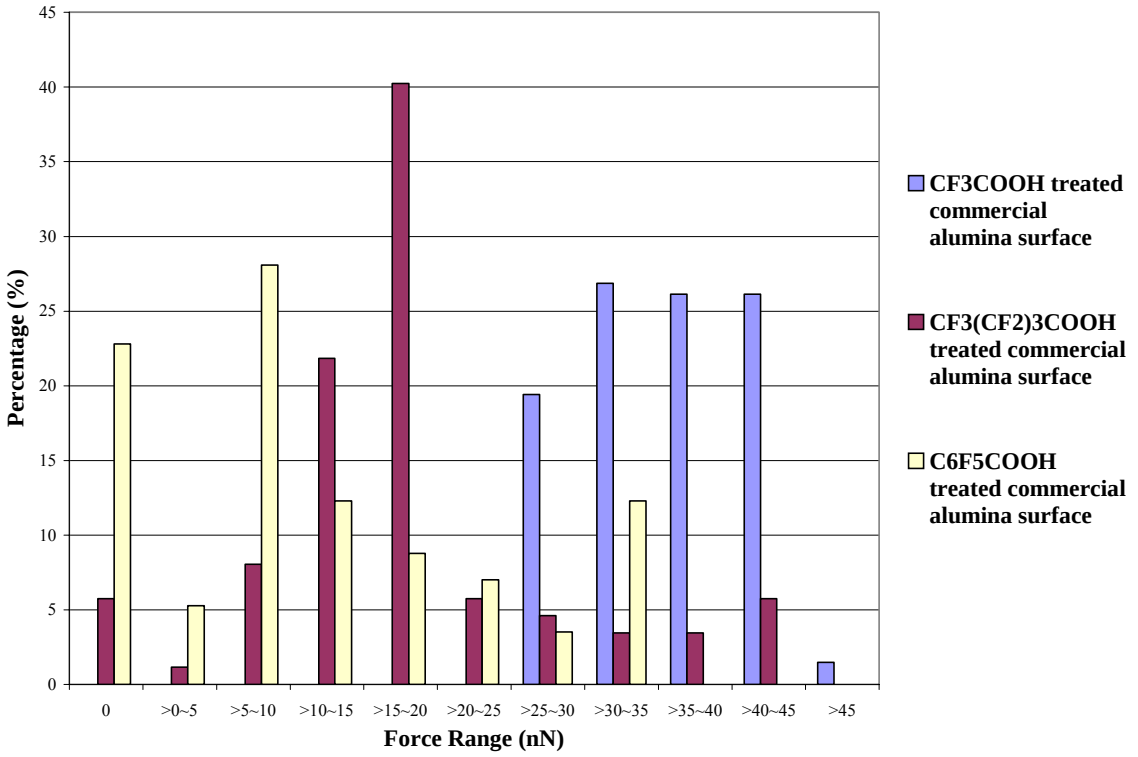

A force between the AFM probe and alumina surface is measured when the tip is retracted from the surface. At least five different areas of each grafted surface have been studied. The Fig. 3.13 gives the distribution of attractive forces between AFM probe and chemically grafted surfaces, as well as comparison among the differently treated surfaces. Table 3.9 summarized force values arrive in different force range from 0 to more than 45 nN on each grafted surface. For example, on CF_3COOH grafted surface, 26.87% of all the force measurements are more than 30 nN and less or equal than 35 nN.

From the graph of both Fig.3.13 and Table 3.9**,** it is observed that the force between the silicon nitride tip and the CF_3COOH grafted surface mainly ranges from 25 to 45 nN (98.51% of all the measurements), with standard deviation of 5.3 nN. On the other hand,

more than three-quartile of the measured forces on $CF_3(CF_2)_3COOH$ and C_6F_5COOH grafted alumina surfaces lie mainly around 5~25nN (77.01% of all the measurements and standard deviation of 9.7) and 0~ 25nN (84.21% of all the measurements and standard deviation of 10.5), respectively. The mean (and median) values of the measured forces for CF_3COOH, $CF_3(CF_2)_3COOH$ and C_6F_5COOH grafted surfaces are 35.9 (36.6), 17.8 (16.8) and 12.2 (9.6). The difference between the means and medians indicates the distribution is slightly skewed towards lower forces for CF_3COOH, higher forces for $CF_3(CF_2)_3COOH$ and higher forces for C_6F_5COOH. In comparison, all measured forces between the probe and bare alumina lie in the range of 0~10nN, clearly showing an increase of interactive forces between silicon nitride probe and alumina surface after grafting.

Figure 3.14 15 AFM Force-Distance Plot measure position.

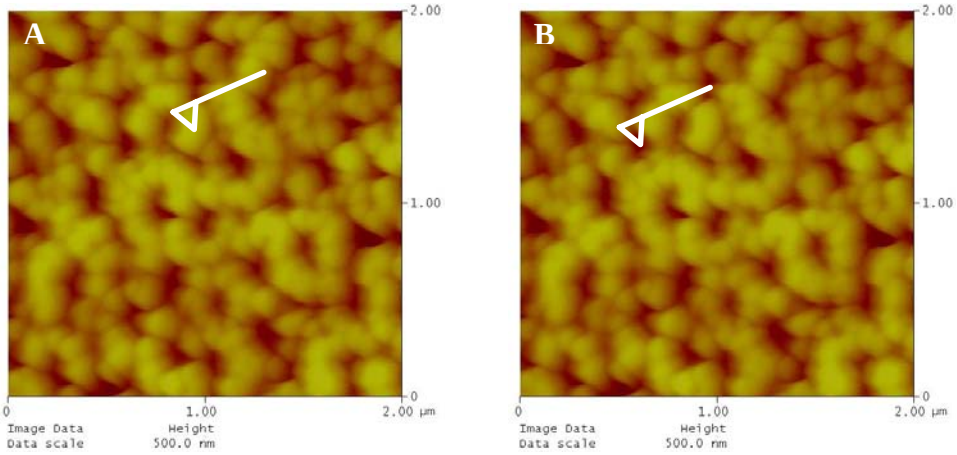

The increase of the interactive force between probe tip and grafted alumina surfaces illustrates the more hydrophobic surface property of fluorinated carboxylic acid grafted alumina surface. When the probe retracts from the surface, the grafted alumina surface interacts favorably with the hydrophobic silicon nitride probe, thus gives an increased

measured force than the less hydrophobic bare alumina surface. This increase of the hydrophobicity of fluorinated carboxylic acid grafted surface is due to hydrophobic component of fluorinated groups [32] on the surface after grafting. These AFM force-distance plot results further confirm the successful grafting on alumina surface.

The AFM probe tip may contact the alumina surface at various positions along the alumina grain. One position is at the central part of an alumina grain (Fig 3.15A); the other possible position is at the pores which appear as "dark spots" in the AFM image as shown in Fig 3.15 B. These two positions represent the extremes which would yield very different values of the contact force. All other positions would yield values of contact force in between these two extremes.

It is found that larger force values are obtained when the AFM probe measures at the "dark spots". For example, on the alumina surface grafted by $CF_3(CF_2)_3COOH$, all the force values more than 25 nN are acquired when silicon nitride probe retract from the pores of the surface. Whereas, 10~20nN large forces are obtained when AFM probe measures on exposed alumina grains. Similarly, on C_6F_5COOH grafted surface, all the forces larger than 15nN come from the "dark spots" measurements. The same trend can also be found on CF_3COOH grafted surface, forces those larger than 40nN are attributed by AFM probe retracts from alumina pores. It is also found that, when AFM tip retracts from exposed alumina grain of bare alumina surface, it gives zero force of interaction. Whereas when the tip measures in the pores of the surface, it gives 7~10 nN forces.

It is possible that when the AFM probe tip contacts the exposed alumina grain, only the tip end touches the surface followed by retracting. The retracting force is thus obtained due to interaction between the tip end and the surface. If the fluorine groups appear on the surface, a hydrophobic interaction occurs between the end of the tip and the surface. However, if the surface is not hydrophobic, there is little interaction between the tip and the surface, which is conformed using the bare alumina surface in which the AFM Force-Distance Plot gives 0 nN (not shown) when probing the exposed alumina grains.

In contrast, when the AFM probe tip retracts from the pores of alumina surface, both the side and end of probe tip are able to contact the alumina surface. Thus besides, the interaction between the end of the tip and the alumina surface, two other sources of the force attributes to the final measurement. One is hydrophobic interaction between side of the tip and the surface, which has more contact area between each other thus, gives increased force value; the other is the frictional force between the side of the tip and the surface. The magnitude of this frictional force is estimated to be about 7~10 nN, from measured forces when the probe tip retracts from the pores of a bare alumina surface.

This AFM Force-Distance Plot study carried out on nano-scale single alumina grain surface, which excluded the surface roughness effects on hydrophobicity measurement. The increasing attractive force between AFM probe and alumina surface after the surface grafted with fluorinated group indicates more hydrophobic surface is presented. The study gives out good suggest on further researches in which atomic level interaction is considered such as protein adsorption on surface with different properties.

In conclusion, surface component measurement by XPS, surface properties by both contact angle and AFM force-distance studies indicated chemical modification has been successfully performed on both commercial and etched glass supported alumina.

Chapter 4

Applications using chemically grafted nano-porous alumina

4.1 Introduction

Present applications in which surface binding of biological molecules are important includes chromatography[33], biocompatible materials for implantation[34], biosensors [35, 36] and heterogeneous catalysis[37] . Especially, the immobilization of bio-molecules onto solid surface with well controlled orientation and array, while maintaining their biological functionality is of a great interest in science today [38-40]. However, it is more difficult to achieve the same level of precise control for these biological molecules compared to the simpler molecules which are smaller and/or possess regularly repeated sub-units such as the organic molecules, polymers and nano-particles. In contrast, bio-molecules such as proteins are essentially high-molecular-weight polyamides which adopt an exquisite complexity characterized as primary, secondary, tertiary, and quaternary structures. In their physical forms, a number of different conformations can occur in the solution and solid states, as well as at the solid-liquid interface. Generally, adsorption at the solid-liquid interface occurs when the adsorption substance migrates from the adjacent phase to the surface, followed by its accumulation in the interface between bulk and surface, with resultant decrease in entropy that is larger for a flexible bio-molecules compared to a small or rigid molecule.[41]. Fundamentally, bio-molecular immobilization on solid substrates involves forces of interaction between the bio-molecules and solid surface, which vary from weak van der Waals type of force including electrostatic forces, hydrophobic interaction, and steric forces, to strong covalent bonds mainly in chemisorptions. Here, we do not include the covalent binding between protein and solid surface.

The immobilization of bio-molecules onto solid surface with well controlled orientation and array, while maintaining their biological functionality is of a great interest in science today [38-40]. It is potentially useful to applications in separations science, biosensors and biomaterials.

Self-assembly of immunoglobulin molecules have been extensively studied on modified hydrophobic gold surfaces [42-44], and glass surfaces [45] . However, little work has been carried out for aluminum oxide surfaces [46, 47] . Multiple intermolecular binding sites along the surface of a biological molecule however, makes it very difficult if not impossible, to predict accurately orientations of a protein molecule whilst physically bound onto a substrate surface. In our laboratory, we have selected immunoglobulin molecules as the surface modifying agents and the substrates employed are aluminum metal and nano-porous alumina membranes.

Since the first description of globulin proteins by Bence Jones in 1847 as a proteinaceous substance in urine specimen, the general structure of immunoglobulin has been very well elucidated. It comprises two distinct polypeptides combined to give two identical flexible arms (also known as Fab arms) and a short constant stem region (known as Fc domain) with a total molecular mass of about 150 kDalton [48] . Binding of antigens occur at the flexible arms which impart its Y-shaped structure first elucidated in 1967 by Valentine and Green using scanning electron microscopy and bifunctional antigens [48]. In recent ten years, there has been much progress in the study of self-assembly of immunoglobulin on solid substrate surfaces. Self-assembly of immunoglobulin G (IgG) on highly oriented pyrolytic graphite has been studied using atomic force microscopy (AFM). Self-assembly

occurs via initial random adsorption at nucleation sites forming monolayer patches, followed by subsequent deposition of more IgG molecules at these patches and reorganization, resulting in a homogeneous monolayer over long times [49]. This appears to be due to strong IgG-surface interactions as compared to lateral IgG-IgG interactions [49]. Structural analysis of IgG adsorbed on vacuum-evaporated gold surfaces using STM was also carried out, which revealed a molecular structure with dimensions slightly larger than those derived from crystallographic data [50]. The effects of different concentration, substrate immersion time and ionic strength on self-assembly of IgG have been studied on silica surface [51].

Here, the adsorption of immunoglobulin adsorbed on chemically grafted commercial alumina surface is studied using Atomic Force Microscopy and Quartz Crystal Microbalance (QCM).

4.2 Atomic Force Microscope study on Immunoglobulin adsorption behavior

4.2.1 AFM studies on Immunoglobulin adsorbed alumina surface

A study on the effect of chemical modification of alumina on adsorption of immunoglobulin has been carried out under Atomic force microscopy (AFM). Fig. 4-1 shows the AFM images of 1.5 μg ml^{-1} IgGs adsorbed on bare and chemically treated commercial alumina substrate surfaces.

Figure 4-1. AFM images of commercial alumina substrates with 200 nm wide pore channels obtained at increasing magnifications from I (5 µm), II (2 µm) to III (1 µm) (A)Bare commercial alumina membrane surface; (B)with no surface chemical treatment and after immersion in 1.5 µg ml^{-1} IgG solution for 30 min; (C) with surface chemically treated with trifluoroacetic acid and after immersion in 1.5 µg ml^{-1} IgG solution for 20 min.

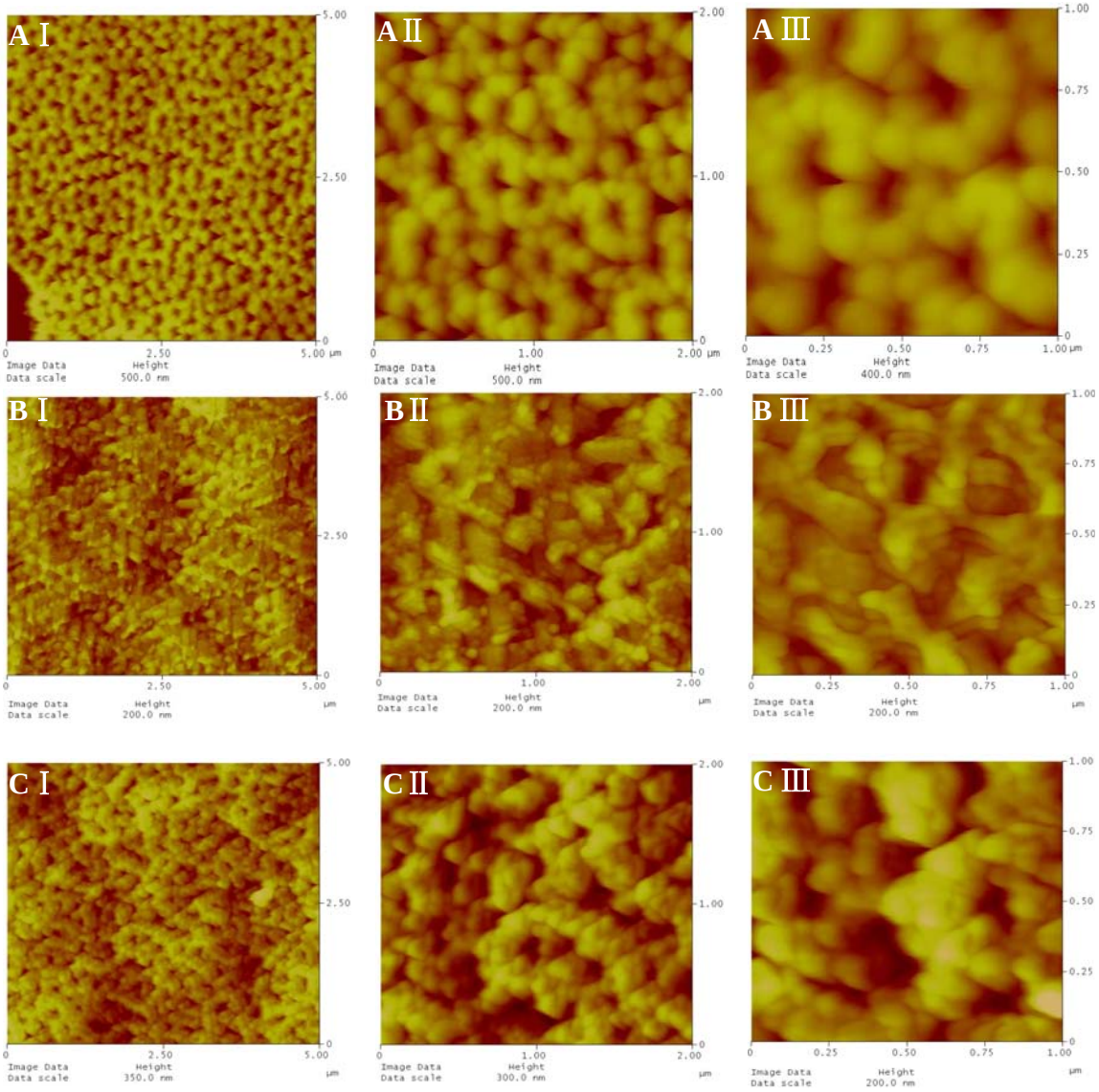

In Fig. 4-1A, bare commercial alumina substrates from Whatman® membrane with 200nm pores was studied as a control. Alumina grains with diameter about 100 nm are arranged regularly around the pores of sizes about 200nm. Fig. 4-1B shows the surface of un-treated commercial alumina substrates after immersion in IgG solutions. Unlike

the bare commercial alumina substrates (Fig.4-1A), adsorption of IgG on the alumina surface yields a structure resembling that of a honey-comb (Fig. 4-1B). Under higher magnifications (Fig.4-1B II), the surface structure was observed to comprise multi-layered ring stacks centering around the alumina pores. Each ring consists of round bead structures of about 30 ~ 50 nm in diameters. The dimension of these globular bead structures are clearly different from the size of an IgG molecule determined from X-ray crystallography studies (14 × 10 × 5nm). This is likely due to swelling of IgG molecules or aggregation of more than one IgG molecule. Only about 40% of the ring structures appear complete and remain intact during the AFM measurements. This may arise from the disruptive tapping force exerted upon the structure during the imaging process or due to drying out effect which reduces protein swelling and increases the distance between the IgG units in the ring structure, causing rupture of the weak intermolecular bonds. The relatively similar pore dimensions (200nm) and multi-layered honey-comb structure, strongly suggest protein-protein interaction plays a more important role on un-treated alumina substrate compared to protein-substrate interaction.

In contrast, the trifluoroacetic acid treated commercial alumina surfaces (Fig 4-1 C) after immersion in IgG solutions show long range nano-porous pattern very similar to the underlying alumina surface (Fig 4-1 A) but with much reduced pore sizes of about 120 to 160 nm. Another obvious difference between the trifluoroacetic acid treated and un-treated alumina surface, is the presence of regularly arranged beads with size of about 40~70nm in diameter, without the ring structure as observed in Fig 4-1B.

It is clear the difference between these two surfaces on which IgG adsorbed is due to the surface property difference brought about by CF_3 groups on the modified surface. CF_3 groups are known to confer more hydrophobic property on surfaces [32]. This is confirmed by the increased contact angle measured for $CF_3(CF_2)_3COOH$ modified glass-supported alumina surfaces compared to the chemically un-treated samples (described in Section 3.5). It has been shown that the Fc part of IgG molecule has a high preference for hydrophobic surfaces and on these surfaces, IgG molecules self-assemble to form regularly arranged end-on structures under optimum conditions. The reduction in alumina pore sizes from ~200nm of the underlying alumina substrate to 120~160nm of the IgG adsorbed surface indicates binding of IgG molecules occurs within the alumina pores and these IgG molecules adsorb as structures with heights of about 40~80nm similar in dimension to the surface bead structures (Fig. 41C). These bead structures are much larger than single IgG molecules and are likely, the result of swelling, as data derived from size measurements of IgG molecules in the same buffer solution using Malvern zetasizer Nano ZS indicate absence of IgG aggregates of these dimensions. Presently, it is however, uncertain whether the adsorbed IgG on trifluoroacetic acid treated alumina surface are arranged end-on or side-on. Although the AFM data is not conclusive with regards to the orientation of IgG molecules on the chemically treated and un-treated alumina surfaces, it clearly illustrates that a simple change in surface functionality is sufficient to affect a large difference in surface structural arrangement of IgG molecules on the alumina surface.

4.2.2 AFM studies on Immunoglobulin adsorbed on chemically grafted alumina surface

In this section, the effect of IgG concentration on the adsorption behavior of IgG molecules on a chemically grafted alumina surface is studied. Different concentrations of IgG adsorbed on $CF_3(CF_2)_3COOH$ grafted commercial alumina with 200nm pore size have been imaged using the AFM. Images with scan area of 2×2 μm, as well as cross section studies were presented in Fig. 4.2.

Fig.4.2 A shows the AFM image of the grafted alumina surface after 30 min exposure to a 0.4 μg ml^{-1} IgG-PBS solution. The pores with size of 200nm still remain, however the regularly arranged individual alumina grain of about 100 nm in diameter cannot be identified. Instead, one can observe the grains at only certain locations, while other grains appear to merge together, giving the appearance of 'inter-connecting bridges' between grains. In addition, the 3D image (Fig.4.2 AⅠ) shows some pores are filled or partially filled, while a few remained unfilled. This filling effect can be more clearly observed from the cross-section analysis (Fig. 4.2 AⅡ).

Figure 4-2. AFM images of $CF_3(CF_2)_3COOH$ grafted commercial alumina adsorbed with IgG with different concentration: (A) 0.4 μg/ml; (B) 0.8 μg/ml; (C) 1.6 μg/ml; (D) 3.2 μg/ml for 30 mins. A~D Ⅰ are 3D image of A~D; and A~D Ⅱ are cross section study on any cross line of the corresponding surface.

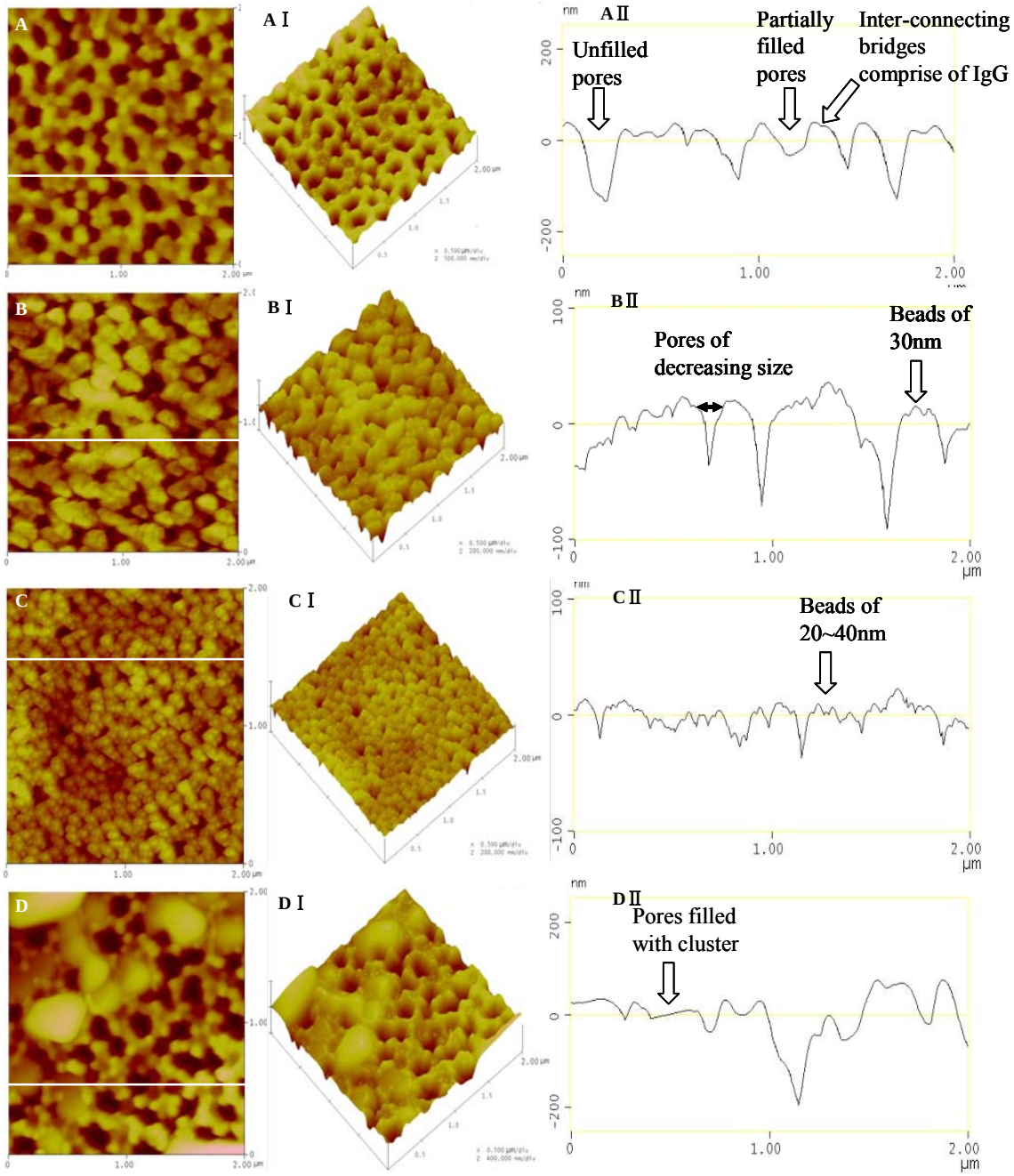

In contrast, after similar immersion time in a higher IgG concentration of 0.8 μg ml^{-1}, it is found that the pore sizes appear smaller with diameters of about 70~100 nm and most are irregularly round. 'Inter-connecting bridges' observed in Fig. 4.2 A I are not present. Instead, beads with sizes as small as 30 nm can be identified and the underlying alumina grains (about 100 nm in size) are clearly absent. 3-D image and cross-section analysis (Figs. 4.2 B I & II) clearly indicates filling of the pores occur but to a greater extent compared to the sample immersed in 0.4 μg ml^{-1}.

When the IgG concentration increases to 1.6 μg ml^{-1}, most of the surface are filled evenly with small beads about 20~40nm in dimension, and pores with size of about 30 nm is not uncommon (Fig. 4.2 C). It is clear that the pores are almost fully filled and it is difficult to identify the original position of the pores from the cross-section analysis at Fig. 4.2 C II.

This different concentration based IgG adsorption can be explained when related to nucleation rate. As it is known that, nucleation rate N can be given by the equation:

$$N = w \exp -(\Delta G_{bulk}/kT)\ C_0 \exp -(\Delta G_{het}^*/kT)$$

Whereas, C^* is the concentration of critical embryos; f is the critical embryos forming rate; C_0 is the density of nucleation atoms; w is of the order of the atomic vibration frequency; ΔG_{bulk} is the activation energy for (bulk) diffusion; ΔG_{het} is the activation energy of nucleation.

When adsorption carried out in IgG solution of low concentration, nucleation rate is low with small C_0, thus fewer nuclei are formed. Those that formed nuclei have strong preferences for crevices and pores; hence the alumina grains appear to be merged. At higher concentrations, the nucleation rates are faster with larger C_0, so the IgG molecules form nuclei on all surfaces. This effect increases with the next higher concentration of 1.6 ug ml^{-1}.

Table 4.1 Surface roughness of CF3(CF2)3COOH grafted commercial alumina adsorbed with IgG with different concentration:

	Image Z range/nm	Image RMS(rq)/nm
0.4 μg/ml	290.32	50.844
0.8 μg/ml	188.37	27.141
1.6 μg/ml	148.79	13.492

Table 4.1 shows the surface roughness of a chemically modified alumina after immersion in different concentrations of IgG solutions for 30 min. The root mean square value measures the roughness of studying surface. The Z range describes the difference between the highest point and lowest point on the measuring surface. It is clear as the IgG concentration increases, surface roughness decreases. This decreasing trend is due mainly to the filling of the pores at the higher IgG concentrations and does not describe the roughness of IgG structures adsorbed on the alumina surface. It is clear from Figs. 4B and C, that the IgG structures remain relatively unchanged at about 20~40 nm in size after immersion in 0.8 μg ml^{-1} and 1.6 μg ml^{-1} IgG solutions, while the surface roughness decreases by a factor of 2. At a much higher IgG concentration of 3.2 μg ml^{-1}, the surface structures become highly irregular, giving clusters as large as 700 nm and grains as small as 40 nm (Fig. 4D). This is likely the result of aggregates of IgG forming in solution

which precipitates onto the surface, rather than the growth of IgG structures on the chemically grafted alumina surface.

To be noted that, it is also possible to measure the IgG molecule concentration in solution after exposure to the membrane surface, hence calculate out the adsorbed IgG molecules, though there is a rinsing process after IgG adsorption, as well as the adsorption amount is too small compared to the original IgG concentration which make it difficult to measure the IgG concentration change.

In conclusion, increasing the IgG concentration assist in reducing the surface roughness of a chemically grafted alumina surface due mainly to the in-filling of the alumina pores. The surface structures of the IgG adsorbed alumina surface at the different concentration of IgG can be explained using nucleation rates.

4.3 QCM studies on Immunoglobulin adsorbed alumina surface

In this section, in a collaborative work with Ms Deng Suzi, we study the self-assembly of immunoglobulin G molecules on spontaneously formed aluminum oxide surfaces of sputtered aluminum substrates at low concentration ranges (0.4 $\mu g\ ml^{-1}$ to 6.0 $\mu g\ ml^{-1}$), analyzed using quartz crystal microbalance (QCM) technique. Figure 4-3 shows the mass densities of IgG layers assembled on the aluminum-quartz as a function of time in different solution concentrations. Mass densities of surface bound IgG layers are calculated from quartz frequency shift measurements. Maximum surface coverage of

IgG on aluminum oxide surface of aluminum quartz increases with IgG concentrations (Figure 4-3). When adsorption occurs, the IgG adsorbed onto the aluminum oxide surface resulting in a continuous mass change until it reaches the surface adsorption maximum.

Figure 4-3 Mass densities of IgG layers assembled on aluminum coated quartz crystals as a function of time in 0. 4 µg ml^{-1}, 0.8 µg ml^{-1}, 1.6 µg ml^{-1}, 2.4 µg ml^{-1}, and 3.2 µg ml^{-1}.

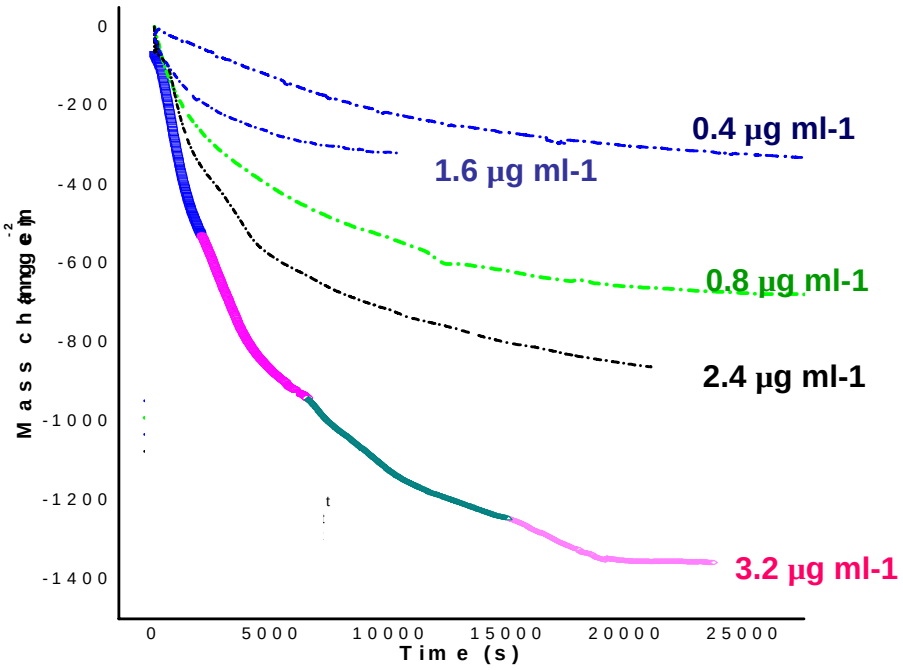

The mass densities of IgG layers assembled on the aluminum-quartz as a function of time in different solution concentrations are shown in Figure 4.3. Mass densities of surface bound IgG layers are calculated from quartz frequency shift measurements. Maximum surface coverage of IgG on aluminum oxide surface of aluminum quartz increases with IgG concentrations (Figure. 4.3). A densely-packed IgG monolayer would give a surface coverage ranging from 200 to 550 ng cm^{-2}, depending on orientation of IgG molecules[16].

Based on dimensions of an IgG molecule from X-ray crystallography studies (14 × 10 × 5nm)[17], it was estimated that a monolayer of IgG would give a surface coverage of 200 ng cm^{-2} when all IgG molecules were bound to the surface via a side-on configuration[16]. End-on orientations yield different surface coverage depending on density of the monolayer - 550 ng cm^{-2} for compact end-on configuration, 370ng cm^{-2} for end-on with intermediately-spaced Fab arms and 260ng cm^{-2} for end-on with widely repelling F_{ab} arms[16]. Based on these theoretical calculations, we expect the maximum surface coverage at 335 ng cm^{-2} for concentration 0.4 μg ml^{-1} to be equal to one monolayer which is likely between a flat monolayer (200ng cm^{-2}) and an end-on monolayer (550 ng cm^{-2}) [16].

The same trend of increasing maximum surface coverage at increasing IgG concentrations is also observed using a different 10 MHz QCM system. However, it is clear from Fig. 4.3, this trend is not always observed for all concentrations. The non-proportional increase in maximum surface coverage with respect to the 0.8 μg ml^{-1} concentration case is due to variations in surface areas of sputtered aluminum films. Quartz cells coated with sputtered aluminum within the same batch and across batches give different results in terms of maximum surface coverage values in self-assembly studies using same IgG bulk concentrations. This poor reproducibility may due to abnormal differences in distribution ratios of different aluminum grain sizes on 0.8 μg ml^{-1} sputtered aluminum quartz, though further experiments are needed to confirm that there is not any other experimental error. Under our optimized sputtering conditions, the crystal grain sizes are relatively uniform between 200 to 300 nm, with intermittent dispersion of larger grains with sizes of about 500 nm. Assuming the grains are

hemispherical shape and regularly arranged with no interstitial spaces in between, the highest possible actual surface area in contact with the solution phase would be two times the geometric area. From AFM and SEM studies (not shown), the grains are generally flat and heights of these grains on sputtered aluminum film surfaces are less than half the average grain radius. Therefore, it is reasonable to assume actual surface areas to lie somewhere between 1 and 1.5 times the geometric area. Theoretical maximum surface coverage for a monolayer coverage of IgG are between 200 and 550 ng cm^{-2}, calculated based on side-on and compacted end-on configurations respectively for self-assembly onto a planar surface [16, 18]. If surface area of sputtered aluminum film for the 0.8 μg ml^{-1} case is at 1.5 times more than the geometric quartz area, the observed maximum surface coverage at 620 ng cm^{-2} still falls within the monolayer coverage regime. At higher concentrations, it is clear the maximum mass densities of surface bound IgG layers extend beyond the theoretical mass density value for one monolayer even for an aluminum surface with maximum possible roughness of two times the geometric area. This discussion to identify the monolayer and multilayer coverage regimes is necessary for the sputtered aluminum-quartz system which lacks atomically flat surfaces. Likewise, we have chosen sputtering conditions which produce surfaces with average grain size much larger than the dimensions of IgG molecules in order to clearly distinguish the morphology of surface bound IgG layers from the underlying aluminum structures.

Interestingly in Fig. 4.3, the mass density changes for aluminum-quartz immersed in IgG solutions of high concentrations show several step plateaus, which are unusual and not observed for self-assembly of IgG on gold in similar concentration ranges using our

system. These step plateaus are also absent in reports for other QCM studies of IgG self-assembly on gold surfaces [6, 8] nor on other types of surfaces[19, 20]. In Fig. 2, we replot the same data from Fig. 4.3 as rate of mass density change with respect to surface coverage for IgG at different initial IgG bulk concentrations.

If self-assembly of IgG on aluminum oxide surface of aluminum quartz occurs through initial random adsorption and unlimited by diffusion, we can approximate the assembly process using Langmuir kinetics, under the conditions where adsorption energy is constant at all surface coverage and the total number of available binding sites remain constant. The rate of protein adsorption can be described according to equation (4-1) which is first order with respect to concentration of adsorbing species and number of available binding sites at the surface for an irreversible adsorption process.

$$\frac{d\Gamma}{dt} = k_{ads} c_b (\Gamma_{\max} - \Gamma) \qquad \text{Eq. (4-1)}$$

Where k_{ads} is the adsorption rate constant and cb is the bulk concentration, assuming ka and cb remain constant throughout the adsorption process. $\Gamma_{\max}$ is the maximum number of surface binding sites, and Γ is the surface available binding site at the time.

Figure 4.4 Replot of the data in Figure 3-1 in terms of rate of mass density change on aluminum oxide surface of aluminum-quartz as a function of surface coverage.

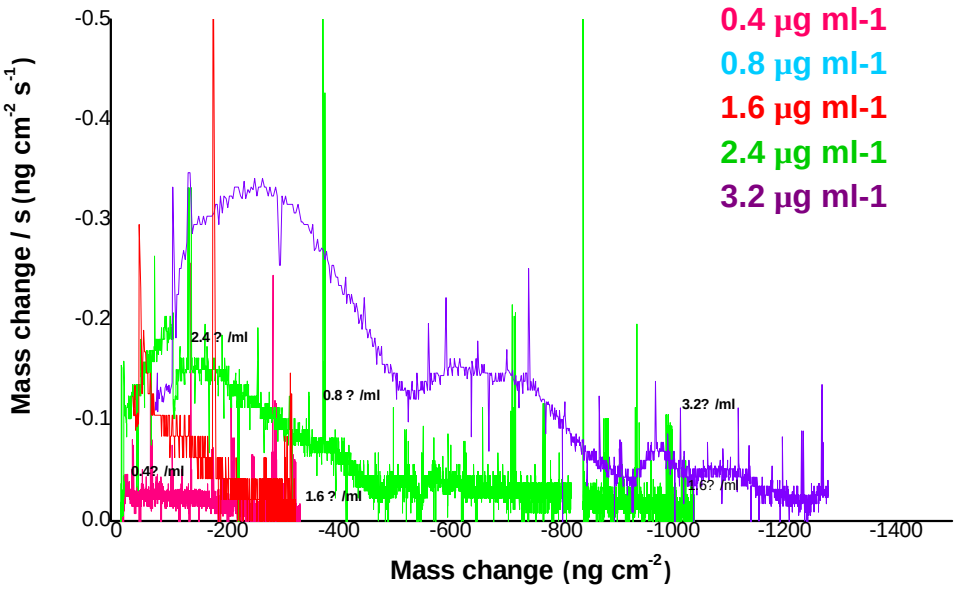

Figure 4.4 shows the rate plot of mass density change with respect to surface coverage for IgG at different concentrations. From Figure 4.4, the self-assembly of IgG on aluminum oxide surface of aluminum quartz obey Langmuir kinetics for the 0.4 µg ml^{-1} concentration, suggesting relatively unoccupied area of the surface is available for adsorption of IgG throughout the assembly process. At higher concentrations of 0.8 and 1.6 µg ml^{-1}, the rate of mass density change decreases linearly with surface coverage at low surface coverage below about 40 %. The same is observed for deposition of IgG from similar concentrations using a 10 MHz QCM system (not shown). This is consistent with Langmuir adsorption kinetics in the absence of desorption and in situations when entire unoccupied area of the surface is available for the deposition of fresh IgG. At higher surface coverage however, the rates of mass density changes

decrease more slowly and gradually become negligible. This indicates either unfavorable interactions between IgG molecules when crowding of sites occur or relaxation of the surface bound IgG molecules which reduce the amount of available sites for further deposition. This deviation from Langmuir kinetics is unlikely due to diffusion limitation of adsorbate molecules reaching the substrate surface since adsorption rate is not proportional to $t^{1/2}$, as determined from curve fitting at the high surface coverage regime.

At higher concentrations of 2.4 and 3.2 μg ml^{-1} we observe a significant difference in the rates of mass density changes for aluminum-quartz immersed in IgG solutions compared to lower concentrations between 0.4 and 1.6 μg ml^{-1}. First, initial maxima in the rate curves are absent at the lower concentrations. Second, there are a series of transient peaks in the rate curves for 2.4 and 3.2 μg ml^{-1} concentrations, corresponding to the unusual steps observed in Fig. 4.3. These peak maxima may arise due to a nucleation mechanism and the short lag period with sigmoid shape observed at end of each step plateau strongly suggest nucleation growth is involved[21]. Another possible explanation is abrupt changes in the surface bound IgG structures which occur during transient rise and fall in the rate curves. Adsorption studies of globular proteins on surfaces have reported observation of stepwise increase in surface bound protein amount with protein concentrations[22]. This has been attributed to discrete changes in IgG packing with concentrations[23]. However, these stepwise increases were reported with respect to changes in initial bulk protein concentrations, different from the stepwise increase in surface bound IgG amount with respect to time in Fig. 4.3. It is also unclear how reorganization of surface bound IgG structure driven by minimization of surface energies

and relaxation of protein structures should take place abruptly after reaching stable mass density values. A third possible reason for the unusual transient maxima in the rate curves is viscoelastic variation of the surface bound IgG layer. Viscoelastic contributions to frequency shift during QCM measurements may cause the measured values to deviate from actual mass of IgG deposited. Zhou et al.[42] showed QCM overestimates the amount of mass deposited by 20% for an apparent surface coverage of 361 ng cm^{-2} and by as much as 60% for an apparent surface coverage of 1340ng cm^{-2} as compared to the values obtained by another viscoelasticity-independent surface acoustic wave technique[6].

It is interesting to note at the end of mass measurement experiments after the mass densities have reached close to maximum surface coverage values, there are sufficiently large amounts of IgG in bulk solutions for further deposition of IgG molecules on the surface bound IgG layers. We add more IgG to these bulk solutions after the initial 10000s when mass densities of IgG layers assembled on aluminum-quartz have reached constant values. However, no appreciable mass change is observed over additional wait time of 10000 s. It is clear in the case when protein-surface interactions are much stronger compared to protein-protein interactions, no further deposition of IgG will occur once the surface is covered with a monolayer of IgG molecules. However, the QCM data indicates multilayer coverage on the aluminum oxide surface of aluminum-quartz can be obtained at higher initial IgG concentrations. Therefore, the observed negligible mass change during successive additions of IgG solutions after long immersion times is likely due to conformational changes of the surface bound IgG structures which prevent further deposition of IgG molecules from bulk solutions. Differences of about 20% in total

surface bound IgG amount were reported between successive and one-time additions of IgG solution during IgG self-assembly on hydrophobic silica surfaces [15]. Jonsson et al. attributed this phenomenon to time and surface-dependant conformational changes of the surface bound IgG which obstructed further IgG deposition at successive-additions [15]. Since no further mass change is observed during successive additions for both IgG monolayer and multilayer covered aluminum-quartz, time-dependent conformational changes are likely to play a more significant role compared to surface-dependent conformational changes here. We confirm IgG assembly on alumina is irreversible over the time period of mass measurement experiments, by monitoring the frequency of IgG-coated aluminum-quartz after replacing the bulk IgG solution with deionized water. Negligible frequency changes are observed for both the monolayer and multi-layer cases. This negligible desorption of surface bound IgG further supports the above observations of essentially unchanged mass densities of surface bound IgG layers, under conditions of successive additions of IgG solutions. Initial IgG concentration in bulk solution is thus important in determining maximum mass densities of IgG assembled on aluminum oxide surface of aluminum-quartz and this is likely due to a process of protein conformational rearrangement which disfavors further depositions even in the presence of excess IgG in bulk solutions.

The above study on adsorption of IgG molecules on aluminum metal covered with spontaneously formed aluminum oxide provides an insight into how IgG molecules adsorb on the surface of aluminum oxide. It is clear from this study that multilayer growth of IgG occurs only when IgG concentrations are larger than a critical value. In

this case of aluminum oxide formed spontaneously on aluminum metal, the value is close to or higher than 2.4 μg ml^{-1}. Second, maximum surface coverage of IgG on aluminum oxide surface does not depend on total amount of IgG molecules in solution, but vary with concentration of IgG. These findings are very useful towards our further work in the development of an electrochemical immunosensor based on immunoglobulin-gated nano-channels of nano-porous alumina.

In conclusion, the Quartz crystal microbalance studies of self-assembly of IgG on sputtered aluminum films covered with spontaneously formed aluminum oxide indicate multilayer growth in IgG concentrations at and higher than 2.4 μg ml-1. Results from both QCM and AFM data suggests a self-assembly mechanism which progresses via initial nucleation growth of immunoglobulin molecules, followed by abrupt rearrangement of surface structures due to structural instability of the vertically growing ellipsoidal structures. Further deposition of IgG molecules do not occur on IgG surface structures which have undergone conformational changes at long time.

Chapter 5

Conclusion and prospective work

5.1 Conclusion

Because of its well defined pores sizes, nano-porous anodic alumina manufactured in electrochemical method has its potential applications in a variety of fields such as template for fabricating other nano-porous structures; dielectrics in capacities; mechatronic system, and so on. In this work, a novel way of chemically grafted nano-porous alumina to produce different surface properties has been described. Three kinds of fluorinated carboxylic acids, Trifluoroacetic acid, pentafluorobenzoic acid, and perfluoropentanoic acid, have been attempted to graft on anodic alumina membrane and home-made glass-supported alumina surface. The latter is manufactured using electrochemical anodization on sputtered aluminum, and different pore sizes can be obtain by different wet etching period. X-ray Photoelectron Spectroscopy AXIS Instrument has been used to study the surface modification. Fluorinated elements are found on these grafted surfaces. On $CF_3(CF_2)_3COOH$ and C_6F_5COOH grafted surface, ratio of F to Al is proportional to the F atom number in the chemicals respectively. Moreover, it is also found that the oxalic acid residue remaining on the glass-supported alumina surface during the anodization step reduce the possibility of further fluorinated carboxylic acid grafting. The shift on Al 2p peak after surface grafted also indicated secondary shift on grafted alumina membrane and etched glass-supported alumina film suggesting successful grafting on both commercial alumina membrane and etched glass-supported alumina surface by three different fluorinated carboxylic acids.

The grafted surfaces have also been characterized by Contact Angle and AFM Force-Distance Plot. The contact angle results gave out the surface property difference with effects of surface pore sizes and chemical composition. It is found that the surface hydrophobicity is increased as the alumina pore size increases. The further surface property variation based on different surface component has been investigated by AFM Force- Distance plot at molecular level. The surface property and measuring position effects on AFM Force- Distance plot has been discussed.

Application of nano-porous alumina has been explored by Atomic Force Microscopy and Quartz Crystal Microbalance. Different performance of Immunoglobulin adsorption on un-grafted anodic alumina membrane and fluorinated group grafted alumina surface has been discovered under tapping mode AFM. It can be concluded that on a hydrophobic alumina surface which is grafted with fluorinated group, IgG molecules will adsorb with more regular orientation. AFM image studies also have been carried out on chemically grafted alumina surface adsorbed with different concentrated IgG solution. It clearly shows more surface coverage of IgG molecules is obtained as the adsorbent concentration increased until excess IgG molecules aggregate as cluster before arriving on the surface. Different concentration effects on IgG adsorption behavior have also been studied on thermal alumina under Quartz Crystal Microbalance. Maximums of adsorption rate are observed when the adsorption concentration exceeds monolayer and due to nucleation formation.

5.2 Prospective work

The hydrophilic alumina surface can be modified into different properties by the method describe in this work. In similar point of view, other functional groups such as carboxylic group, amino group, and so on can be grafted on both commercial and etched glass-supported alumina surface with freely controlled pore sizes. These diverse functional groups can not only change alumina surface property, but also can further react with another molecules, for instance, bio-molecules, thus produce covalent binding on nano-porous surface with broad promising applications.

During the attempt to observe IgG adsorption on treated alumina using QCM, we have encountered a difficulty to mount treated alumina on QCM quartz. Future work involves the feasible way to attach either commercial alumina or home-made alumina sheet to the quartz surface thus compare the IgG adsorption on un-treated alumina surface witH-treated ones.

It can be observed that all AFM images are taken from commercial alumina as it provides a smoother surface than home-made anodized alumina films. Future work can be carried out on mechanical polishing glass-supported alumina films with which is not only possible to obtain a smooth surface both also can effectively remove the surface with chemical residue thus helpful in further modification.

Atomic Force Microscopy Force-Distance curve performs a promising technique in bio-molecules studies which can provide additional information from the atomic level. After being functionalized, AFM probe performs different attraction in forms of force with different surface. For instance, the probe modified with a certain kind of antigen A will give most obvious force when tip retrieved from the surface which is grafted with anti-A. However, there are various factors complicate the presented force, for example, the deformation of surface molecular or the electrostatic force between probe and surface, therefore, the operation environment of liquid buffer is of better choice than atmosphere.

Based on our discussion on IgG adsorption of nucleation effect, future work can include time-frame adsorption AFM studies, thus can further understand IgG adsorption behavior, especially on those surfaces with different properties which probably affect the adsorption.

Furthermore, dual polarization interferometry (DPI), a newly developed analytical tool is another good option to further studies IgG adsorption. Using two orthogonal polarizations, a high resolution of 1Å of thickness and refractive index can be obtained. Based on these information, especially real time detection can be given by DPI, we can further understand IgG adsorption behavior, as well as their conformational changes when challenged with its antigen.

Reference:

1. K.Siegbahn, C.N.Nordling, A.Fahlman, R.Nordberg, K.Hamrin, J.Hedman, G.Johansson, T.Bergmark, S.E.Karlsson, I.Lindgern, and B.Lindberg, *ESCA: Atomic, Molecular and Solid State Structure Studies by Means of Electron Spectroscopy*, Almqvist and Wiksells, Uppsala, **1967**
2. Siegbahn, K. et al., *ESCA – Atomic, Molecular and Solid State Structure Studied by Means of Electron Spectroscopy*, Alqvist and Wiksells, Uppsala **1967**
3. Lindberg, B. J., Hamrin, K., Johansson, G., Gelius, U., Fahlman, A., Nordling, C. and Siegbahn, K., *Molecular Spectroscopy by Means of ESCA Π Sulphur Compounds. Correlation of Electron Binding Energy with Structure.* Uppsala University Institute of Physics UUIP-63B, **1970**
4. Woodruff and Delchar, *Modern Techniques of Surface Science*, Cambridge University Press, **1986**
5. Handbook of X-ray Photoelectron Spectroscopy, (C.D.Wagner, W.M.Riggs, L.E.Davis, J.F.Moulder and G.E.Mullenberg, eds.), Perkin-Elmer Corporation **1979**.

6. Briggs, D., and Seah, M.P., eds., *Practical Surface Analysis by Auger and X-Ray Photoelectron Spectroscopy*, John Wiley and Sons, **1983**
7. Woodruff and Delchar, *Modern Techniques of Surface Science*, Cambridge University Press, **1986**
8. Briggs, D., and Seah, M.P., eds., *Practical Surface Analysis by Auger and X-Ray Photoelectron Spectroscopy*, John Wiley and Sons, **1983**
9. Powell, C.J., and Seah, M.P., *J.Vac.Sci.Technol.A,* **1990**, vol.8, no.2, Mar/Apr
10. Woodruff and Delchar, *Modern Techniques of Surface Science*, Cambridge University Press, **1986**
11. G.Binnig, C.F.Quate, and C.Gerber, *Phys.Rev.Lett.,* **1986**, 12,930,
12. G.Meyer and N. M. Amer, *Appl. Phys. Lett*., **1988,** 53, 2400,
13. Mecea, V.M. *Sens.Actuators A* **1994**, 40, 1-27.
14. O'Sullivan, C.K.; Guilbault, G.G. *Biosensors Bioelecton*. **1999**, 14,663-670
15. JJ Donohue, DA Buttry. *Langmuir* **1989**, 5:671,
16. K Ijiro, M Shimomura, M Tana ka, H Nakamura, K Hasebe. *Thin Solid Films* **1996**, 284-285:780,
17. G Sauerbrey. Z *Phys* **1959,** 155:206.
18. KK Kanazawa, JG Gordon. *Anal Chim Acta* **1985,** 175:99,
19. Bernard P.Binks, Modern Characterization Methods of Surfactant Systems,
20. Arthur T. Hubbard, The Handbook of Surface Imaging and Visualization,
21. Ketul C. Popat, Copal Mor, Craig A. Grimes, et al. *Langmuir* **2004**,20,8035-8041
22. Belyavskii S.G.; Mingalev P.G.; Lisichkin G.V. *Colloid Journal.* **2004**, Vol.66, No.2,.pp.156-165

23. Karaman, M.E., Antelmi D.A. and Pashley R.M., *Colloids and Surfaces A*, **2001,** 182, 285-298.

24. Sah A, Castricum HL, Bliek A, et al. *Journal of Membrane Science* **2004**, 243 (1-2): 125-132

25. Karaman, M.E., Antelmi D.A. and Pashley R.M., *Colloids and Surfaces A,* **2001,** 182 , 285-298,.

26. C. S. Toh, B. M. Kayes, E. J. Nemanick and N. S. Lewis, *Nanoletters*, **2004**, 4 (5), 767-770.

27. Zhang, JX; Zhang, LD; Ye, CH; et al., *Chemical Physics Letters*, **2004**, 400 (1-3): 158-162

28. Charles R. Martin *Science*, New Series, **1994,** Vol. 266, No. 5193., pp. 1961-1966

29. Zong RL, Zhou J, Li Q, et al. 398 (1-3): 224-227 NOV 1

30. Moueddeb H, Sanchez J, Bardot C, et al. *Journal of Membrane Science* **1996**, 114 (1): 59-71 MAY 29

31. Handbook of X-ray photoelectron spectroscopy: a reference book of standard spectra for identification and interpretation of XPS data / by John F. Moulder, et al. edited by Jill Chastain. Eden Prairie, Minn. Perkin-Elmer Corporation, Physical Electronics Division, c**1992**.

32. Key BD, Howell RD, Criddle CS; Fluorinated organics in the biosphere; Environmental Science & Technology **1997**, 31 (9), 2445-2454.

33. Fu, H. J.; Huang, X. D.; Jin, W. H. and Zou, H. F., *Curr. Opin. Biotechnol.* **2003,** 14, 96-100.

34. Chu, P. K.; Chen, J. Y.; Wang, L. P. and Huang, N., *Materials Science & Engineering R-Reports* **2002,** 36, 143-206.

35. Kohli, P.; Wirtz, M. and Martin, C. R., *Electroanalysis* **2004,** 16, 9-18.

36. Lucarelli, F.; Marrazza, G.; Turner, A. P. F. and Mascini, M., *Biosensors & Bioelectronics* **2004,** 19, 515-530.

37. Bourdillon, C.; Demaille, C.; Moiroux, J. and Saveant, J. M., *J. Phys. Chem. B* **1999,** 103, 8532-8537.

38. Bergkvist, M., Carlsson, J and Oscarsson, S., "A method for studying protein orientation with atomic force microscopy using relative protein volumes" *J. Phys. Chem. B* **2001,** 105, 2062-2069.

39. Topoglidis, E.; Cass, A.E.G.; O'Regan, B. and Durrant, J. R., "Immobilisation and bioelectrochemistry of proteins on nano-porous TiO2 and ZnO films", *Journal of Electroanalytical Chemistry* **2001,** 517, 20-27,.

40. Chen S.F., Liu L.Y., Zhou J. and Jiang S.Y., *Langmuir* **2003,** 19, 2859-2864,.

41. FL Slejko. Adsorption Technology: A Step-by-Step Approach to Process Evaluation and Application. New York: Marcel Dekker, **1985**, pp1-6

42. Zhou, C.; Friedt, J. M.; Angelova, A.; Choi, K. H.; Laureyn, W.; Frederix, F.; Francis, L. A.; Campitelli, A.; Engelborghs, Y. and Borghs, G., *Langmuir* **2004,** 20, 5870-5878.

43. Karyakin, A. A.; Presnova, G. V.; Rubtsova, M. Y. and Egorov, A. M., *Anal. chem.* **2000,** 72, 3805-3811.

44. Caruso, F.; Rodda, E. and Furlong, D. N., *J. Colloid Interface Sci.* **1996,** 178, 104-115.

45. Yoshioka, M.; Mukai, Y.; Matsui, T.; Udagawa, A. and Funakubo, H., *Journal of Chromatography-Biomedical Applications* **1991,** 566, 361-368.

46. Djokic, S. S. and Burrell, R. E., *Biosensors & Bioelectronics* **1998,** 13, 271-278.

47. Jia, R. P.; Shen, Y.; Luo, H. Q.; Chen, X. G.; Hu, Z. D. and Xue, D. S., *Thin Solid Films* **2005,** 471, 264-269.

48. Valentine, R. C., Green, N.M., *J. Mol. Biol.* **1967,** 27, 615-617.

49. Cullen, D. C. and Lowe, C. R., *J. Colloid Interface Sci.* **1994,** 166, 102-108.

50. You, H. X.; Disley, D. M.; Cullen, D. C. and Lowe, C. R., *Int. J. Biolo. Macromole.* **1994,** 16, 87-91.

51. Jonsson, U.; Lundstrom, I. and Ronnberg, I., *J. Colloid Interface Sci.* **1987,** 117, 127-138.